Lancelot, Y., Larson, R. L., et al., 1990
Proceedings of the Ocean Drilling Program, Initial Reports, Vol. 129

2. SITE 800[1]

Shipboard Scientific Party[2]

HOLE 800A

Date occupied: 25 November 1989

Date departed: 5 December 1989

Time on hole: 9 days, 19 hr, 45 min

Position: 21°55.38′N, 152°19.37′E

Bottom felt (rig floor; m, drill-pipe measurement): 5697.0

Distance between rig floor and sea level (m): 11.00

Water depth (drill-pipe measurement from sea level, m): 5686.0

Total depth (rig floor; m): 6241.40

Penetration (m): 544.40

Number of cores (including cores with no recovery): 61

Total length of cored section (m): 544.40

Total core recovered (m): 150.73

Core recovery (%): 27

Oldest sediment cored:
Depth (mbsf): 498.10
Nature: chert
Earliest age: Berriasian
Latest age: Valanginian

Basement:
Depth (mbsf): 498.10
Nature: Basalt

Principal results: Site 800 is located in the northern Pigafetta Basin on magnetic anomaly lineation M33, 40 miles northeast of Himu Seamount. Its presumed basement age is Jurassic, based on an extrapolation of the Japanese magnetic lineation pattern that is contained in the same spreading compartment to the northwest. Hole 800A consists of the following stratigraphic sequence:

0–38 mbsf: Tertiary to Upper Campanian zeolitic brown clay.

38–78 mbsf: Upper Campanian to Turonian red cherts and porcellanites corresponding to the top of the reverberant layer on seismic records.

78–229 mbsf: Cenomanian to Lower Albian grey chert and silicified limestone with increasing amounts of silicified limestone downsection, grading into nannofossil chalk at the base of the sequence.

229–450 mbsf: Aptian volcaniclastics, well indurated and possibly emanating from Himu Seamount 40 miles to the southwest that is radiometrically dated at 120 m.y. (Aptian-Barremian), with occasional included radiolarites. The volcaniclastics contain spectacular turbidite and debris flow features, including graded beds, cross bedding, tear-up structures, and penecontemporaneous deformation obvious even to geophysical investigators.

450–498 mbsf: Hauterivian to Berriasian laminated claystones, red with occasional black banding and green reduction halos. Hard red chert at the base of the sequence.

500–545 mbsf: Dolerite, massive, aphyric, medium-grained, holocrystalline with no observed internal cooling unit boundaries. The dolerite is marginally finer grained at the top and contains no macroscopically observable glass or palagonite. Large, elongate clinopyroxene crystals are present throughout, and the material is relatively fresh and unweathered except for the top 1 m. The top of this unit corresponds to a flat, high-amplitude seismic reflector that is essentially acoustic basement in this area.

Drilling was terminated at 545 mbsf due to a tight spot in the hole at 350 mbsf that was probably caused by swelling clays in the volcaniclastic section. A summary of coring statistics is presented in Table 1. Logging with standard tools was conducted in three runs from 45 to about 300 mbsf.

BACKGROUND AND OBJECTIVES

The correlation of the M1 to M22 Mesozoic magnetic anomaly sequence in the Pacific by Larson and Chase (1972) indicated that the oldest ocean crust beneath the Pacific Basin is centered in the far western Pacific Ocean. Hilde (1973) and Hilde et al. (1976, 1977) extended these correlations to M26, and predicted that the point of origin of the Pacific plate lies within the triangle found at the Leg 129 drill sites (800, 801, and 802), and is of Middle to Early Jurassic age. Cande et al. (1978) extended these Pacific magnetic lineation correlations to M29, and Handschumacher and Kroenke (1978) recognized some version of the same lineations. These correlations were further extended to M38 by Handschumacher and Gettrust (1985).

Site 800 (proposed site PIG-1) was drilled in the northwestern region of the Pigafetta Basin (Fig. 1), in an area where magnetic anomalies believed to correspond with the M-series were mapped recently by Handschumacher and Gettrust (1985), Tamaki et al. (1987), Handschumacher et al. (1988), and Nakanishi et al. (1989). These anomalies are well defined in this area and extend from M25 to the northwest through M37 to the southeast. Because we follow Tamaki et al.'s (1987) suggestion that Handschumacher et al. (1988) miscorrelated M29 from its original definition in Cande et al. (1978), our M-series numbers are always one less than in Handschumacher et al. (1988) for anomalies older than M29.

Site 800 lies on anomaly M33 (Figs. 2 and 3), in an area where multichannel seismic profiles (including refraction data) obtained aboard the *Le Suroit* during the MESOPAC II cruise in August 1989 (see "Site Geophysics and Seismic Stratigraphy" section, this chapter) indicated that the basement might be reached relatively easily, as there is no evidence of substantial accumulation of Cretaceous volcanogenic sediments or hard rocks within the sediment section. The total sediment thickness was estimated to be about 550 m based on seismic velocities obtained from a refraction sonobuoy launched nearby during MESOPAC II.

The final choice for the location of this site was also determined by the thickness of soft sediment lying above the top of the "opaque layer" (Houtz and Ludwig, 1979) which was correlated regionally with Upper Cretaceous cherts that result from diagenetic alteration of siliceous organisms accumulated during the transit of this area beneath the equatorial zone of high productivity. A minimum of about 35 m of soft sediment above the hard chert is generally considered necessary to provide support for the bottom-hole assembly before any substantial weight can be applied to the drill bit. At Site

[1] Lancelot, Y., Larson, R. L., et al., 1990. *Proc. ODP, Init. Repts.,* 129: College Station, TX (Ocean Drilling Program).

[2] Shipboard Scientific Party is as given in the list of participants preceding the contents.

Table 1. Coring summary for Site 800.

Core	Date (1989)	Time (UTC)	Depth (mbsf)	Length cored (m)	Length recovered (m)	Recovery (%)
129-800A-						
1R	26 November	1545	0.0–1.0	1.0	0.32	32.0
2R	26 November	1950	1.0–10.6	9.6	0.01	0.1
3R	26 November	2055	10.6–20.2	9.6	2.03	21.1
4R	26 November	2200	20.2–29.9	9.7	5.07	52.2
5R	26 November	2305	29.9–39.6	9.7	0.39	4.0
6R	27 November	0030	39.6–49.2	9.6	0.51	5.3
7R	27 November	0210	49.2–58.9	9.7	0.53	5.5
8R	27 November	0350	58.9–68.5	9.6	0.70	7.3
9R	27 November	0525	68.5–78.2	9.7	0.34	3.5
10R	27 November	0715	78.2–87.8	9.6	0.57	5.9
11R	27 November	0845	87.8–97.3	9.5	0.71	7.5
12R	27 November	1035	97.3–106.8	9.5	0.32	3.4
13R	27 November	1230	106.8–116.2	9.4	0.57	6.1
14R	27 November	1430	116.2–125.4	9.2	1.03	11.2
15R	27 November	1610	125.4–134.9	9.5	0.16	1.7
16R	27 November	1805	134.9–144.2	9.3	0.24	2.6
17R	27 November	2025	144.2–153.7	9.5	0.65	6.8
18R	27 November	2245	153.7–162.9	9.2	1.31	14.2
19R	28 November	0050	162.9–172.4	9.5	0.77	8.1
20R	28 November	0320	172.4–181.3	8.9	0.40	4.5
21R	28 November	0720	181.3–191.0	9.7	1.59	16.4
22R	28 November	1005	191.0–200.5	9.5	0.67	7.1
23R	28 November	1255	200.5–209.9	9.4	0.92	9.8
24R	28 November	1620	209.9–219.3	9.4	1.00	10.6
25R	28 November	1830	219.3–228.6	9.3	0.41	4.4
26R	28 November	2040	228.6–238.0	9.4	4.41	46.9
27R	28 November	2250	238.0–247.2	9.2	2.19	23.8
28R	29 November	0050	247.2–256.5	9.3	7.23	77.7
29R	29 November	0310	256.5–265.9	9.4	4.41	46.9
30R	29 November	0525	265.9–272.0	6.1	3.18	52.1
31R	29 November	0735	272.0–278.1	6.1	3.54	58.0
32R	29 November	1140	278.1–287.5	9.4	2.84	30.2
33R	29 November	1450	287.5–297.0	9.5	9.12	96.0
34R	29 November	1655	297.0–306.4	9.4	6.92	73.6
35R	29 November	1850	306.4–315.9	9.5	4.37	46.0
36R	29 November	2100	315.9–325.1	9.2	7.81	84.9
37R	29 November	2250	325.1–334.5	9.4	3.10	33.0
38R	30 November	0040	334.5–343.8	9.3	1.90	20.4
39R	30 November	0250	343.8–353.1	9.3	5.58	60.0
40R	30 November	0500	353.1–362.5	9.4	1.52	16.2
41R	30 November	0650	362.5–368.6	6.1	2.02	33.1
42R	30 November	0840	368.6–374.7	6.1	1.69	27.7
43R	30 November	1315	374.7–383.7	9.0	1.28	14.2
44R	30 November	1515	383.7–393.1	9.4	2.52	26.8
45R	30 November	1725	393.1–402.5	9.4	5.27	56.0
46R	30 November	2125	402.5–411.9	9.4	5.34	56.8
47R	30 November	2345	411.9–421.4	9.5	5.22	54.9
48R	30 November	0215	421.4–430.9	9.5	8.22	86.5
49R	01 November	0450	430.9–440.2	9.3	5.42	58.3
50R	01 November	0740	440.2–449.6	9.4	3.55	37.7
51R	01 November	0950	449.6–458.8	9.2	1.68	18.2
52R	01 November	1200	458.8–464.9	6.1	3.53	57.8
53R	01 November	1420	464.9–471.0	6.1	2.27	37.2
54R	01 December	1915	471.0–479.1	8.1	2.88	35.5
55R	01 December	2200	479.1–488.5	9.4	3.00	31.9
56R	01 December	0105	488.5–498.0	9.5	0.36	3.8
57R	01 December	0555	498.0–507.2	9.2	1.94	21.1
58R	02 December	1030	507.2–516.6	9.4	3.55	37.7
59R	02 December	1425	516.6–525.9	9.3	0.22	2.4
60R	02 December	1810	525.9–535.3	9.4	1.12	11.9
61R	03 December	0020	535.3–544.4	9.1	0.31	3.4
Coring totals				544.4	150.73	27.7

800 the thickness of the soft sediment layer believed to correspond with post-Cenomanian deposits was estimated at about 51 m, based on 3.5-kHz profiles from the MESOPAC II survey as well as those obtained aboard the *JOIDES Resolution* during the approach to the site (see "Site Geophysics and Seismic Stratigraphy" section, this chapter).

The specific objectives for this site were (1) to determine if the lowermost sediment layers and basement could be reached with a single bit hole, and (2) to obtain as complete a section as possible down to the presumed Jurassic sediments and basement. We planned to drill a pilot hole at Site 800 to be followed by drilling another hole to the southeast, within the Jurassic quiet zone (JQZ), before deciding if and where a multiple reentry site with extensive casing would offer the best opportunity to sample the oldest sediment and achieve substantial penetration into the basement. Site 800, representing the youngest end of a transect across the oldest portion of the Mesozoic magnetic anomalies, was also considered of particular interest in the attempt to calibrate the age of these anomalies.

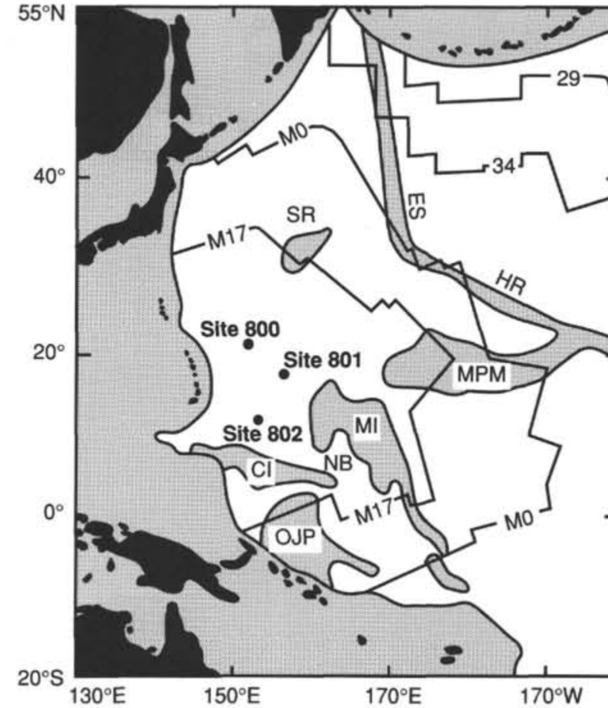

Figure 1. Location of Leg 129 Sites 800, 801, and 802. Bedrock isochrons are determined from magnetic anomaly lineation mapping on the Pacific plate (after Larson et al., 1985) and superimposed on groups of islands, atolls, and guyots in the western Pacific Ocean. (Feature abbreviations are as follows: Caroline Islands (CI), Ontong Java Plateau (OJP), Marshall Islands (MI), Nauru Basin (NB), Mid-Pacific Mountains (MPM), Shatsky Rise (SR), Hawaiian Ridge (HR), and Emperor Seamounts (ES). Jagged contours represent magnetic lineations and unshaded areas represent normal Pacific oceanic crust. Shaded areas represent volcanic edifices with thickened crustal sections, as well as the younger areas beyond the Pacific subduction zones.

An interpretation of the regional seismic stratigraphy combined with what is known from the history of plate motion during the Mesozoic (Lancelot and Larson, 1975; Lancelot, 1978) allowed us to predict that the sediment section would consist of a very thin cover of soft pelagic brown clay resting on a series of chert layers of Late to middle Cretaceous age. The lower part of the section was believed to consist of clay and limestones of Early Cretaceous age, possibly underlain by another series of cherts and/or limestones of Late Jurassic age, and finally by basaltic basement.

OPERATIONS

Approach to the Site

We approached Site 800 from the peak of Himu Seamount on course 52.5° at 6 kt, shooting a seismic line with two 80-in.^{3} water guns (Fig. 4). Our target was a point at 0740 hr

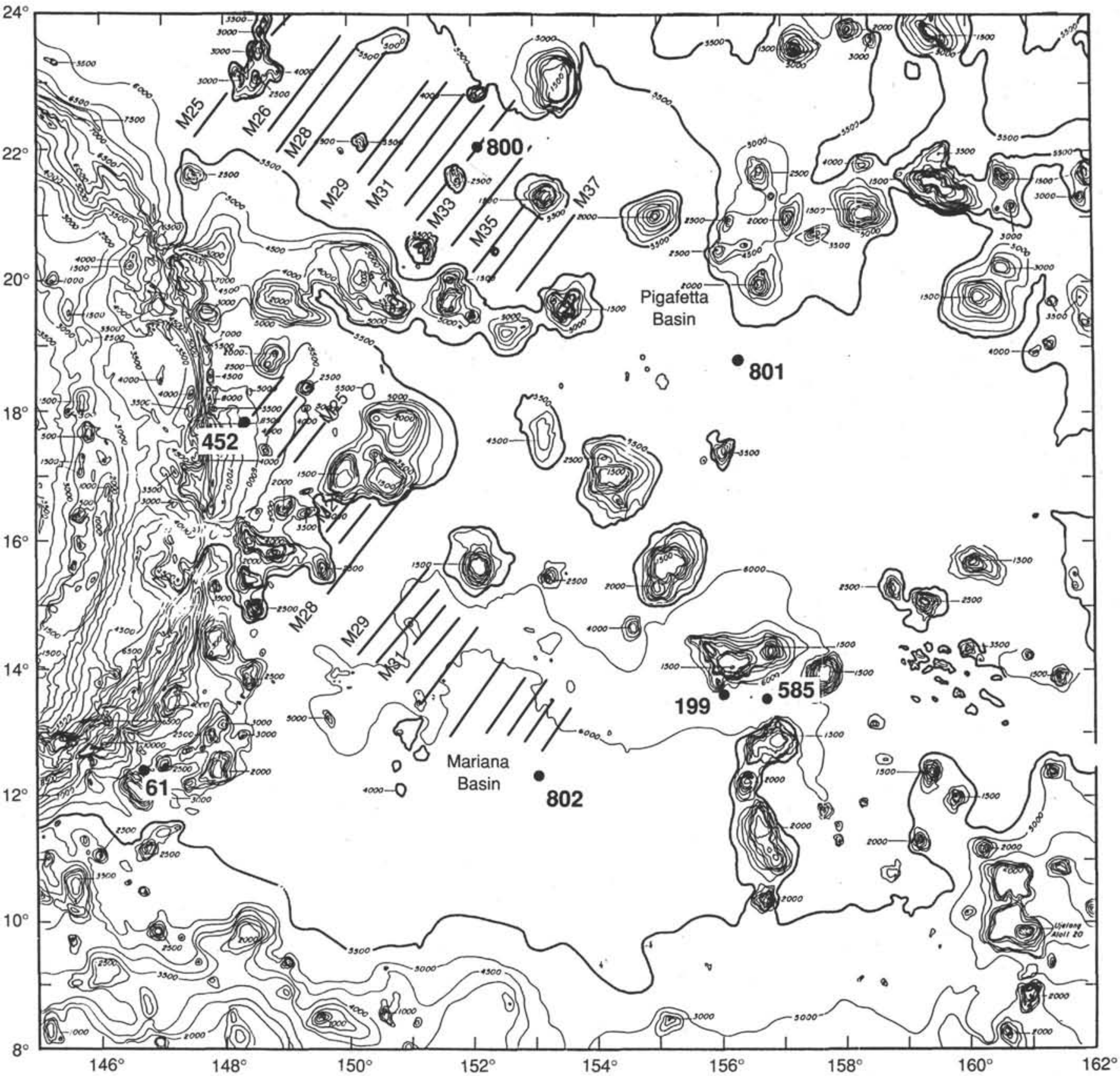

Figure 2. Bathymetry (in meters) of the central western Pacific (M. Angell and C. Brenner, pers. comm., 1990) with location of drill sites. Magnetic anomalies modified from Handschumacher and Gettrust (1985), Tamaki et al. (1987), and Handschumacher et al. (1988).

(Universal Time Coordinated, UTC), 21 August 1989, on MESOPAC II line 3 that trends at about a 45° angle to our approach direction. At 1244 hr, 25 November 1989, when we were still 1.5 miles south of the MESOPAC II target, the water gun and 3.5-kHz records showed a very clear seismic picture (see Figs. 40 and 41, "Site Geophysics and Seismic Stratigraphy," this chapter) comparable or superior to the MESOPAC II profile. We launched the beacon at that location (21°55.408′N, 152°19.386′E, which is slightly different from the final site position). We then continued on a constant heading to cross MESOPAC II line 3 at our original target location where the seismic picture was about the same. We proceeded 2.8 miles beyond the MESOPAC II line where we changed course to 167° and ran 4.3 miles, crossing MESOPAC II again to a point where we could run parallel to MESOPAC II and over the beacon drop site. We changed course to 283° and ran an 8.7-mile line that passed 0.3 mile south of the beacon drop site and trended parallel to MESOPAC II line 3. We then retrieved the seismic gear and returned to the beacon location.

Our first line shows a very clear reflector at 500 ms that extends continuously for 3 miles. The beacon drop site is nearly centered in the middle of the extent of the reflector. The last (cross-strike) line shows that this reflector marks the basement of a narrow basin, with the beacon drop site close to the west basin wall. However, the beacon drop site is also on the deepest location of the basement reflector, and thus probably is close to the optimum location for Site 800.

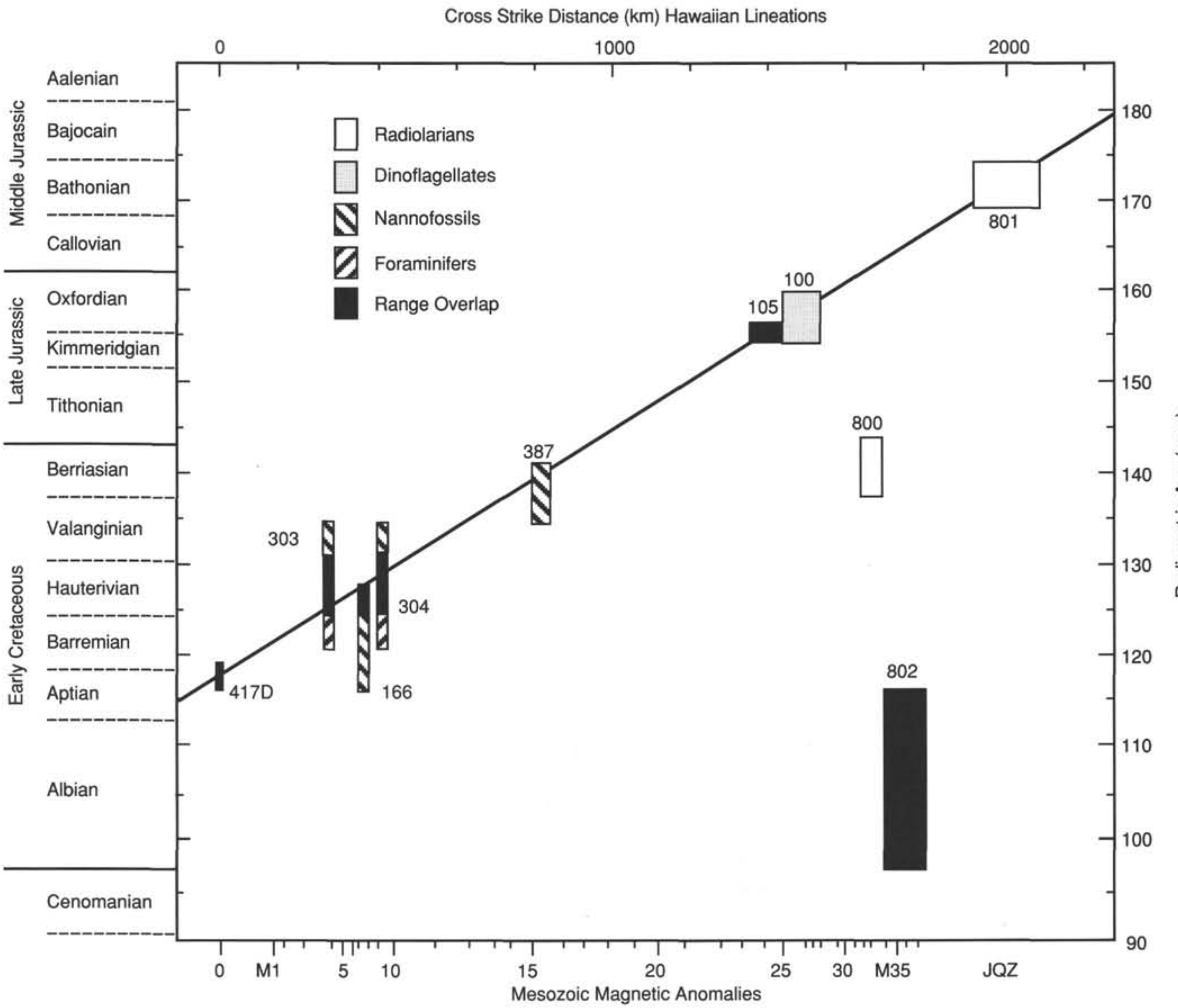

Figure 3. Time calibration plot of the Mesozoic anomalies M0 to M37 and the preceding magnetic quiet zone (JQZ). Magnetic anomalies plotted as cross-strike distance across the Hawaiian lineations for M0 to M25. Anomalies M25 to M37 are normalized to that parameter after Handschumacher et al. (1988). Geologic time scale and radiometric ages are from Harland et al. (1982), as modified by Kent and Gradstein (1985) at the Tithonian/Kimmeridgian boundary. Diagonal line indicates a predicted time scale constrained prior to Leg 129 that closely fits the calibration points. Oldest paleontologic ages in various DSDP holes (numbered) are shown as rectangles. Vertical lengths of rectangles show paleontological age ranges from DSDP *Initial Reports*, except for 100 (Zotto et al., 1987) and 105 (Gradstein and Sheridan, 1983). Horizontal lengths show magnetic age ranges from Larson and Hilde (1975) for DSDP Sites 303, 304, 166, 100, and 105, and DSDP *Initial Reports* for Sites 387 and 417D. Age ranges from Sites 800, 801, and 802 are also shown.

Hole 800A

A bottom-hole assembly (BHA) 154 m long was made up almost completely of 8¼-in. drill collars with a 3-m-long set of Hydrolex jars at 115 m. Total BHA weight was 65,000 lb with 47,000 lb below the jars. A Rock Bit International C4 coring bit was chosen to lead our assault on the Jurassic. This bit consisted of four roller cones with short chisel teeth, tungsten carbide inserts, sealed journal bearings, and inlaid hard metal armor to retard shirt-tail wear.

The corrected seafloor precision depth recorder (PDR) depth at Site 800 is 5697 m to the rig floor. A core was taken from 5693 m of measured drill pipe to account for a theoretical 11 m of pipe stretch. This core was all water. The string was lowered 5 m and the next core taken (Core 129-800A-1R) contained 0.32 m of brown clay. The mud line was established at 5697 m of measured drill pipe, exactly equal to the corrected PDR depth.

As this was a potential reentry site, we next conducted a jet-in test to determine the length of casing that could be washed in. Resistance was met at 38 mbsf, and 40 strokes per min (spm) of pump pressure only produced an additional 2 m of penetration. We concluded that 38 m of conductor casing is the maximum that could be washed in at this location.

Core 129-800A-2R then was taken from 1.0 to 10.6 mbsf. Only a core-catcher sample and a clean core liner were recovered, casting some doubt on our previous mud-line determination. We proceeded to recover a medium to poor

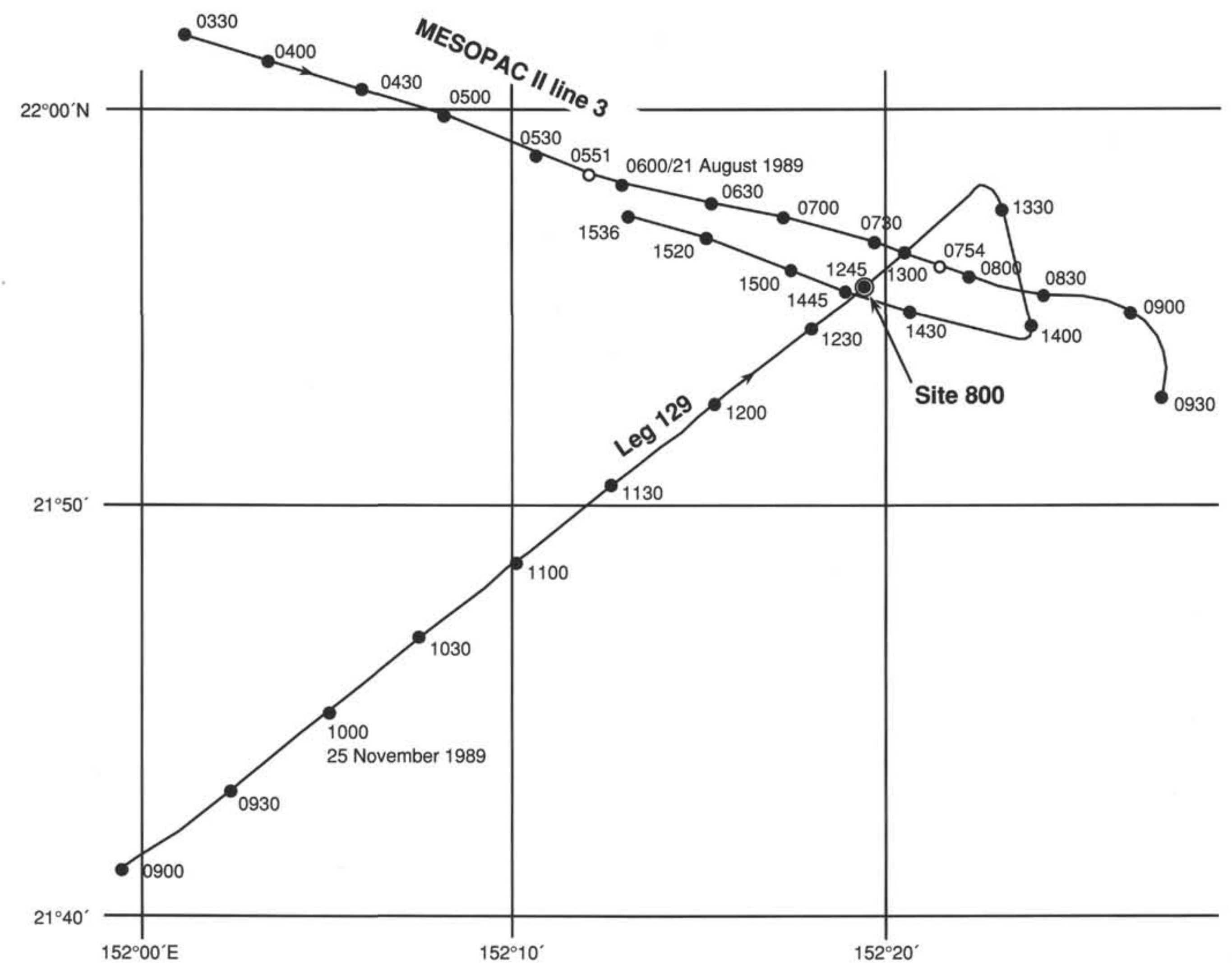

Figure 4. Track chart of expeditions MESOPAC II and Leg 129 showing the location of Site 800. The originally proposed site PIG-1 is located at the intersection of the MESOPAC II and Leg 129 seismic lines approximately 3 km to the northeast of Site 800. Sonobuoy 2m was recorded from 0349 to 0800 hr UTC along MESOPAC II line 3 (Fig. 43). The entire SCS record obtained on approach to Site 800 during Leg 129 is displayed in Figure 40.

percentage of brown clay down to 39.5 mbsf. Core 129-800A-4R (20.2–29.9 mbsf) was determined to be of middle Pliocene to middle Miocene age by a single coccolith, and Core 129-800A-5R (29.9–39.6 mbsf) was Campanian.

The hard zone was met again at 38 mbsf requiring rotation and pump pressure for penetration. Core 129-800A-6R (39.6–49.2 mbsf) and the immediately subsequent cores proved to be red, banded porcellanites and cherts with recovery averaging 5%–10%. Cores required about 30 min to cut with 15,000 to 20,000 lb of bit weight and 20–40 spm of pump pressure. A minor amount of drill string torquing was experienced. The good weather and heave compensator provided a relatively constant weight on bit that made penetration relatively routine. Coring continued in this fashion, although the porcellanites hardened into true cherts, requiring more bit weight and cutting time. Cores 129-800A-10R to -16R were cut with 20,000 to 25,000 lb of weight on bit, 40 spm of pump, and 40–50 rotations per minute (rpm). They each required 40–45 min of cutting time. After Core 129-800A-10R, 15 barrels of mud were pumped into the hole after every third core. The recovered cherts graded down section from red (recrystallized brown clay) to grey chert and silicified limestone. The coring rate averaged 11.8 m/hr through the cherty interval, down to Core 129-800A-24R.

After Core 129-800A-20R, a short wiper trip was run to retrieve our 100-m inventory of knobby drill pipe. On returning to the bottom of the hole, 17 m of soft fill was encountered and cutting torque increased significantly. Starting with Core 129-800A-25R, the cutting rate increased and cutting torque decreased as the formation changed from cherts and silicified limestones to indurated and slightly silicified claystones with occasional volcanic ash.

Recovery on Core 129-800A-26R was nearly 50%, up from 5%–10% in the chert sequence. The hole remained clean (no torque with the bit off the hole bottom) and the bit cutting structure was still intact, as the claystone was recovered as full-gauge core (diameter = 2.28 in.). Beginning with Core 129-800A-26R, we cored through, and recovered a substantial percentage of, a thick section of well-cemented, fine- to medium-grained volcaniclastic turbidites, probably shed from Himu Seamount 40 miles to the southwest. The volcaniclastics contain occasional, deep-water pelagic sediments that are uniformly Aptian in age (as is Himu Seamount) down through Core 129-800A-50R. The coring rate averaged about 20 m/hr through this sequence. Wiper/knobby trips were run after Cores 129-800A-31R and -42R. A drift survey after Core 129-800A-39R measured 3° of hole inclination off vertical.

Cores 129-800A-51R to -55R recovered relatively soft, red claystone that caused some torquing problems of the drill string. Several sweeps of mud were run to combat the problem, and a knobby/wiper trip was run after Core 129-800A-53R.

Coring was relatively rapid until the last 2 m of Core 129-800A-56R, when a very hard formation was encountered. This proved to be hard, red chert in Core 129-800A-56R and the top of Core 129-800A-57R. The bottom of Core 129-800A-57R and the succeeding cores proved to be basaltic dolerite that cored smoothly at the rate of 3–4 m/hr. The basalt was jammed off in Core 129-800A-57R by a deformed, plastic core liner, so we decided to core without liners in the basalt section after that. The hole held up well until the end of Core 129-800A-61R, when it was difficult to pick up the bit off the bottom of the hole. It was decided to run a knobby/wiper trip prematurely to ream out the hole. After laying down the knobby pipe and several stands of regular drill pipe, the drilling line was also slipped, cut, and reterminated. After the wiper trip it was impossible to return to the bottom of the hole, due to a tight spot at 350 mbsf. Apparently the large percentage of clay in the volcaniclastic turbidites was swelling and seizing the BHA. Several attempts to ream through the tight spot were not successful, and we abandoned our attempts to core ahead in this hole. It required several attempts to release the bit for logging at 335 mbsf, probably due to volcaniclastic debris plugging the bit release mechanism.

Standard logging in this hole was conducted in three runs: the quad combination consisting of caliper, natural gamma ray, dual induction, long-spaced sonic, temperature, and lithodensity tools; the geochemical string consisting of induced-gamma, aluminum clay, neutron, and natural gamma ray tools; and the formation microscanner (FMS) consisting of FMS and natural gamma-ray tools. At the start of the quad combination run, it was discovered that the wireline heave compensator was inoperative despite a service call from its designer during the Singapore yardwork. We were not able to make repairs during the logging period and operated without the compensator in relatively calm seas. All logs were run up to 45 mbsf. The quad combination bottomed at 294 mbsf, the geochemical string at 315 mbsf, and the FMS at 214 mbsf. Logging took a total of 28 hr, after which we pulled out of the hole and proceeded to proposed site PIG-3A at 1103 hr UTC on 5 December 1989.

LITHOSTRATIGRAPHY AND SEDIMENTOLOGY

The stratigraphic sequence penetrated at Site 800 consists predominantly of pelagic clays, cherts and porcellanites, limestones, volcaniclastic claystones, siltstones, and sandstones. On the basis of the distribution of these lithologies, the sedimentary column between 0 and 498.1 mbsf has been divided from top to bottom into five lithologic units: a pelagic brown clay unit, a brown porcellanite and chert unit, a gray siliceous limestone and chert unit, a volcaniclastic turbidites unit, and a siliceous and pelagic clay unit. Intrusive dolerite sills that contain minor amounts of sediment were recovered between 498.1 and 544.5 mbsf and are described as Unit VI. The main lithologic facies, mineralogical composition, and depositional trends are shown in Figure 5.

Lithologic Units

Unit I. Cores 129-800A-1R to -6R (0 to 38.0 mbsf): Pelagic Brown Clay; Pliocene to Upper Cretaceous

Unit I, 38 m thick, consists of soft- and fine-grained pelagic brown clay. Its homogeneous character is probably related to the high degree of drilling disturbance. The pelagic clay is composed of clay aggregates and abundant iron oxide globules and granules which are similar to those occurring in deep-sea pelagic clay of abyssal plains and often described as RSO's ("red-brown semi-opaque objects," Yeats, Hart, et al., 1976). Sediment colors range from a very dark reddish brown in the highest four cores (129-800A-1R to -4R) to lighter hues as yellowish brown in the lowest core, 129-800A-5R. Detrital phases, represented by quartz and scarce feldspar are more abundant in the surface deposits, whereas the zeolites (phillipsite) increase in the lower part of the unit.

The possible ages of this sequence are derived from scarce foraminifer, nannofossil, and radiolarian populations, and range from middle Pliocene to middle Miocene in the upper dark brown deposits (Cores 129-800A-1R to -4R) to late Campanian in the lower, lighter deposits from Core 129-800A-5R. A long hiatus probably ranged from the Late Cretaceous to middle Miocene. The very low sedimentation rate for this unit, estimated to be lower than 0.5 m/m.y., is typical of pelagic deep-sea brown clays, deposited below the carbonate compensation depth (CCD). This facies is well represented in the entire deep northern Pacific Ocean.

On top of the subsequent core (129-800A-6R) at 39.6 mbsf, a 10-cm-thick layer of light brown clay occurs, which is probably uphole contamination from drilling operations.

Unit II. Cores 129-800A-6R to -9R (38 to 78.2 mbsf): Brown Porcellanite and Cherts; Campanian to Turonian

Unit II, 40.2 m thick but poorly recovered, is predominantly composed of porcellanites in gradational transition to cherts at various scales. The porcellanite and chert are very dark brown to brown in reddish and yellowish hues. Patches of chert cut across millimeter-scale laminations in the porcellanite (Fig. 6). Porcellanite prevails in the upper part of the unit and radiolarian cherts become more abundant downward. A zeolitic claystone occurs in interval 129-800A-8R-1, 35–40 cm. The main mineralogical composition of this facies consists of variable amounts of quartz and opal-CT.

Radiolarians provide late Campanian to early Campanian and Turonian ages. Therefore, the sedimentation rate of this sequence is estimated to be <2 m/m.y., a relatively low rate.

Unit III. Cores 129-800A-10R to -25R (78.2 to 228.6 mbsf): Gray Siliceous Limestones and Cherts; Albian-Cenomanian

A major change in color, from the reddish and yellowish brown cherts of Unit II to olive gray and gray cherts and porcellanites determines the top of Unit III. This unit, 150.4 m thick, consists of cherts and siliceous limestones. The cherts contain radiolarians filled with opal and chalcedony; some are pyrite-replaced (Core 129-800A-10R). The texture is aphanitic, with a waxy luster and smooth, conchoidal fracture. In the upper part of the unit, the limestone layers are locally replaced by cross-cutting chert, with variable degrees of silicification (Fig. 7). The discontinuous laminations are often deformed and show slight bioturbation. Siliceous limestone becomes more abundant, as an interlayered major lithology, in Cores 129-800A-13R through -22R (Figs. 8 and 9A). Rare thin layers of soft micrite with nannofossils occur within Core 129-800A-17R. Foraminiferal fauna are mainly redeposited (see "Biostratigraphy" section, this chapter). At 181.4 mbsf (Core 129-800A-21R), the siliceous limestone and nannofossil

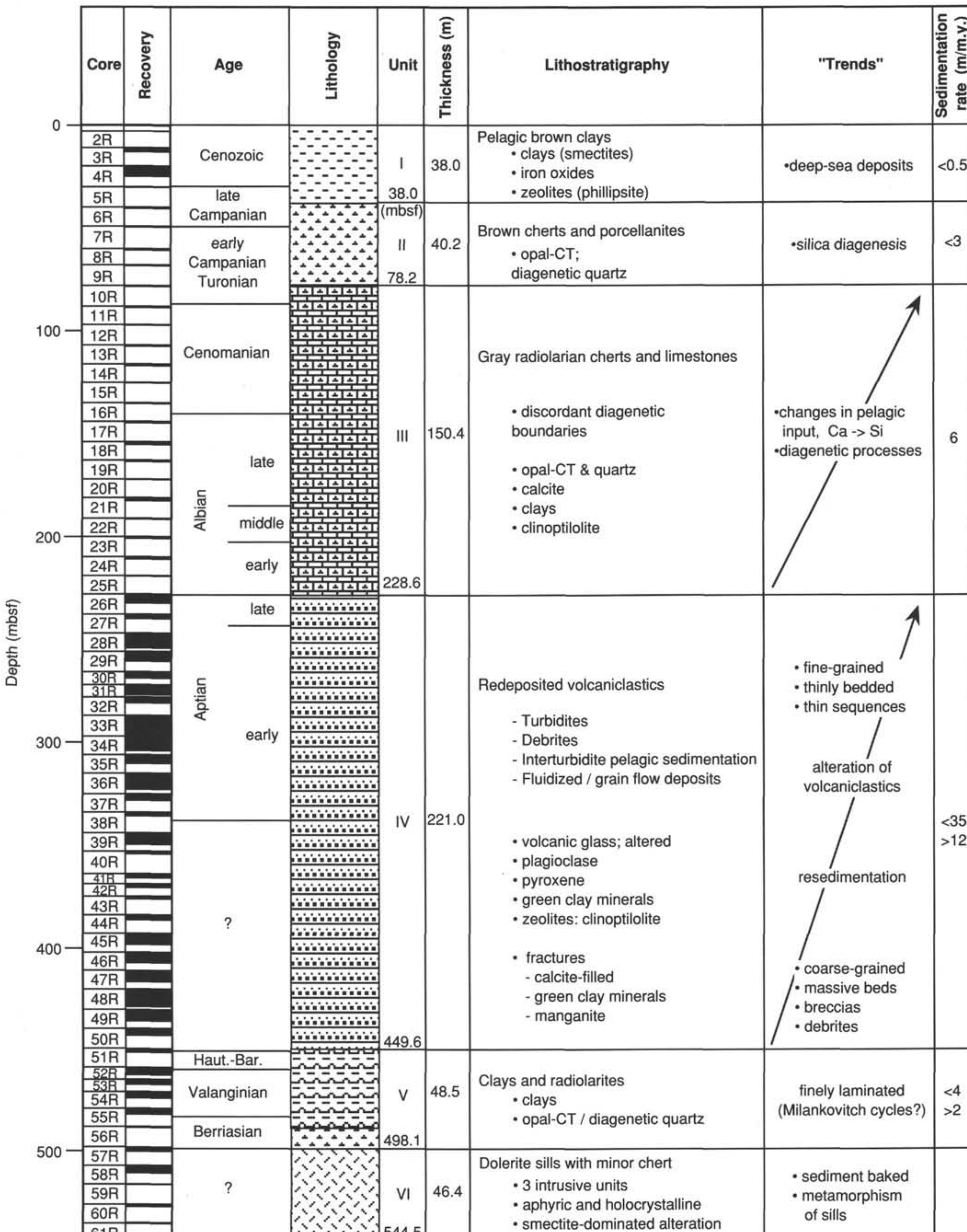

Figure 5. Composite lithologic units at Hole 800A and summary of the main mineralogical composition and sedimentary trends established for each unit.

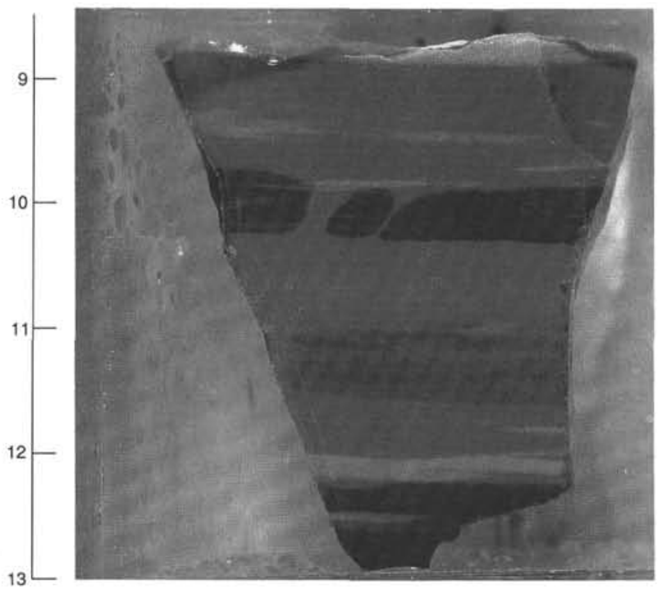

Figure 6. Sample 129-800A-9R-1, 9–13 cm, from Unit II. Porcellanite (light reddish brown, 5YR 6/4) with thin planar bedding and local replacement by chert.

chalk are microlaminated. Variations in grain size which form the laminations are related to the abundance of radiolarians and to the degree of dissolution and cementation of the siliceous microfossils. The gradational transitions between the limestone or porcellanite and chert, as nodules or layers, are well established by thin-section observations (Fig. 9B, -C). In the lower part of the unit (Cores 129-800A-22R through -25R), a few volcanic clasts and clinoptilolite zeolite were detected (in smear slides, thin sections, and XRD). The volcaniclastic input within the base of the silicified limestone, expressed as fine-grained clasts and glass, establishes a transitional zone between the siliceous limestone and chert and the underlying volcaniclastic deposits (Unit IV).

The main mineral composition of the sediment from Unit III, determined by XRD analyses, ranges from prevalent quartz and opal-CT contents in the upper part of the unit (Cores 129-800A-10R to -17R), to higher calcite (Core 129-800A-22R), followed by higher clay contents in the lower levels (Cores 129-800A-23R to -25R).

Nannofossils as well as radiolarian assemblages indicate an age of Cenomanian for the top of the unit and early Albian for Cores 129-800A-21R to -25R (see "Biostratigraphy" section, this chapter). Thus, the mean sedimentation rate estimated for the whole Unit III is approximately 6 m/m.y. A possibly lower sedimentation rate is suspected in the lowest part of the unit, from Cores 129-800A-21R-2 through -25R (182.5–228.6 mbsf), because it is entirely middle to early Albian in age. A possible hiatus occurs between these Albian deposits and the underlying Aptian sediments.

Unit IV. Cores 129-800A-26R to -50R (228.6 to 449.6 mbsf): Redeposited Volcaniclastic Sandstone to Claystone; Aptian

Unit IV consists of a 221-m-thick sequence of interbedded clays and claystones, silty clays, silty sandstones, and sandstones, mainly redeposited ash, and tuff with scarce biogenic phases. This unit is described as volcaniclastic turbidites and redeposited volcaniclastic sandstone. Several intervals are distinguished on the basis of the grain size, the thickness of the upward-fining beds, and carbonate content which were

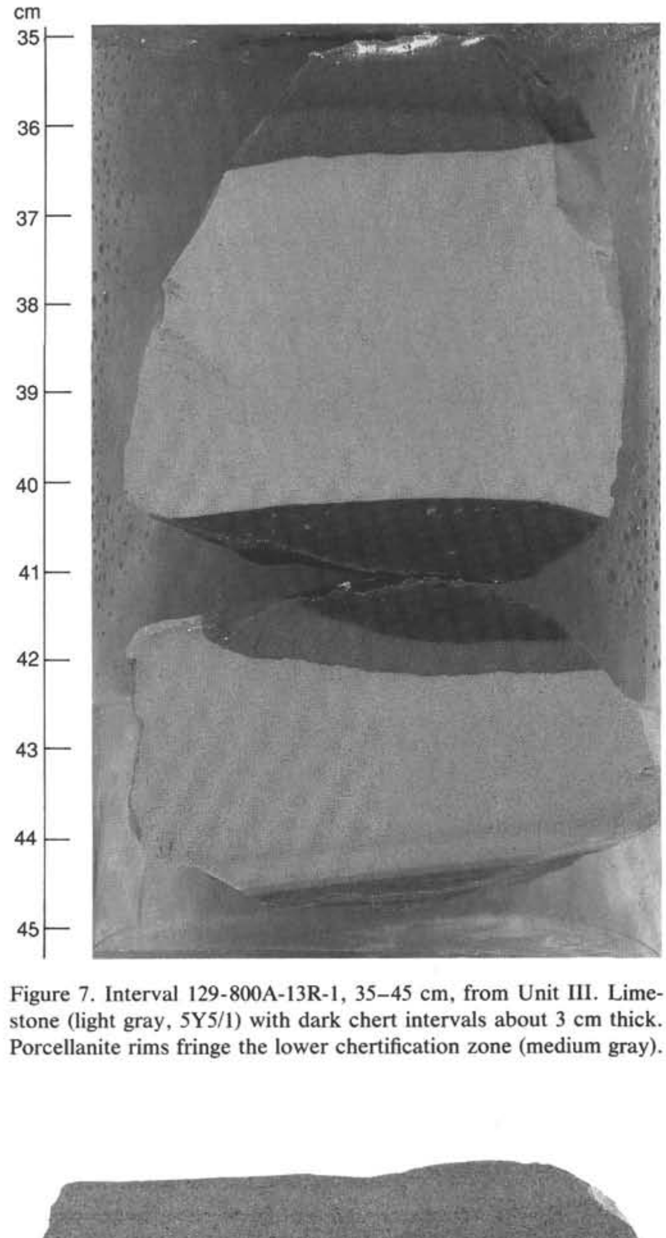

Figure 7. Interval 129-800A-13R-1, 35–45 cm, from Unit III. Limestone (light gray, 5Y5/1) with dark chert intervals about 3 cm thick. Porcellanite rims fringe the lower chertification zone (medium gray).

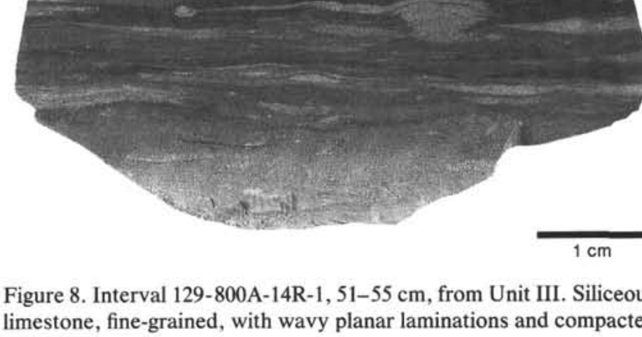

Figure 8. Interval 129-800A-14R-1, 51–55 cm, from Unit III. Siliceous limestone, fine-grained, with wavy planar laminations and compacted possible bioturbation features.

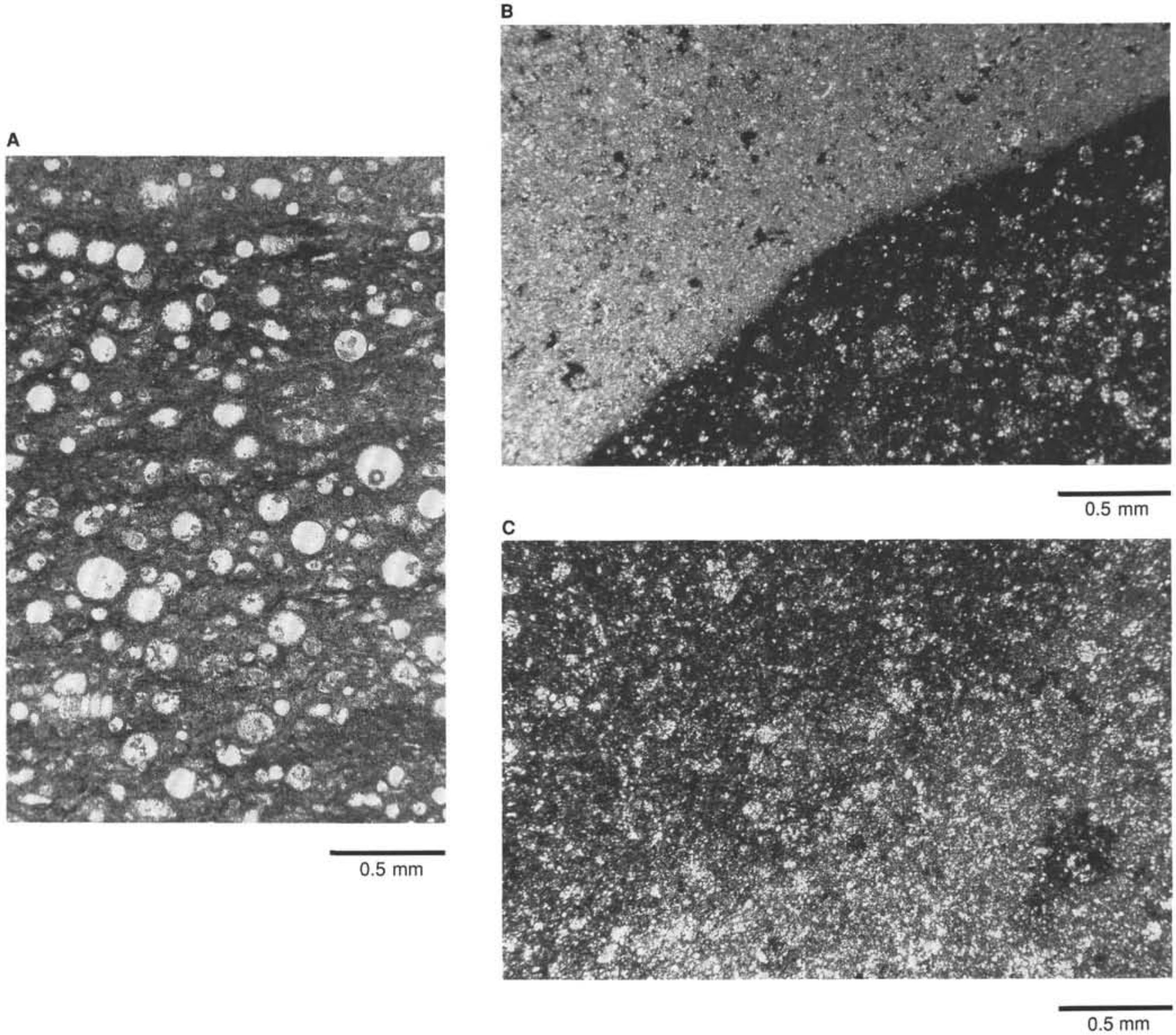

Figure 9. Photomicrographs of major facies from Unit III. Scale bar = 0.5 mm. **A.** Typical siliceous radiolarian micritic limestone of Unit III. The matrix is composed of micritic calcite and opal-CT. Radiolarians are filled chiefly with chalcedonic quartz, locally with opal-CT. Sample 129-800A-13R-1, 29–32 cm. **B.** Chert nodules in limestones are usually surrounded by an intermediate zone of porcellanite (cf. Fig. 7). The photomicrograph (cross nichols) shows the sharp diagenetic boundary between radiolarian micritic limestones (upper left) and radiolarian opal-CT porcellanite (lower right). Sample 129-800A-15R-1, 38–40 cm. **C.** Same nodule, radially inward, as Figure 9B. Gradational diagenetic boundary between radiolarian opal-CT porcellanite (upper left) and microcrystalline quartz chert (lower right). Sample 129-800A-13R-1, 38–40 cm.

determined by macroscopic, microscopic, XRD, or chemical investigations.

The upper part of the unit (Core 129-800A-25R, 50 cm, to Core 129-800A-31R) is composed of alternating, repeated, upward-fining beds of dark bluish to greenish grays. The thicknesses of these individual beds average about 50 cm (Figs. 10 and 11). In this part of the unit volcaniclastic siltstones grade upward to claystones that contain less than 10% radiolarians and scarce nannofossils. The graded beds are finely laminated, with load casts and convolute layers, and cross or planar laminations. Rare fractures are quartz-filled. Some of the turbidite beds grade upwards to olive brown radiolarian pelagic claystone with local bioturbation features (Fig. 12). Some turbidite beds begin with a thin horizon of calcareous, volcaniclastic, poorly-sorted, sandy siltstone (Fig. 11). The main components of the turbidite deposits are volcanic glass, igneous rock fragments, feldspars, zeolites (clinoptilolite), calcite, and opaline silica; the ground mass is made up of green clay minerals.

From Core 129-800A-32R through -38R the graded beds become coarser and thicker, consisting of gray gritstone to fine-grained sandstones, and to reddish brown claystones or clayey radiolarites. Calcareous claystone increases below Core 129-800A-36R. Several intervals show reversely graded bedding. Ripple laminations, cross laminations, and calcite veins are the main sedimentary and structural features. Reduction fronts often extend from the gray-green sharp base of turbidites beds downward into the underlying reddish brown

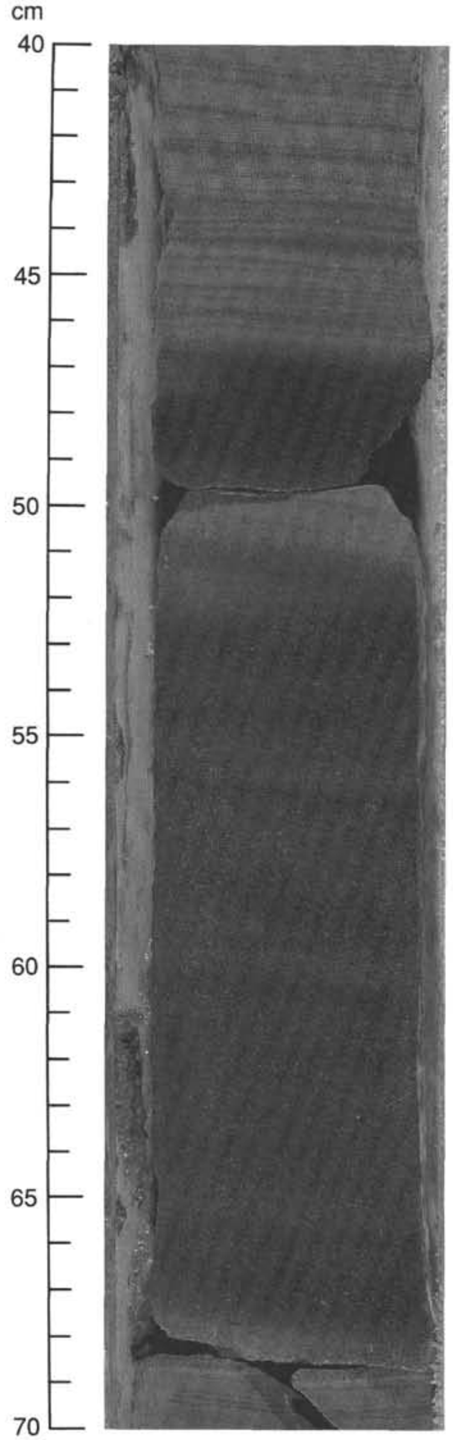

Figure 10. Typical, small, fine-grained, fining-upward turbidite bed of volcaniclastics ranging from dark gray (N4) sandy siltstone to lighter blue-green (5BG 5/1) claystone. This lithology comprises mainly the uppermost part of the Unit IV. Interval 129-800A-26R-3, 40–70 cm.

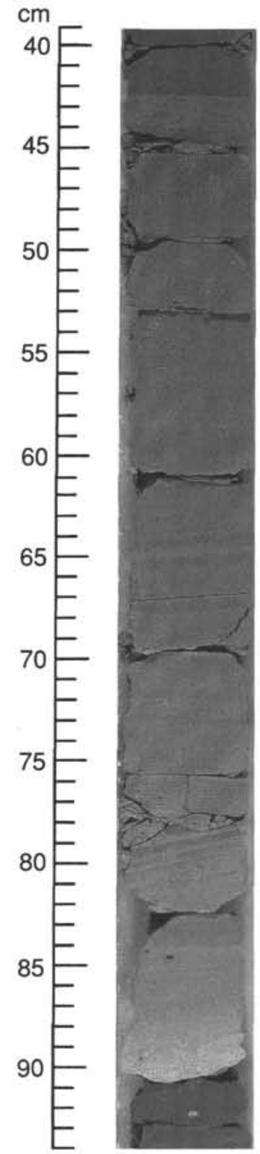

Figure 11. Within the upper part of Unit IV, some turbidite beds are made up of poorly sorted, yellowish gray (5Y 8/1) calcareous siltstone to light greenish gray (5GY 7/1) laminar volcaniclastic and clayey beds. The composition of the basal sand is calcareous microfossils, inorganic calcite, and volcaniclastic fragments. Interval 129-800A-28R-3, 40–90 cm.

claystones. The turbidites increase in thickness to approximately 0.8–1 m. The main composition of the deposits is the same as the overlying fine-grained beds, but with higher calcium carbonate contents. The calcareous sandstone recovered in Core 129-800A-32R-1, 80–125 cm, contains up to 50% red algae fragments (Fig. 12C, -D). In the surrounding area of Site 800, similar calcareous compounds were described by Witman et al. (1986) and Haggerty and Premoli-Silva (1986). These fragments are also similar to the debris studied by McKenzie et al. (1980, and references therein) on northwestern Pacific seamounts and attributed to the "coral-algal facies" from low latitudes. In interval 129-800A-38R-1, 25–40 cm, numerous large fractures are filled by very a well-crystallized manganese hydroxide, identified as manganite (MnOOH). Dendrites are also abundant on fracture surfaces.

From Core 129-800A-39R through -46R, the prevalent lithologies are volcaniclastic sandstones, claystones, and poorly sorted sandstone breccia, with less frequent claystone horizons than above. The breccia facies shows numerous clasts of finely laminated claystone or radiolarite, poorly sorted sandstone and some volcanic rock fragments; trains of clasts are randomly oriented and some may represent debris flows (Fig. 13). The finest claystones and radiolarites contain

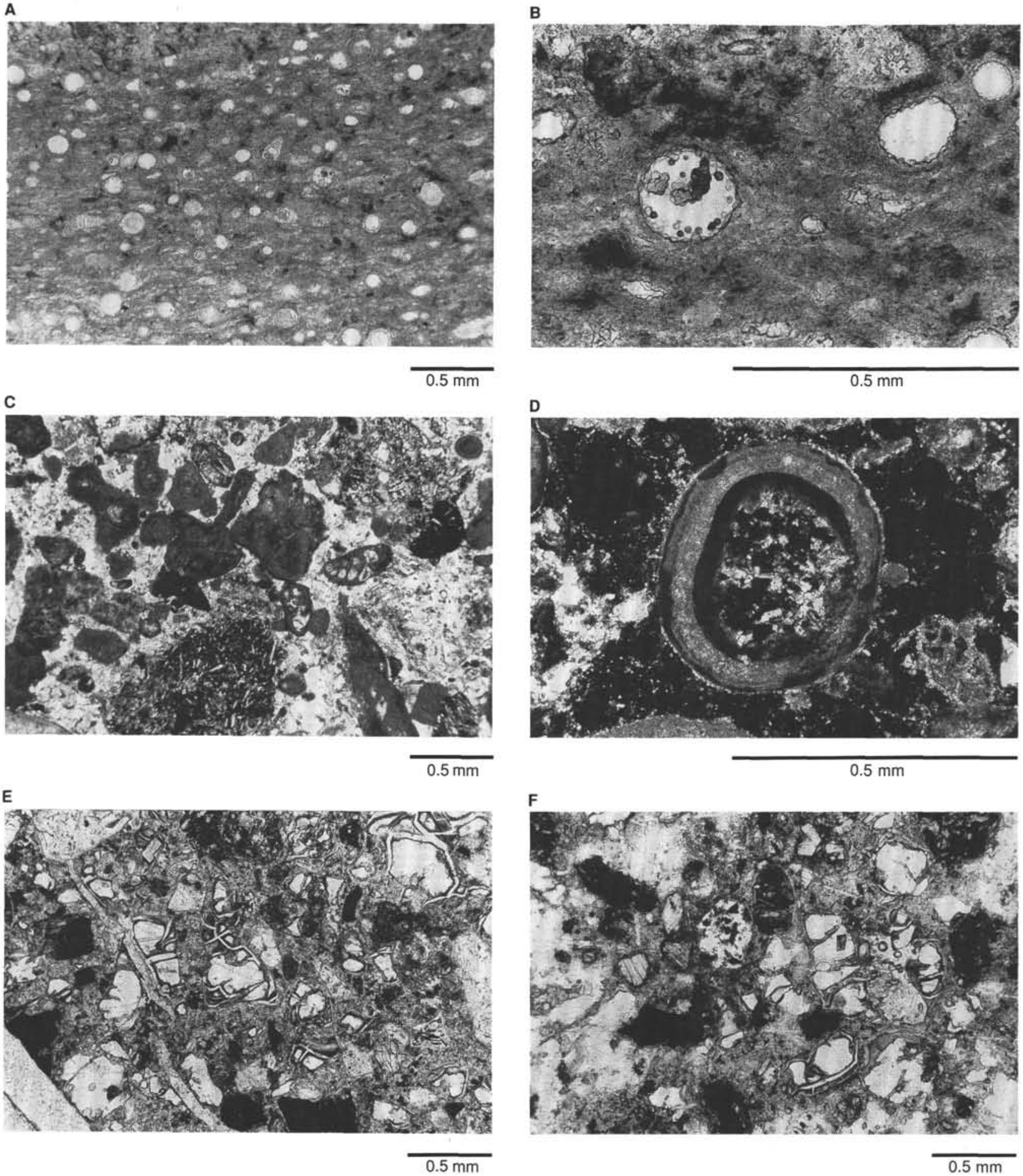

Figure 12. Photomicrographs of the major sedimentary facies from Unit IV. Scale bar = 0.5 mm. **A.** Background pelagic sedimentation between the redepositional events is mainly radiolarian-rich. The facies is typical radiolarian opal-CT porcellanite with a clay and opal-CT matrix. Sample 129-800A-30R-1, 34–37 cm. **B.** Close-up from previous thin section. Radiolarians tests are replaced by opal-CT and partially filled by opal-CT lepispheres. The clear remainder of radiolarian internal tests are filled with chalcedony. Sample 129-800A-30R-1, 34–37 cm. **C.** Calcareous volcaniclastic turbidite beds (cf. Fig. 11) contain abundant biogenic components. The fragments of foraminifers and micritized red algae are associated with ooids and volcaniclasts. Scattered fragments of *Orbitolinidae* foraminifers in other parts in the thin section are typical, middle Cretaceous neritic forms. Sample 129-800A-32R-1, 117–118 cm. **D.** Ooid nucleated on volcaniclast, and a foraminifer similar to *Bolivinopsis* sp. in calcareous volcaniclastic turbidites. Same sample as Figure 12C. Cross nichols. **E.** Volcaniclastic sandstone turbidites with prevalent volcanic glass, igneous rock fragments, clinopyroxene, and calcite. Sample 129-800A-37R-2, 123–128 cm. **F.** Volcaniclastic, medium-grained, dusky green (5G 3/2) sandstone turbidites are composed mostly of microphyric glass fragments replaced by clays, plagioclase, clinopyroxene clasts, black tachylite, iron-oxides, clay minerals, and secondary calcite. Sample 129-800A-47R-2, 64–67 cm.

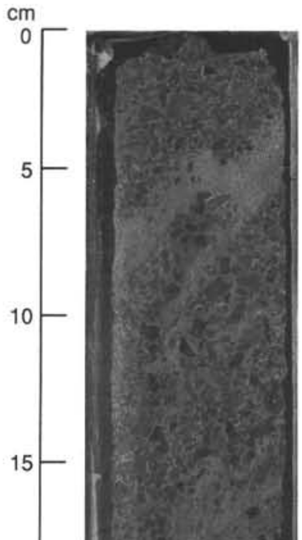

Figure 13. Lower part of lithologic Unit IV. The basal horizon of the thicker turbidite beds are often composed of a breccia of reddish brown (5YR 4/4) claystone clasts within a greenish gray (5G 5/1), sandy, volcaniclastic matrix. The clasts are angular to sub-rounded, 0.2–1.5 cm in size, and without preferential orientation. The distribution suggests a debris flow deposit. Interval 129-800A-2R-1, 0–40 cm.

up to 50% radiolarians. Several generations of fractures occur. Some horizons are oxidized, resulting in medium gray and grayish red hues. The bulk mineralogy of the facies consists of quartz, feldspar, and clay minerals and few iron oxides. The fracture fillings are mainly calcite and/or dark green clay minerals such as palygorskite. The volcaniclastic sandy horizons are composed of unvesiculated glass often altered to clays, pyroxene clasts, and very few trachylite fragments within a clayey matrix (Fig. 12E, -F).

The lowest part of Unit IV (Cores 129-800A-47R to -50R) is a massive, dusky green, sandy volcaniclastic deposit containing igneous rock fragments, claystone fragments, and prevalent fresh volcanic glass shards; the latter are scarcely and locally palagonitized. Breccia horizons are frequent, and numerous redox fronts are expressed by sharp variation in colors ranging from green to brown. The clay-filled fractures are also more frequent. At interval 129-800A-48R-5, 107–118 cm, a calcareous sandstone contains moderately sorted carbonate grains within a clay matrix.

The calcareous microfauna found within the turbidite deposits of Unit IV indicate an early to late Aptian age for the upper part of the unit (Core 129-800A-25R to -37R) and a high sedimentation rate of 12–35 m/m.y. is estimated from the ages of the under- and overlying sediments (Fig. 5). A hiatus possibly occurred during the Barremian, probably reflecting the drastic change in energy between the volcaniclastic deposits (Unit IV) and the underlying siliceous sediments (Unit V).

Unit V. Core 129-800A-51R to Section 129-800A-57R-1, 10 cm (449.6 to 498.1 mbsf): Clayey Radiolarites to Siliceous Claystones; Valanginian-Barremian

A distinct change in lithology distinguishes Unit V from the previous volcaniclastic and turbiditic deposits. This unit, 48.5 m thick, consists of microlaminated clayey radiolarites and siliceous claystones (Fig. 14). The sediment displays scarce green reduced zones in the mostly dark red to light red alternating beds. The mean thickness of the regularly alternating light-colored radiolarite (up to 85% radiolarians) and red claystone layers is about 6 cm. The mineralogical composition consists of varying concentrations of silica and clay minerals, with small amounts of feldspar (XRD). Frequent thin coatings of manganese oxide cut across or follow the laminations (Core 129-800A-53R to -54R). Bioturbation is common throughout the unit. Common, thin, silica-filled fractures cross-cut the layers in the lowest part of unit (Core 129-800A-55R). Within the interval from Core 129-800A-56R to interval 129-800A-57R-1, 0–10 cm, a grayish brown chert bed, with subtle laminations, directly overlies the first recovered igneous rocks.

Radiolarian assemblages indicate Hauterivian-Barremian to Berriasian ages. The sedimentation rate of the whole sequence of clays and radiolarites is estimated to be 2–4 m/m.y.; this sedimentation rate is low compared to average recent biogenic pelagic sedimentation rates of 5–10 m/m.y.

Unit VI. Section 129-800A-57R-1, 10 cm, to Core 129-800A-61R (498.1 to 544.5 mbsf): Dolerite Sills and Cherts; Berriasian

Unit VI, the lowest lithologic unit recovered at Site 800, is composed of igneous rocks with one thin, interlayered chert horizon. The igneous rocks are described as intrusive dolerite sills (see "Igneous Petrology" section, this chapter). The dolerite is aphyric, non-vesicular, hyalocrystalline, and divided into three sub-units based on macrotextural variations and the presence of a chert sedimentary interlayer. All dolerite units are moderately to highly altered, dominated by secondary smectites, iron oxides, and carbonate, together with minor proportions of sericite, chlorite, celadonite, zeolite, actinolite, and biotite.

The interlayered sediments at interval 129-800A-58R, 30–45 cm, consist of dark reddish brown chert and radiolarite. They exhibit thin laminations similar to that of the chert layer above the dolerite (Core 129-800A-56R).

Thin-Section and XRD Data from Sedimentary Rocks

Detailed descriptions of 79 thin sections were used to estimate the various major and minor lithologies and have been incorporated into the above lithologic descriptions. XRD analyses from 38 samples (see "Explanatory Notes" chapter, this volume) from both the dominant or minor lithologies

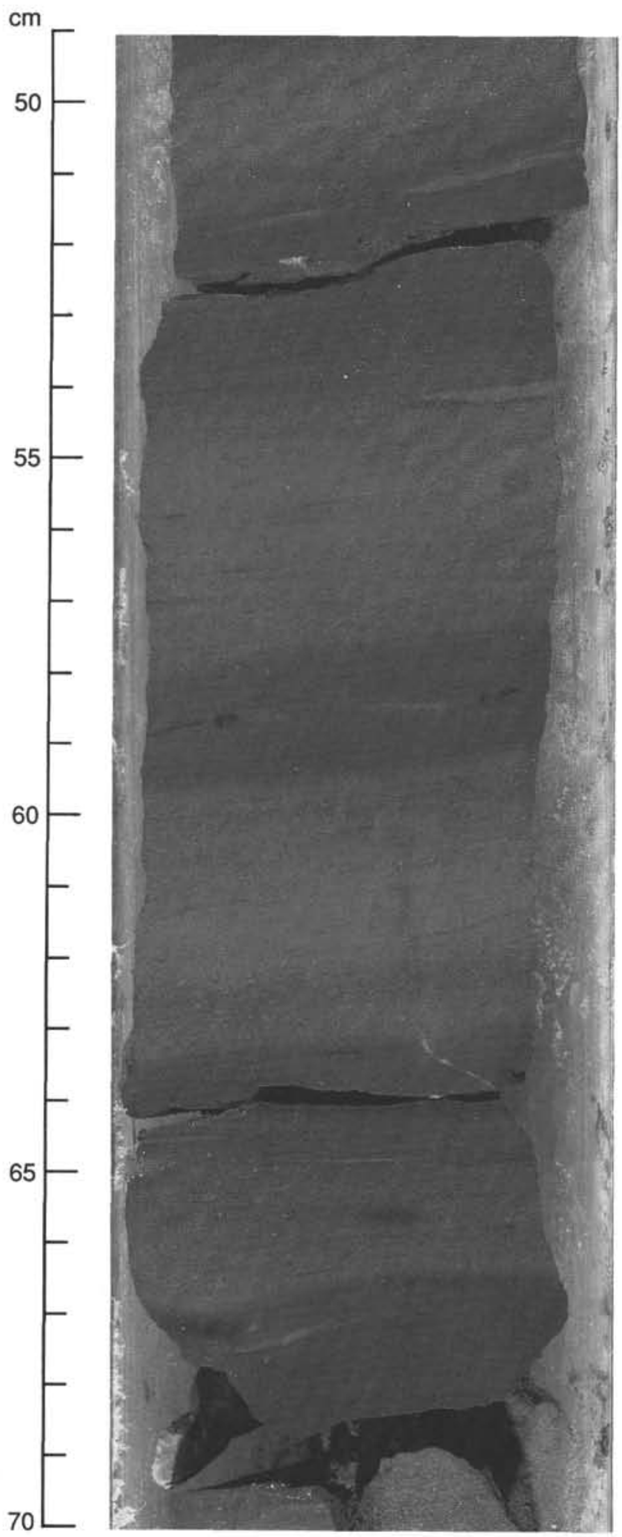

Figure 14. Interbedded, microlaminated, clayey radiolarites (lighter layers as brown, 7.5YR 4.5/2–5/5) and siliceous claystones (dark brown layers, 7.5YR 3/1) form lithologic Unit V. The frequent thin fractures are silica-filled. The microlaminations are delineated by black manganese oxide concentrations. Interval 129-800A-55R-2, 50–70 cm.

encountered in the various facies were selected to distinguish the relative mineralogic abundances and trends of these sediments, and to attempt the determination of specific features such as fracture fillings or thin lamination. Several trends can be observed in these data:

1. The nature of the zeolites. Phillipsite is present in the soft pelagic brown clay facies (Unit I), in clinoptilolite in the siliceous limestones (Unit III), and in the volcaniclastic turbidites and sandstones (Unit IV). The occurrence of these secondary silicates appears related to diagenetic processes.
2. Downhole increase in calcite and clay mineral contents, in the lowest part of Unit III. These variations in calcite and clay contents are inferred to represent a gradual change in biogenic input and an increasing silicification through diagenetic processes.
3. Composition of the sandstone and claystone layers in the turbiditic deposits (Unit IV). Higher plagioclase and pyroxene contents are found in the former, and higher clay minerals and clinoptilolite contents in the latter. The XRD data, limited to the peak values files ranging from between 2° to 40° 2θ, is not sufficient for the determination of specific clay minerals.
4. Barite occurs in some sampled intervals, such as the lowest part of the pelagic brown clays and interbedded claystones within the porcellanite and chert of Unit II. The widespread occurrence of barium-rich phases in pelagic deposits is often related to early diagenetic evolution of biogenic silica (dissolution-recrystallization processes).

Carbonate Contents

Carbonate content data from selected samples were obtained following the method described in the "Explanatory Notes" chapter (this volume). Results are given in Table 2 and represented in Figure 15.

The calcium carbonate contents are very low, as expected, in the pelagic brown clay and underlying brown chert, and in the basal siliceous deposits (Units I, II, and V).

The sediments from Units III and IV contain variable amounts of calcium carbonate related to the primary nature of the lithologic facies and their subsequent diagenetic evolution. Thus, in Unit III, the interlayering and transitions between limestones, siliceous limestones, and cherts are well-documented. For example, a progressive downward increase of carbonate content from limestone to underlying chert is established from the data of Cores 129-800A-14R to -17R (Table 2). The higher contents (>80%) are reached in samples from chalk and limestone horizons within Cores 129-800A-19R and -20R. The main trend in this unit, composed predominantly of biogenic deposits, is a slight decrease in the number of carbonate layers and overall carbonate content from bottom to top.

The redeposited volcaniclastics forming Unit IV contain very little calcium carbonate (<10%), except for a few horizons occurring in the middle of the sequence (Cores 129-800A-32R and -33R), where the turbidite beds are coarse-grained. The carbonates are described mainly as reworked shallow-water biogenic fragments. Within turbidite beds, the coarser layers show higher calcium carbonate content than the overlying claystone layers. Fine-grained claystone horizons (i.e., interval 129-800A-39R-2, 41–43 cm) show relatively high calcite content, corresponding to the occurrence of numerous fracture fillings.

Sedimentological Implications

The lithological and mineralogical description of the successive lithologic units allow us to define major trends in the sedimentary history of Site 800 (Fig. 5) in relation to the

Table 2. Carbon carbonate, expressed as $CaCO_3$, organic carbon, and sulfur contents of sediments from Hole 800A.

Core, section, interval (cm)	Depth (mbsf)	$CaCO_3$ (wt%)	Organic carbon (wt%)	Sulfur (wt%)	Lithology
129-800A-					
3R-1, 82–85	11.42	0.3	0.03	0.10	Pelagic clay
4R-1, 115–118	21.35	0.4	0.04	0.12	Pelagic clay
4R-2, 25–30	21.95	0.6	0.21	0.09	Pelagic clay
4R-3, 58–60	23.78	0.5	0.02	0.11	Pelagic clay
6R-1, 35–37	39.95	0.1			Pelagic clay
8R-1, 35–36	59.25	0.1	0.09	0.02	Chert
8R-1, 36–37	59.26	0.2	0.14	0.01	Chert
8R-1, 37–38	59.27	0.1	0.05	l.d.	Chert
8R-1, 56–57	59.46	0.1	0.05	0.01	Chert
9R-1, 9–12	68.59	0.1			Chert
10R-1, 7–8	78.27	l.d.	0.04	0.58	Chert
10R-1, 32–34	78.52	0.1			Chert
12R-1, 21–25	97.51	18.2	0.14	l.d.	Siliceous limestone
13R-1, 62–64	107.42	31.7			Siliceous limestone
14R-1, 1–3	116.21	0.2			Chert
14R-1, 92–93	117.12	0.2	0.09	0.01	Chert
15R-1, 36–38	125.76	27.3	0.08	l.d.	Siliceous limestone
16R-1, 45–46	135.35	21.2	0.07	l.d.	Siliceous limestone
17R-1, 47–49	144.67	37.2			Siliceous limestone
17R-1, 63–64	144.83	23.3	0.18	l.d.	Siliceous limestone
18R-1, 88–9	154.58	0.1	0.13	l.d.	Chert
18R-1, 104–105	154.74	49.3	0.21	l.d.	Limestone
18R-1, 128–1130	154.98	0.1			Chert
19R-1, 23–25	163.13	29.4			Siliceous limestone
19R-1, 52–53	163.42	88.1	0.53	l.d.	Limestone
21R-1, 1–2	181.31	0.4			Chert
21R-1, 135–137	182.65	81.7			Limestone
22R-1, 22–23	191.22	86.8			Limestone
22R-1, 25–27	191.25	44.6			Limestone
23R-1, 18–20	200.68	8.4			Silicified limestone
23R-1, 53–55	201.03	44.1			Limestone
23R-1, 68–69	201.18	0.4			Chert
23R-1, 90–91	201.40	21.1			Silicified limestone
24R-1, 86–87	210.76	13.6			Silicified limestone
24R-1, 120–122	211.10	22.5			Silicified limestone
25R-1, 11–12	219.41	19.1			Silicified limestone
25R-1, 31–33	219.61	0.3			Chert
26R-1, 114–115	229.74	5.8	0.12	l.d.	Volcanic turbidite, fine
26R-2, 140–148	231.50	5.3	0.05	l.d.	Volcanic turbidite, fine
26R-3, 54–56	232.14	1.4			Volcanic turbidite, fine
26R-CC, 10–12	232.84	0.5			Volcanic turbidite, medium
27R-1, 16–18	238.16	4.1			Volcanic turbidite, fine
27R-1, 97–99	238.97	0.3	0.04	l.d.	Volcanic turbidite, fine
27R-1, 140–150	239.40	2.0	0.01	l.d.	Volcanic turbidite, medium
28R-1, 19–20	247.39	4.2	0.07	l.d.	Volcanic turbidite, medium
28R-1, 33–35	247.53	6.6			Volcanic turbidite, medium
28R-2, 55–56	249.25	0.6			Volcanic turbidite, medium
28R-3, 106–108	251.26	0.9			Volcanic turbidite, fine
29R-2, 29–31	258.29	2.4			Volcanic turbidite, fine
30R-2, 102–104	268.42	0.6			Volcanic turbidite, medium
30R-2, 107–117	268.47	1.0			Volcanic turbidite, fine
31R-1, 50–52	272.50	2.1			Volcanic turbidite, fine
32R-1, 103–105	279.13	49.6			Volcanic turbidite, coarse
33R-1, 27–35	287.77	11.6			Volcanic turbidite, fine
33R-3, 74–76	291.24	18.4			Volcanic turbidite, coarse
33R-5, 12–14	293.62	4.2			Volcanic turbidite, coarse
33R-6, 60–70	295.60	8.2	l.d.	l.d.	Volcanic turbidite, coarse
34R-3, 15–17	300.15	5.9			Volcanic turbidite, medium
35R-3, 36–38	309.76	0.3			Volcanic turbidite, medium
36R-1, 63–65	316.53	6.6			Volcanic turbidite, coarse
36R-3, 76–78	319.66	5.3			Volcanic turbidite, fine
37R-2, 0–10	326.60	0.7	0.01	l.d.	Volcanic turbidite, fine
37R-2, 115–116	327.75	5.0	0.14	l.d.	Volcanic turbidite, coarse
38R-1, 112–114	335.62	2.1			Volcanic turbidite, fine
39R-2, 41–43	345.71	14.8			Volcanic turbidite, fine
40R-1, 39–41	353.49	2.4			Volcanic turbidite, medium
41R-1, 19–21	362.69	0.9			Volcanic turbidite, fine
41R-2, 0–10	364.00	1.2	0.08	0.03	Volcanic turbidite, fine
42R-1, 53–55	369.13	0.5			Volcanic turbidite, fine
43R-1, 106–108	375.76	0.6			Volcanic turbidite, coarse
44R-1, 123–126	384.93	0.7			Volcanic turbidite, medium
45R-1, 85–87	393.95	1.9			Volcanic turbidite, medium
46R-1, 78–80	403.28	0.2			Volcanic turbidite, fine
47R-1, 89–91	412.79	1.3			Volcanic turbidite, medium
48R-4, 21–23	426.11	1.2			Volcanic turbidite, medium
49R-1, 35–37	431.25	0.5			Volcanic turbidite, fine
49R-2, 140–150	433.80	0.2	0.07	0.03	Volcanic turbidite, fine
50R-1, 81–83	441.01	0.5			Volcanic turbidite, fine
51R-1, 71–73	450.31	0.2			Volcanic turbidite, fine
52R-2, 118–120	461.48	0.2			Volcanic turbidite, fine
53R-1, 128–130	466.18	0.1			Volcanic turbidite, medium
54R-2, 0–12	472.50	0.2			Clay radiolarite
54R-2, 57–59	473.07	0.2			Radiolarite
55R-2, 62–64	481.22	0.2			Clay radiolarite

Note: l.d. = less than detection level.

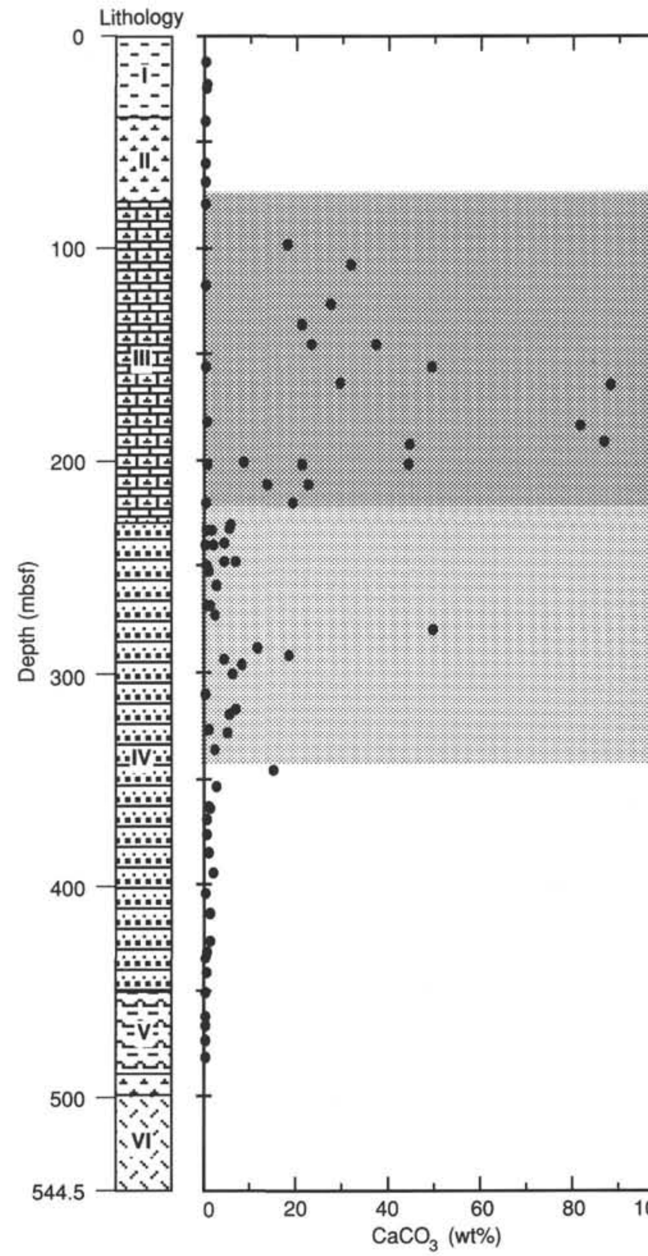

Figure 15. The calcium carbonate ($CaCO_3$) content of sediments from Hole 800A. Dark area represents lithologic Unit III (chert and limestone). Gray area corresponds to the middle and upper parts of lithologic Unit IV (volcaniclastic turbidites with basal calcareous beds).

geological and oceanic evolution of the Pigafetta Basin since Berriasian time. The main changes in oceanic conditions (e.g., primary productivity and preservation, deep-water masses and currents) recorded in the sediments result from the paleolatitudinal migration of the site and the subsidence of seafloor (see "Biostratigraphy" and "Paleomagnetics" sections, this chapter).

The Intrusive Event and Early Cretaceous Sedimentation (Berriasian-Barremian)

Above and within the intrusive dolerites between 498.1 and 449.6 mbsf, the sediments are siliceous and consist mainly of radiolarian claystones and radiolarites. Thermal diagenetic effects of the intruded sill on the sediments may have induced the formation of red chert with well-preserved laminations (Unit VI at 507.5 mbsf). Siliceous biogenic deposits, sometimes baked or metamorphosed by the setting of igneous rocks, are common. The epochs of siliceous sedimentation are also often contemporaneous with episodes of fast oceanic spreading, volcanism, and consequent global transgressions (Garrison, 1974; Jenkyns, 1978; Jenkyns and Winterer, 1982).

Lithologic Unit V (449.6–498.1 mbsf), which overlies the dolerites, consists of alternated red radiolarites and claystones beds showing an apparent cyclicity. Based on the low sedimentation rate of this facies (about 2 m/m.y.), the average rhythmicity is about 40 k.y., a period clearly compatible with Milankovitch-type cycles. The worldwide formation of pelagic alternations during the Early Cretaceous is generally attributed to global climatic pulses (Berger et al., 1984). In the northwestern Pacific such deposits were described by Ferry and Schaaf (1982). Even if such rhythmic deposits are mostly described in calcareous sediments (alternations of limestones, marls, and clays), siliceous deposits at Site 800 may have recorded fluctuations in productivity that resulted in rhythmic deposition of biogenic siliceous phases at depths below a contemporaneous CCD, within an oxidizing bottom environment. The slight influence of the underlying volcanics is expressed in the lower part of these deposits by the diagenetic remobilization of various components expressed as manganese oxide coatings and abundant thin, silica-filled fractures.

Aptian Volcanic Event

During terminal Barremian times, Site 800 experienced an intense volcaniclastic deposition event which seems to have abruptly interrupted and diluted the biosiliceous sedimentation. The volcaniclastic material was redeposited mostly as turbidite beds in a thick "sequence" of about 221 m (449.6 to 228.6 mbsf, Unit IV). Successive types of turbidites, differentiated by thickness, grain size, and composition, record the relative variations of intensities of volcaniclastic or/and pelagic inputs, and the environment conditions of the deep sea.

The lower volcaniclastic deposits are coarse-grained, form massive beds, and contain grain flows, breccia, and debrites (449.6–343.8 mbsf). The deposits are free of calcareous biogenic phases but the fracture fillings are often calcitic within the more volcanogenic layers. Thus, the biogenic contribution is mostly siliceous, in continuity with the previous deposits, and better represented in the finer clayey beds that also show upward-migrating oxidation fronts. Alteration and authigenetic processes within volcanogenic deposits form a green clay minerals matrix and fracture filling. This type of deposit reflects: (1) a high level of volcanic activity producing material which reacts intensively with seawater, (2) the proximal location of the site to the volcanic source, and (3) the oxidizing bottom conditions allowing preservation of biogenic phases and development of red top beds during quiet episodes between intermittent setting of volcaniclastic flows.

The overlying turbidites, from 343.8 to 278.1 mbsf, have mostly the same characteristics, with a slight decrease in thickness and grain size in some beds. The main change is in the calcareous input; carbonate phases are mainly shallow-water debris. This deposition interval could result from the degradation, under high energy conditions, of the top and shallow slopes of the nearby, still active seamounts. The intense erosion processes of such shallow-water volcanogenic and biogenic facies may occur during abrupt tectonic events of seamount subsidence (e.g., Jackson, Koizumi, et al., 1980, and references therein).

The uppermost interval of turbidites (top of Unit IV, 278.1–228.6 mbsf) corresponds to the final stage of the large volcaniclastic sedimentary event. The turbidite beds become thinner, finer-grained, and finer-laminated. The facies grades up to more siliceous and somewhat calcareous biogenic deposits. Carbonate content is low, reflecting limited pelagic input (nannofossils). The time span between the deposition of successive turbidite beds allows the development of well-oxidized horizons with abundant bioturbation features. Thus, migration of the site into an area of high primary productivity may have provided an adequate environment for the formation of clayey siliceous pelagic sediments mixed with the final stage of volcaniclastic redeposition.

The volcaniclastic and pelagic sequence with its characteristic high sedimentation rate provides a complete record of a middle Cretaceous volcanic event in a deep basin. This volcanic activity, which resulted in the edification of major volcanic plateaus and numerous seamounts in the northwestern Pacific, occurred throughout the Pacific Ocean (Larson and Schlanger, 1981; Moberly, Schlanger, et al., 1986).

Albian-Cenomanian Biogenic Sedimentation

After the volcanic event, sedimentation was dominated by the siliceous and calcareous biogenic contribution (lithologic Unit III, 228.6–78.2 mbsf). The sedimentary transition is gradational and the remobilization of volcanogenic phases is common in the lower levels of the gray radiolarian chert and limestone. The main trends in this lithologic unit are the progressively upward increase in calcareous biogenic input within the lowermost horizons (228.6–162.9 mbsf), followed by a gradational decrease in the calcium carbonate content (162.9–78.2 mbsf). The deposits seem to reflect the oceanic environment when the site reached subequatorial paleolatitudes, characterized by nutrient-rich surface water masses yielding high primary productivity, a weakly reducing deep-water environment, and a sufficiently high sedimentation rate, favoring preservation of biogenic phases. Diagenesis then silicified limestones and chertified radiolarian oozes, creating of a full range of various lithologies between chalks and cherts. The evolution of siliceous biogenic oozes and formation of cherts, and the role of various amounts of clays and carbonate, as well as the role of time in the mineralogical composition of cherts, have been discussed by Lancelot (1973), Wise and Weaver (1974), Kastner et al. (1977), and Pisciotto (1981) and references therein.

Siliceous Sedimentation During the Late Cretaceous

During Turonian to late Campanian times, sedimentation was predominantly siliceous, with a relatively low sedimentation rate. The diagenetic transformation of clayey siliceous oozes leads to the formation of iron-rich, red porcellanite and cherts (lithologic Unit II, 78.2–38.0 mbsf). The conditions of deposition show a slight change from the previous gray cherts with more oxidizing bottom conditions. Similar Upper Cretaceous red cherts are widespread in the northwestern Pacific Ocean (Thiede, Vallier, et al., 1981; Pisciotto, 1981).

Pelagic Brown Clay Deposition from the Latest Cretaceous to the Cenozoic and Quaternary

The uppermost deposits (0–38 mbsf, lithologic Unit I) are pelagic brown clay similar to that described in the recent deep ocean basins. A drastic change in sedimentation outlines the transition between cherts and clays in the late Campanian. The clay facies results from the nondeposition and/or dissolution of biogenic compounds at depths below the CCD. The CCD depth was about 3500 m during the early Tertiary and deepened near the end of the Eocene down to an average depth of about 4500 m (Hay, 1988). The average sedimentation rate of such deposits is very low and enhances early diagenetic processes expressed by authigenesis of clays, iron oxides, and zeolites. A possible hiatus separates the lowest and lighter-colored Campanian pelagic clay from the Cenozoic brown clay. Because biostratigraphy is not very precise in the condensed deposits, it is not possible to preclude the occurrence of successive hiatuses during the whole period. Long hiatuses, particularly during the Paleocene, across the Eocene-Oligocene boundary, and during Miocene, are widespread in the northern Pacific Ocean (Karpoff, 1989, and references therein).

BIOSTRATIGRAPHY

A sequence of sediments was recovered from 58 rotary-drilled cores dated as possibly Miocene-Pliocene to Berriasian-Valanginian, based on their microfossil content. A hiatus is suspected at the base of Core 129-800A-4R, from which core-catcher sediments were tentatively dated as middle Miocene to middle Pliocene. Core recovery was generally less than 30% although in some instances it was as high as 96%. Core-catcher samples were examined for radiolarians, foraminifers, palynomorphs, and calcareous nannofossils. Other samples from within the cores were examined when core catchers yielded few or no microfossils.

The cores were dated using three groups: calcareous nannofossils, radiolarians, and foraminifers. The calcareous nannofossils are most abundant and useful in the middle Cretaceous sediments. Radiolarians are the most persistent group but their stratigraphic utility at this site is limited to the Neocomian and Upper Cretaceous intervals. Although foraminifers occur sporadically through the cores, they corroborate ages determined by calcareous nannofossils and radiolarians. A summary of the biostratigraphy of Site 800 is presented in Figure 16.

Our interpretation of a general abyssal paleoenvironment, with deposition below the CCD, is attested by a high abundance of radiolarians throughout the cores, sparsity of calcareous nannofossils, virtual absence of planktonic foraminifers, and presence of agglutinated benthic foraminifers. Redeposited larger foraminifers signify proximity to shallow-marine (photic zone) paleoenvironments and transportation and reworking by turbidity currents. Palynomorphs were not observed in samples examined thus far, although amorphous organic matter was encountered in some intervals.

Preliminary data regarding the abundance of calcareous nannofossil and radiolarians are reported in Figure 17 against ages, lithostratigraphy, and paleolatitude. Radiolarians occur abundantly through the Mesozoic except for the Aptian to Barremian(?) interval corresponding to the southernmost location of this site with respect to the equator, as suggested by paleomagnetic data. Highest nannofossil abundance was observed in the Cenomanian to Albian interval, whereas during the Aptian nannofossils are sporadic and rare to few.

Calcareous Nannofossils

No age-diagnostic nannofossils were observed from Cores 129-800A-1R through -5R, except for a single specimen of *Reticulofenestra pseudoumbilica* in Sample 129-800A-4R-CC. If this is reliable, then Core 129-800A-4R is middle Miocene to middle Pliocene in age. We hesitate to place much confidence in an age determination from a single specimen from otherwise barren cores. No other Cenozoic age determinations were made at this site.

The first evidence of Cretaceous sediments was found in Sample 129-800A-6R-1, 3–4 cm. Two specimens of *Watznaueria barnesae* were encountered in this sample but accompanied by a badly overgrown discoaster. As discoasters are confined to the Cenozoic and *Watznaueria* is confined to the Mesozoic, the former must be considered contamination or the latter considered reworking. Other fossil groups indicate that this sample is Cretaceous in age, so we consider the discoaster contamination and, consequently, also consider this sample Cretaceous in age.

All subsequent samples examined are barren of nannofossils until Sample 129-800A-11R-1, 11–23 cm. This sample contains rare specimens of *Cruciellipsis chiastia, Lithastrinus floralis, Rucinolithus terebrodentarius, Prediscosphaera columnata, Eiffellithus turriseiffelii,* and several other less diagnostic species. We assign this sample to the *E. turriseiffelii* Zone of Thierstein (1973, 1976), Zone NC10 of Roth (1978), and Zone CC9 of Sissingh (1977), based on the presence of *E. turriseiffelii* and the absence of *Lithraphidites acutus, Microrhabdulus decoratus,* or any other younger nannofossil markers.

Nannofossils remain few to common in abundance and the assemblage is basically unchanged down to the middle of Core 129-800A-16R, where well-preserved, abundant nannofossils occur. A form closely resembling *Lithraphidites alatus* was observed in that core and consistently downhole until Sample 129-800A-19R-CC. While not mentioned in zonal schemes used here, *L. alatus* ranges from the top of Sissingh's Zone CC9 down to the middle of Zone CC8 on the generalized range chart of Perch-Nielsen (1985, p. 374). If this datum proves reliable, this sequence of cores should be no older than middle Albian. *Rucinolithus irregularis* was first observed in the above sequence from Sample 129-800A-16R-CC. Although the last occurrence of *R. irregularis* is not used as a datum in the zonal schemes adopted here, the species has the last occurrence during the late Albian according to Perch-Nielsen's (1985, p. 342) range chart. This allows us to place the Cenomanian/Albian boundary within Core 129-800A-16R.

E. turriseiffelii was observed down to Section 129-800A-21R-2, 3 cm, and we place the lower limit of the *E. turriseiffelii*/NC10/CC9 Zone within Section 129-800A-21R-2, which is slightly younger than the upper/middle Albian boundary.

The persistent occurrence of *P. columnata* down to Sample 129-800A-24R-1, 86–87 cm, allows determination of the boundary between the *P. columnata*/NC8-NC9/CC8 and *P. angustus*/NC7 zones. We use here *P. columnata* as emended by Manivit et al. (1977), referring to both the species and the zonal names. The *P. columnata*/*P. angustus* zonal boundary is placed within Core 129-800A-24R, below the sample mentioned above.

Tranolithus orionatus is not used in the adopted zonal schemes but its first occurrence is reported in the middle Albian by Perch-Nielsen (1979, 1985). On the basis of the distribution of this taxon, the middle/lower Albian boundary is assigned between Sample 129-800A-23R-1, 21–22 cm, and Sample 129-800A-23R-1, 77–78 cm.

Sediments between Samples 129-800A-24R-CC and -27R-1, 111 cm, contain common nannofossils which include *L. floralis* and *P. angustus,* but not *P. columnata*. We consequently assign these samples to the upper Aptian *P. angustus* Zone of Thierstein (1971, 1973, 1976) and Zone NC7 of Roth (1978).

The Albian/Aptian boundary cannot be determined on the basis of nannofossil events. This boundary is reported within the upper part of the *P. angustus* Zone (Thierstein, 1971, 1973, 1976) and Zone NC7 (Roth, 1978). In the drilled sequence it could coincide with the boundary between lithostratigraphic Unit III and Unit IV, at 228.6 mbsf (see "Lithostratigraphy" section, this chapter). Consequently, a hiatus should not be ruled out at this interval.

The lower boundary of the *P. angustus*/Zone NC7 coincides with the upper/lower Aptian boundary; therefore, we believe this boundary lies within Core 129-800A-27R.

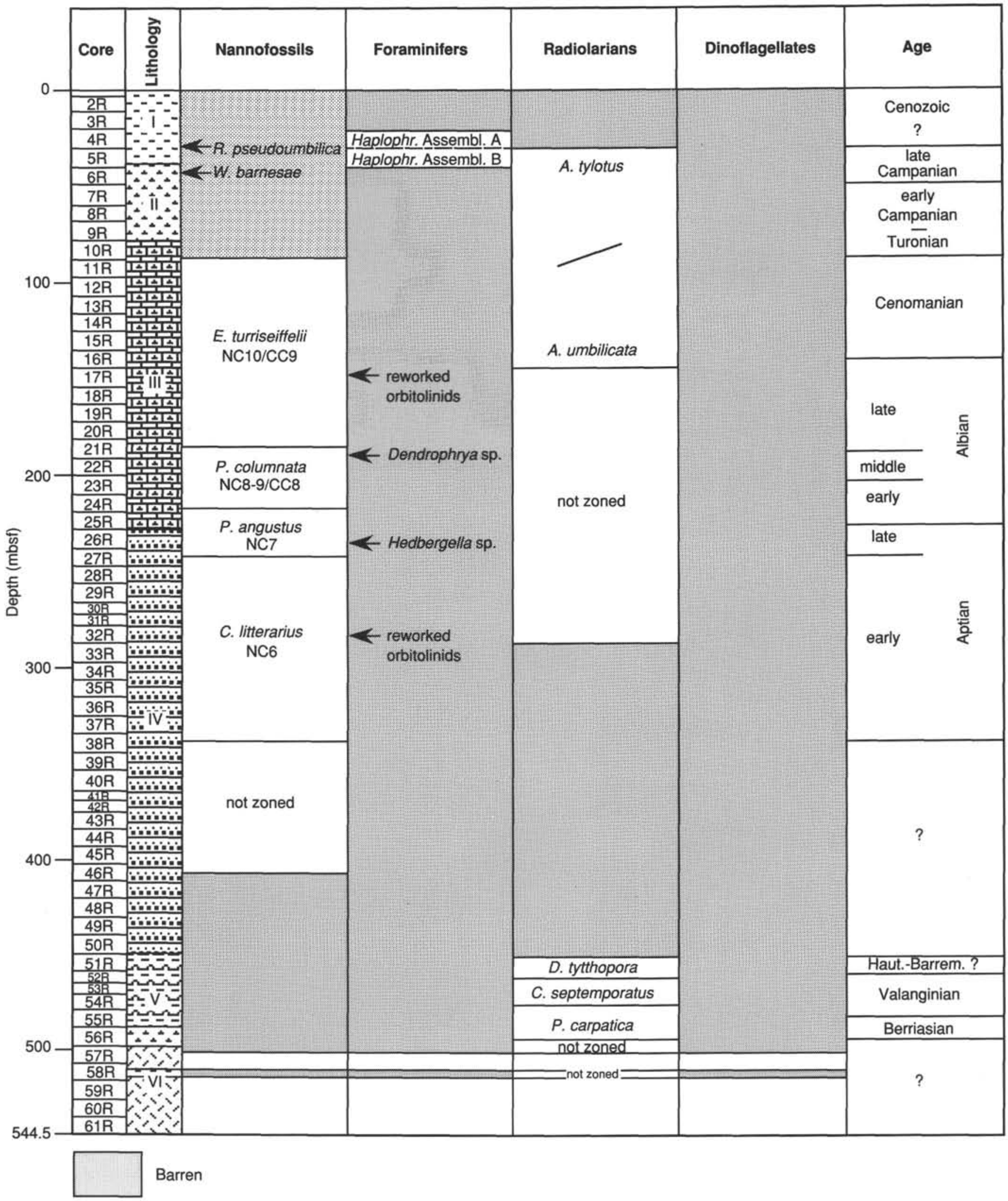

Figure 16. Summary of the biostratigraphy for Hole 800A.

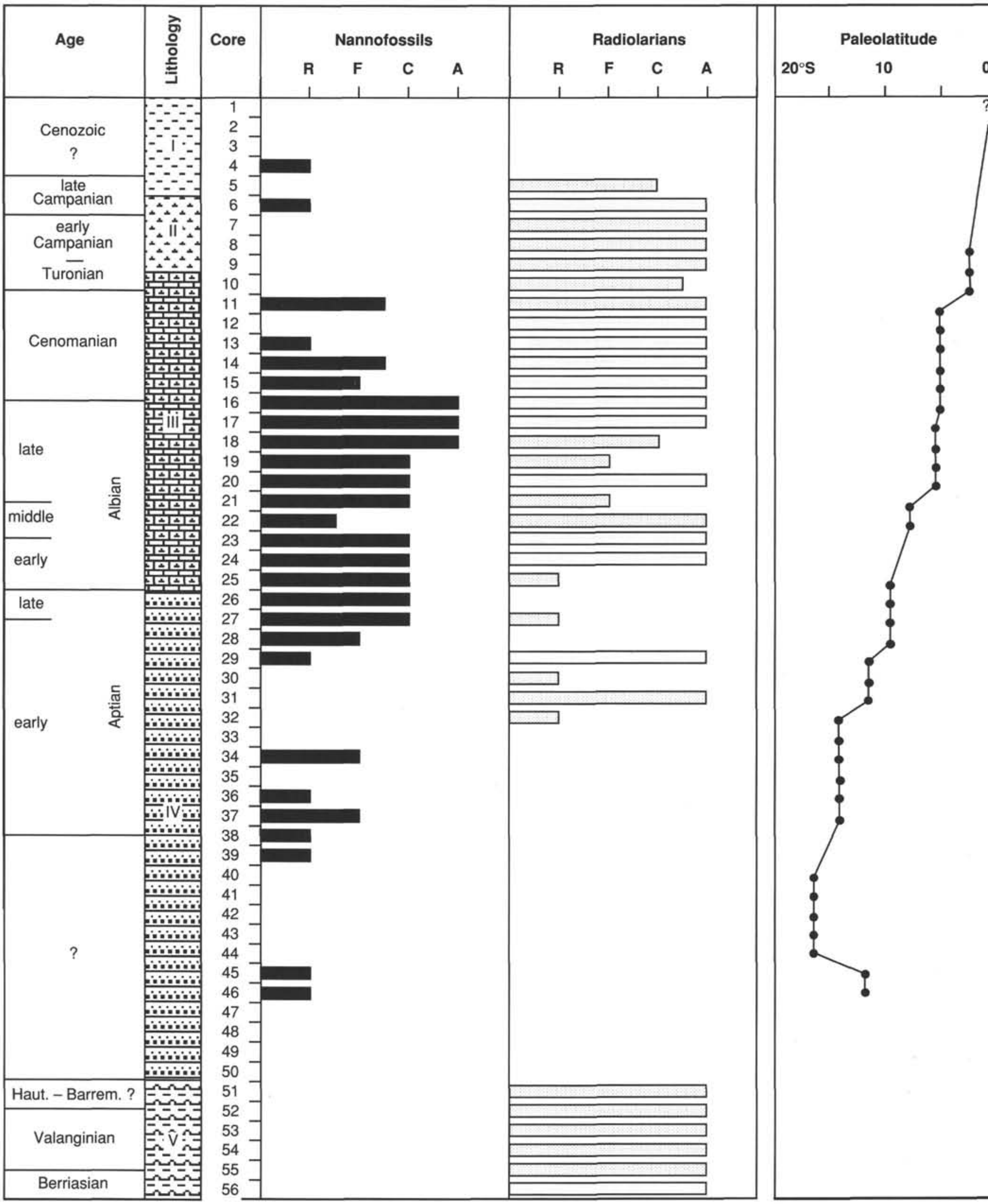

Figure 17. Abundance of calcareous nannofossils and radiolarians plotted against age, paleolatitude, and lithostratigraphy. Relative abundance is denoted as follows: rare (R), few (F), common (C), and abundant (A). (See "Explanatory Notes" chapter, this volume, for further discussion of abundance parameters.)

Sample 129-800A-26R-1, 103 cm, contains our first observance of *Assipetra infracretacea*. Although not mentioned in zonal definitions, Perch-Nielsen (1985) reports the range of this species as Valanginian to Aptian, which confirms our assignment of that sample within the Aptian.

The abundance of nannofossils for the subsequent cores fluctuates from barren to few, with preservation remaining poor. *R. irregularis* was observed as low as the bottom of Section 129-800A-38R-1, confirming that the age of that core is no older than the lower Aptian *C. litterarius* Zone of Thierstein (1971, 1973, 1976) and Zone NC6 of Roth (1978).

A range chart of important species used as markers in the Aptian-Cenomanian interval at this site is presented in Figure 18.

No more age-diagnostic nannofossils were encountered in the remainder of these cores, and the last nannofossil observed, *W. barnesae,* was in Sample 129-800A-46R-1, 91–92 cm.

Foraminifers

Only four of the 56 core-catcher samples recovered from Hole 800A contain foraminifers, which are present in moderate abundances and are sometimes well preserved. Additional samples were processed for foraminifers from the relevant cores.

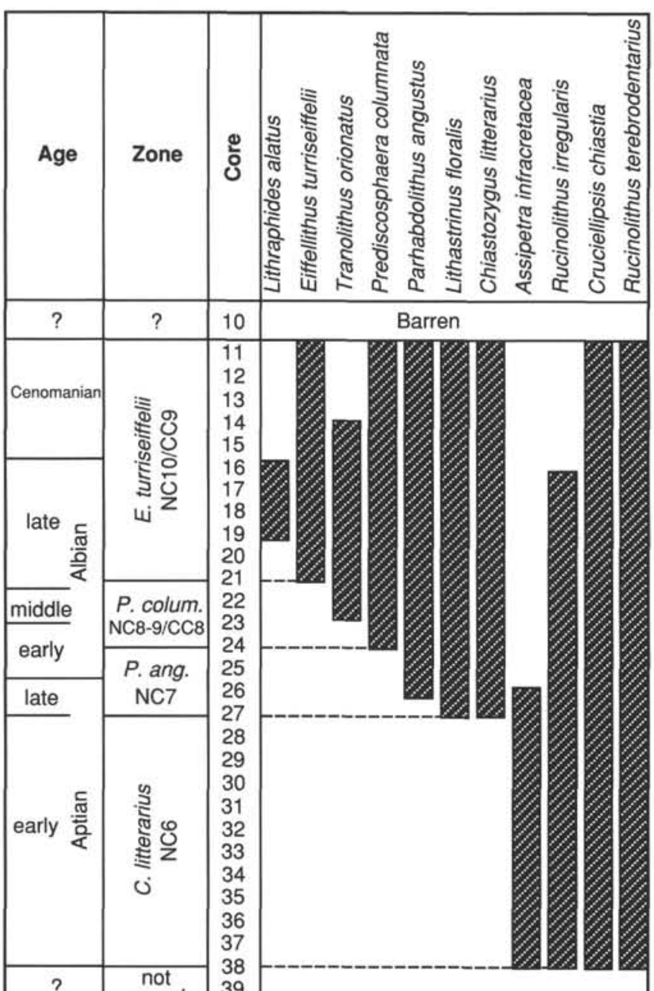

Figure 18. Distribution of important nannofossil species for Hole 800A during the Aptian-Cenomanian interval.

The core catcher from Core 129-800A-4R and four additional samples, 129-800A-4R-1, 72–74 cm; -4R-3, 30–32 cm; -4R-3, 96–98 cm; and -4R-4, 27–29 cm, contain low-diversity (benthic) agglutinated foraminifers that we informally refer to as *Haplophragmoides* Assemblage A. This assemblage is dominated by a possible new species of *Haplophragmoides,* as well as *Paratrochamminoides* sp., *Pseudobolivina munda,* and *Bolivinopsis parvissimus* in low abundances. The latter two species have previously been described from Deep Sea Drilling Project (DSDP) sites, where they are reported to be Late Cretaceous, Santonian to Campanian in age (e.g., Krasheninnikov, 1971). Depending on the reliability of the nannofossil evidence, the stratigraphic range of these species may be extended into the Cenozoic, middle Miocene to middle Pliocene.

Sample 129-800A-5R-CC contains a more diverse agglutinated foraminiferal assemblage that we refer to as *Haplophragmoides* Assemblage B. The majority of these species so far have been described only from the Pacific (DSDP Site 198). The species *Haplophragmoides multicamerata, H. fraudulentus, H. pervagalus, H. biumbilicata, H. perexplicatus, H. parvus, H. brevialus,* and *Praecystammina globigeriniformis* have previously been assigned a Late Cretaceous, Santonian to Campanian age (Krasheninnikov, 1971), and a similar age is attributed to this interval in Hole 800A. *Hormosina ovulum* is also present in this interval but is reported to be a long-ranging form, from Hauterivian (Lower Cretaceous) to Thanetian (Paleocene), according to Geroch and Nowak (1983). Presence of the radiolaria *Dictyomitra koslovae* in this sample indicates a late Campanian age. The very fine-grained and delicate nature of the agglutinated foraminiferal tests in these samples is characteristic of foraminifers from abyssal paleoenvironments.

The sedimentologic thin-section Sample 129-800A-17R-1, 44–46 cm, contains rare, reworked, smaller calcareous benthic foraminifers, but these are not identifiable. Reworked larger benthic foraminifers tentatively identified as *Orbitolina* sp., but lacking diagnostic internal specific characters, are also present in this thin section. Thin sections from Core 129-800A-18R also contain rare reworked benthic foraminifers.

The core-catcher samples from Cores 129-800A-6R to -20R are barren of foraminifers. Sample 129-800A-21R-CC contains abundant primitive tubular agglutinated foraminifers identified as *Dendrophrya* sp. and *Rhabdammina* sp. Both of these forms, however, are long-ranging and neither are age-diagnostic, but their presence has interesting paleoenvironmental implications. Recent studies in the Panama Basin (Kaminski et al., 1988a) have shown that *Dendrophrya* lives in an epifaunal habitat with the abundance of specimens falling sharply beneath the flocculent (nephloid) surface layer, the form being absent 5 cm below the surface. Schroeder (1986) has shown the presence of high concentrations of primitive tubular foraminifers in turbidite layers of the Nares Abyssal Plain. Kaminski et al. (1988b) report a redeposited *Dendrophrya* assemblage from turbidite clays of the lower Lizard Springs Formation of Trinidad. It is expected (Kaminski et al., 1988b) that concentrations of *Dendrophrya* would be seen in the "d" layer of the Bouma turbidite sequence, following erosion of flocculent surface sediments by turbidity currents and subsequent deposition of the entrained turbidite component. From the concentration of primitive tubular agglutinated foraminifers in Hole 800A, a similar mechanism is envisaged. The absence of multichambered or other foraminifers supports the argument of redeposition.

Samples 129-800A-22R-CC to 129-800A-25R-CC are barren of foraminifers. Minute planktonic foraminifers that may belong to the genus *Hedbergella* are seen in the 38- to 63-μm sieve fraction from Sample 129-800A-26R-1, 98–100 cm. These could not be positively identified due to small size and poor preservation. *Hedbergella* is the dominant Early Cretaceous planktonic foraminifer in the Barremian and Aptian, which would be in accordance with the Aptian age given for the calcareous nannofossils. The very small size of the form in Hole 800A may indicate that specimens are juveniles, although the possibility that it represents dwarfism in less than optimum conditions (high silica content of the seawater) cannot be excluded.

Rarity of planktonic foraminifers and their restriction to the fine (silt) fraction of the sediments together with the calcareous nannofossils points toward preferential preservation of the microplankton, perhaps through ingestion and redeposition via fish fecal pellets in an otherwise non-carbonate environment. Absence of benthic agglutinated foraminifers may be due to dilution through high sedimentation rates.

A sedimentologic thin section, Sample 129-800-32R-1, 117–118 cm, contains orbitolinid foraminifers, echinoderm, and algae fragments, which indicate redeposition from shallow-water environments. The sediments in this interval are dated by nannofossils as early Aptian.

Radiolarians

In addition to the 56 core-catcher samples, 19 additional samples from Cores 129-800A-50R to -58R were investigated. Cores 129-800A-1R to -4R are barren of radiolarians. No Cenozoic radiolarians were obtained from this site.

Samples 129-800A-5R-CC to -16R-CC yielded abundant but poorly preserved radiolarians. Only robust and morphologically characteristic species such as *Dictyomitra koslovae, Dictyomitra formosa* and *Pseudodictyomitra pseudomacrocephala* were identified at the species level. These assemblages indicate a late Albian to late Campanian age (upper *Acaeniotyle umbilicata* Zone to lower *Amphipyndax tylotus* Zone). It is difficult to draw any zonal boundaries in this interval because of the lack of zone diagnostic radiolarians. *D. koslovae* was observed in Samples 129-800A-5R-CC and -6R-CC, indicating late Campanian age.

In Samples 129-800A-17R-CC to -32R-CC, common to abundant but poorly preserved radiolarians are present. Cryptocephalic and cryptothoracic nassellarians are common. The poor preservation does not permit zonal assignment. Samples 129-800A-33R-CC to -50R-CC are barren of radiolarians.

Radiolarite and underlying chert samples of Cores 129-800A-51R to -57R contain abundant radiolarian tests. All samples except for Samples 129-800A-56R-CC; -57R-1, 3–7 cm; and -57R-1, 5–8 cm, yield poorly to moderately preserved radiolarians that permit zonal division of this interval. Radiolarians from the three lowermost samples are very poorly preserved because of contact metamorphism from the underlying dolerite sills. In this interval, *Pseudodictyomitra carpatica, Thanarla pulchra, Sphaerostylus lanceola,* and *Acanthocircus dicranacanthos* commonly occur. These species generally characterize Neocomian sediments. A single specimen of *Dibolachras tytthopora* was observed in Sample 129-800A-52R-1, 57–59 cm. Therefore, the lower limit of the *D. tytthopora* Zone should be situated below that sample. *Archaeodictyomitra lacrimula* appears in Sample 129-800A-52R-2, 49–51 cm, and was found in three samples above the first occurrence. *Cecropus septemporatus* first occurs in Sample 129-800A-54R-2, 50–52 cm, and last occurs in Sample 129-800A-52R-CC. The first occurrence of *C. septemporatus* defines the base of the *C. septemporatus* Zone. The order of the first occurrence of the above-mentioned three species is consistent with range charts presented by Schaaf (1984) and Sanfilippo and Riedel (1985). The interval from the Sample 129-800A-51R-1, 30–31 cm, to Sample 129-800A-56R-1, 5–7 cm, is biostratigraphically subdivided into three parts: *D. tytthopora* Zone, *C. septemporatus* Zone, and *Pseudodictyomitra carpatica* Zone in descending order. It is difficult to assign ages to these zones because ranges of key species are quite different among authors. However, the first occurrence of *C. septemporatus* is regarded as being within the Valanginian by several authors (e.g., Schaaf, 1984; Sanfilippo and Riedel, 1985; Baumgartner, 1984, 1987). Radiolarians restricted to pre-Cretaceous ages are absent in this interval.

Sample 129-800A-58R-1, 45–48 cm, is chert that is intercalated within the dolerite sills. It contains common radiolarian tests but because of its extremely poor preservation, it is not assigned an age.

Palynomorphs

Cores 129-800A-1R through -57R are barren of palynomorphs. Samples 129-800A-7R-CC to 129-800A-9R-CC contain abundant amorphous organic matter, but no determinable palynomorphs.

Sedimentation Rates

Figure 19 shows the sedimentation rates for Site 800, as determined on the basis of nannofossil and radiolarian biostratigraphy.

PALEOMAGNETICS

Methods

All measurements were made with the whole-core cryogenic magnetometer. Cores 129-800A-1R through -5R were completely homogenized by the rotary coring process and thus were not measured. Beginning with Core 129-800A-6R, discrete core fragments, most often pieces of chert, were selected from the recovered core and placed in the sample holder with a 10-cm space between pieces; the pieces were taped into position with bedding planes oriented as nearly perpendicular to the magnetometer "z" axis as possible. Selection of samples was based primarily on large size and visibility of bedding traces. Measurements were then made utilizing a 1-cm sampling interval and a radius that approximated the average radius of the group of fragments within each measurement group. This method of measurement was used through Core 129-800A-22R and allowed magnetic measurements to be obtained in a sedimentary interval where recovery was low and represented by only fragments of chert and porcellanite.

Measurements of continuous cores were begun at Section 129-800A-23R-1 and continued through Core 129-800A-60R. Measurement intervals were chosen on the basis of (1) recovery, (2) lithology, and (3) the expected reversal frequency. Thus, a sampling interval of 2 cm was chosen in areas of low recovery, 3 cm for cores with continuous recovery, 5 cm for the high sedimentation rate sequence of the volcaniclastics, and 2 cm for Cores 129-800A-51R through -55R because of the high reversal frequency of the Berriasian-Barremian time interval.

Alternating field (AF) demagnetization of whole cores was varied in the number of steps and peak-field intensity, based on lithology and expected reversal frequency. Maximum AF demagnetization levels averaged approximately 10 mT but ranged from 8 to 20 mT. Lower fields were used for gray and white sediments in which the magnetic carrier seemed to be magnetite or a similarly low coercivity mineral. Demagnetization to 20 mT was used for the red-colored Berriasian-Barremian radiolarite and clay (Cores 129-800A-51R through

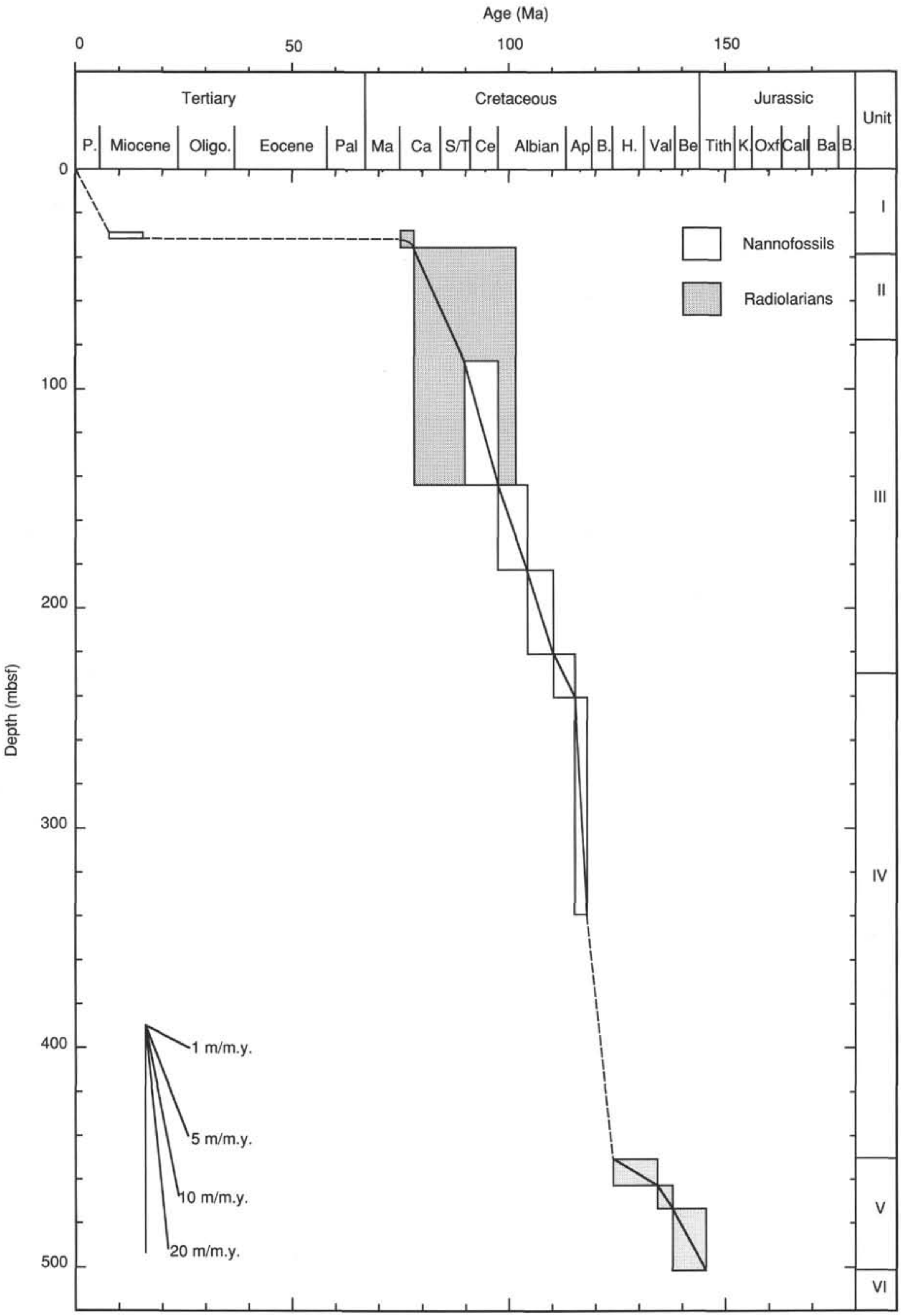

Figure 19. Sedimentation rates for Site 800.

-56R) and for reddish segments of volcaniclastic turbidites, both of which appeared from the red color and demagnetization responses to have higher coercivity remanence components.

Magnetostratigraphy

Definitive magnetostratigraphy at Site 800 was hampered by a combination low recovery rate for much of the hole, particularly in the Upper Cretaceous section, and the paucity of paleontological fauna at critical stratigraphic horizons such as the Maestrichtian/Campanian/Santonian boundaries and Aptian/Barremian/Hauterivian boundaries (see "Biostratigraphy" section, this chapter). Moreover, much of the recovery was occupied by an Aptian (hence normal polarity) volcaniclastic turbidite sequence; therefore, a large segment of the recovered record is a record of geologic events of probable short duration.

Site 800 is located at modern low latitudes, and was located at low paleolatitudes during the deposition of its sedimentary section. As a result, determination of polarity from unoriented drill cores can be difficult, because at low latitudes secular variation is high and thereby undermines the use of inclination data alone. Another difficulty in polarity determination is always the possibility of inversion of core fragments during preparation. Polarity was determined by large relative changes in declination during demagnetization (exceeding approximately 45°) combined with changes in the sign of inclination. In determining a polarity change, more consideration was given to large changes in declination than to inclination sign changes, because secular variation can readily change the sign of low-latitude inclinations but large shifts in declination during demagnetization are most likely due to the removal of the normal present-field component from a reversed characteristic magnetization. It should be remembered, however, that lack of change in declination (in an interval of significant inclination change) may be due to the presence of an unremoved overprint. This is of special concern in the lower part of this section where the red color and high coercivities suggest that hematite or iron hydroxides are a significant magnetic remanence carrier.

The youngest observed reversed interval occurs in Section 129-800A-7R-1 and is based on a single chert sample. The identification of the radiolarian *Dictyomitra koslovae* in Cores 129-800A-5R through -6R suggests that Section 129-800A-7R-1 may be as young as upper Campanian. However, the presence of reversed polarity in this core suggests that it was deposited during geomagnetic polarity interval 33R, therefore indicating an early Campanian age. Normal polarity was obtained in the lower part of this core and in many subsequent cores, suggesting a record of interval 34, the Cretaceous long normal interval, and therefore implying that the lowest part of the core is earliest Campanian to Santonian age.

No polarity changes were observed in the fragments measured from Cores 129-800A-8R through -22R, nor in the continuous core measurements of Cores 129-800A-23R through -50R. Their ages place them within the long normal polarity interval of the Cretaceous (see Fig. 5). Lithology changes markedly at Core 129-800A-51R, from volcaniclastics to finely laminated clays and radiolarites (Fig. 5), and remains that lithology to the end of the sedimentary section (through Core 129-800A-55R). Cores 129-800A-51R through -55R have been determined by radiolarian zonation to range in age from Barremian-Hauterivian(?) to Berriasian (see "Biostratigraphy" section, this chapter). Reversals were observed frequently in this part of the section, beginning in Core 129-800A-52, and continuing through Core 129-800A-55R. Reversals were not observed in Core 129-800A-51R, although this may be an artifact of its lithology; it has a large percentage of orange-colored radiolarite as compared to succeeding cores which are alternating orange and brown color. The orange color was observed to be correlated with higher coercivities; hence, it is possible that instead of being normal polarity, Core 129-800A-51R sediments simply may not be effectively demagnetized by the limited AF treatment. Shore-based thermal demagnetization will test this possibility. Even though reversals are observed throughout Cores 129-800A-52R through -55R, incomplete recovery and lack of more complete biostratigraphic zonation preclude polarity chron identification. Figure 20 shows the polarity reversals observed for the lower part of Hole 800, along with the biostratigraphic age assignments.

Paleolatitude

An important goal of Leg 129 is to decipher the motion of the Pacific plate for the Late Jurassic through the Late Cretaceous. The preliminary data from Site 800 can be used to estimate paleolatitude and, although limited in scope because of the limited demagnetization, offer some insight as to the amount of plate motion that has occurred. The problems encountered in determining polarity applied to the estimation of paleolatitudes as well. In addition, the AF demagnetization treatment of Site 800 sediments did not allow determination of stable endpoints because of the limited field strengths of the whole-core magnetometer assembly. Also, it was clear that

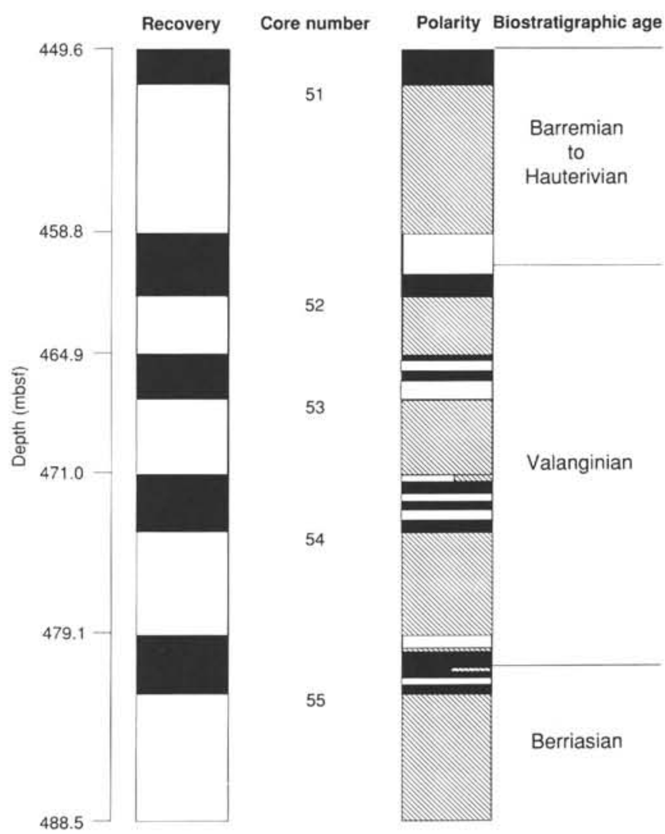

Figure 20. Summary of magnetic polarity for the Lower Cretaceous strata of Cores 129-800A-51R through -55R. Left-hand bar chart indicates interval recovery (black). Black and white bars in polarity column indicate normal and reversed polarities, respectively. Half bars represent a single sample or one with questionable polarity. Ages are from radiolarian zonation (see "Biostratigraphy" section, this chapter).

Table 3. Inclinations and mean paleolatitudes for selected intervals as described in the text.

Core, section, interval (cm)	Mean inclination (°)	No. of samples	Latitude	α_{95}	α_{63}
129-800A-					
8R-1, 0–5	−6.0				
8R-1, 27–32	−2.3				
8R-1, 35–40	−3.8				
8R-1, 40–45	−1.4				
8R-1, 47–50	−1.8				
8R-1, 60–63	−4.8				
8R-1, 70–77	−4.0				
8R-CC, 7–13	−3.5				
8R-CC, 15–21	−2.1				
8R-CC, 28–31	−10.6				
9R-1, 8–13	−3.1				
9R-1, 13–19	−8.2				
9R-1, 24–29	−1.0				
9R-1, 34–42	−12.9				
10R-1, 30–36	−4.6				
10R-1, 56–63	−9.8				
		16	−2.5	1.68	0.98
11R-1, 11–23	−4.9				
11R-1, 28–35	−6.1				
11R-1, 49–55	−13.5				
13R-1, 29–32	−16.4				
13R-1, 35–41	−11.6				
13R-1, 51–57	−8.2				
14R-1, 51–55	−15.3				
14R-1, 107–112	−8.3				
15R-1, 11–14	−3.7				
16R-1, 47–52	−12.2				
		10	−5.1	2.88	1.67
17R-1, 44–54	−7.4				
17R-1, 68–72	−16.4				
17R-1, 80–83	−1.9				
18R-1, 1–6	−10.6				
18R-1, 30–36	−11.1				
18R-1, 76–84	−10.9				
18R-1, 124–132	−13.5				
19R-1, 1–6	−6.8				
19R-1, 36–43	−9.3				
19R-1, 68–80	−18.2				
20R-1, 29–39	−12.3				
		11	−5.5	2.77	1.61
21R-1, 72–78	−20.6				
21R-1, 87–99	−17.2				
21R-1, 144–150	−14.4				
21R-2, 0–6	−15.1				
22R-1, 47–52	−12.8				
22R-1, 52–58	−16.4				
22R-1, 58–64	−9.9				
		7	−7.8	3.02	1.75
24R-1, 117–126	−5.1				
25R-1, 41–47	−11.8				
26R-2, 20–30	−14.3				
26R-2, 57–77	−8.9				
26R-3, 49–68	−20.0				
27R-1, 95–107	−23.5				
28R-1, 45–75	−33.2				
28R-2, 15–25	−15.7				
28R-3, 0–13	−22.4				
28R-4, 15–30	−24.5				
28R-4, 70–90	−22.0				
		11	−9.5	5.22	3.03
29R-1, 0–20	−18.0				
29R-1, 95–130	−25.5				
29R-2, 77–100	−21.0				
29R-3, 19–37	−16.0				
31R-2, 22–50	−26.5				
31R-2, 80–115	−24.2				
		6	−11.4	4.69	2.72
32R-2, 0–20	−24.4				
33R-1, 10–25	−20.0				
33R-1, 25–150	−33.5				
33R-2, 15–85	−31.4				
33R-2, 95–140	−28.8				
33R-3, 0–30	−24.0				
33R-3, 30–50	−22.0				
33R-3, 130–150	−27.0				
33R-4, 15–62	−32.8				
33R-4, 105–140	−25.4				
33R-5, 15–45	−23.8				
33R-5, 105–145	−29.5				
33R-7, 35–75	−29.7				
34R-1, 95–125	−29.2				
34R-2, 80–130	−25.9				
34R-3, 135–150	−25.9				
34R-4, 0–40	−25.9				
34R-4, 50–67	−25.7				
34R-4, 70–100	−27.1				
34R-4, 105–150	−25.9				
34R-5, 30–75	−21.6				
		21	−14.1	1.67	0.97
35R-1, 0–150	−22.6				
35R-2, 0–80	−25.2				
35R-2, 90–150	−29.5				
35R-3, 0–20	−26.3				
35R-3, 20–40	−27.8				
36R-2, 80–110	−31.3				
36R-3, 30–70	−25.5				
36R-4, 70–120	−22.2				
36R-5, 30–50	−22.7				
36R-5, 80–100	−28.1				
37R-1, 45–115	−29.3				
		11	−14.0	2.15	1.25
40R-1, 30–45	−28.7				
40R-1, 85–100	−36.7				
40R-1, 105–125	−37.9				
44R-2, 0–25	−16.2				
		4	−16.3	24.79	14.38
45R-1, 55–145	−21.4				
45R-2, 0–150	−21.4				
45R-3, 0–140	−21.5				
46R-2, 80–130	−24.7				
48R-1, 60–110	−26.9				
48R-6, 0–20	−18.4				
		6	−11.7	3.28	1.90

sediments with red coloration, particularly in Cores 129-800A-51R through -55R, contained high-coercivity minerals and were not completely demagnetized with the AF technique.

Paleolatitude data were obtained from all core fragments exhibiting magnetic stability (Cores 129-800A-8R through -23R) and from all portions within the continuous recovery in which pieces were at least 15 cm long. An additional constraint was to use only those portions of the continuous recovery that contained an interval of at least 10 cm over which declination was uniform at the maximum AF demagnetization step, a characteristic used to assure homogeneity of the magnetic signature. This latter restriction eliminated much of the information from the lower part of the hole.

All magnetic measurements within each acceptable core segment were averaged, excluding 3–5 cm at each end of the interval. These averages were grouped loosely by a combination of age and data quantity. The true mean inclinations, variances, and corresponding paleolatitudes of each group were computed using the method of Kono (1980), a method developed specifically for analysis of azimuthally unoriented cores. The results of this analysis are summarized in Table 3, and are plotted against age in Figure 21. It should be noted that relatively steep (15°) bedding plane dips were observed in the Aptian volcaniclastic turbidites (Cores 129-800A-26R through -50R). Furthermore, Hole 800A also deviates from vertical by up to 3°. Neither of these factors has been removed from these preliminary shipboard paleolatitude results.

The data from Site 800 indicate northward drift from at least Core 129-800A-44R onward, and suggest that a change

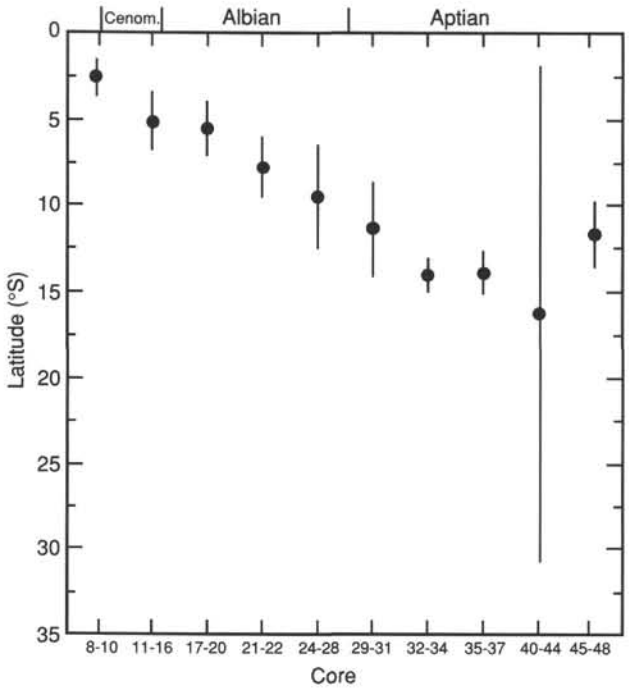

Figure 21. Mean paleolatitudes for core groups (as described in the text). Error bars represent standard deviation values (α_{63}; see Table 3).

from southward drift to northward drift occurs between the Hauterivian-Barremian and the early Aptian. This inference is remarkably consistent with the results of a study of Leg 32 basalts, in which Larson and Lowrie (1975) also postulated that a change in direction from southward to northward drift of the Pacific plate occurred during the Early Cretaceous. While the inflection point in the paleolatitudes (Fig. 21) is indicated by only a single point, preliminary work with Cores 129-800A-50R through -55R suggests a continuation of this trend.

Dolerite Magnetization

Cores 129-800A-57R through -60R were demagnetized with alternating fields of 4, 8, and 12 mT; core sections showing high coercivity of magnetization were demagnetized at 16 mT. The inclination values of the sills in the following discussion are subject to some uncertainty, as the horizontal reference is unknown, and the immediately overlying sediments display dips of up to 33°. The dolerite recovery was divided into three sill units on the basis of grain size and texture (see "Igneous Petrology" section, this chapter). The top of the upper sill (sill 1) is orange in color, suggesting significant oxidation. Sill 1 changes to a gray color in its lowest part (the lower part of Section 129-800A-57R-2). In addition to this oxidation, petrographic studies identified an additional, pervasive, low-grade metamorphism in the gray portions of sills 1, 2, and 3, which varied from a generation of large amounts of secondary clays to a greater alteration which generated lower greenschist facies minerals (see "Igneous Petrology" section, this chapter).

The intensity of natural remanent magnetization (NRM) was comparatively low for igneous material, averaging about 5 by 10^1 mA/m in the least altered dolerite, 1 by 10^2 mA/m in the most metamorphosed material (greenschist facies), and 2 by 10^1 mA/m in the most oxidized top portion of sill 1. NRM inclinations varied from 20° to +60°. Because the three different levels of alteration in these rocks are reflected in the

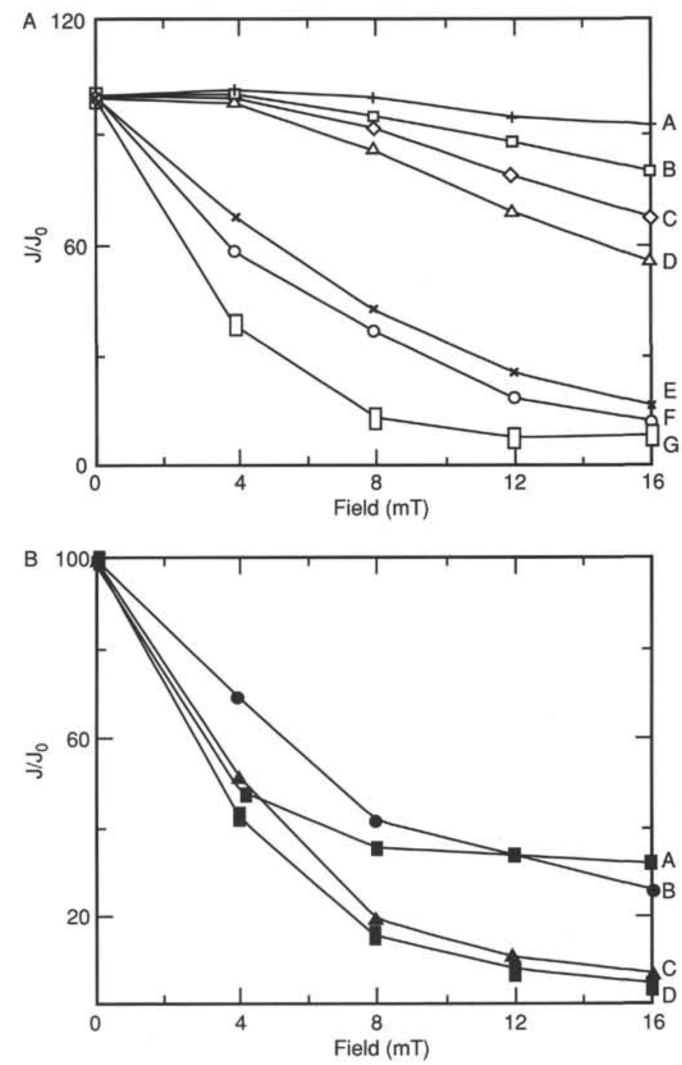

Figure 22. **A.** Alternating field demagnetization of various levels within sill 1, which illustrates the effect of the oxidation on the remanence. Curves A through E represent decreasing shades of orange, whereas curves F and G are gray. Depths within Section 129-800A-57R-2 are 25 cm (A), 5 cm (B), 55 cm (C), 65 cm (D), 80 cm (E), 120 cm (F), and 140 cm (G). **B.** Alternating field demagnetization of typical gray dolerite within sills 2 and 3. Curves A and B are typical of the least altered of the gray dolerite; curves C and D illustrate behavior of the dolerite that contains greenschist facies minerals.

magnetic behavior, the magnetic characteristics will be discussed according to alteration state.

The most prominent result of magnetic measurements in the dolerites is that the orange oxidized material at the top of sill 1 is clearly different from the underlying gray dolerites, both in polarity and response to AF demagnetization. Figure 22A shows demagnetization responses within sill 1; the distinctly orange dolerite displays behaviors depicted by curves A though E, while F and G represent the gray portion of sill 1. Median destructive fields (MDF) of much greater than 16 mT characterize the orange dolerite of sill 1 whereas MDF's of 3–6 mT characterize the gray dolerite of all three sills (e.g., curves F and G in Fig. 22A and all curves in Fig. 22B).

The inclination of the orange dolerite is negative, indicating normal polarity in the Southern Hemisphere, whereas inclinations in the gray dolerite vary from shallow to steeply positive values, indicating reversed polarity. The most heavily orange-colored dolerite has the steepest negative inclinations, approximately 21° after demagnetization to 16 mT. The inclinations decrease downcore uniformly and change to shallow, then steeper, positive values; the change coincides with the gradational change from orange to gray color (Fig. 23).

The least altered dolerite, found in Core 129-800A-60R (lower part of sill 3), has positive inclinations (after demagnetization to 16 mT) of about +42°. However, these are not yet trending to the origin on orthogonal axes plots. If the observed trends are continued, inclinations of about +30° might be inferred. Sill 2, although represented by only 27 cm of recovery, also displays steeply positive inclinations, approximately +50° after demagnetization to 12 mT. Inclinations within the upper part of sill 3 vary from shallow negative to shallow positive, with demagnetization responses reminiscent of the behavior of the oxidized top of sill 1. The polarity of this top part of sill 3 (Sections 129-800A-58R-1 and -58R-2) is generally normal with two intervals of reversed polarity (positive inclinations) interspersed.

Two slightly different AF demagnetization behaviors were noted in the gray dolerite of sills 1, 2, and 3. These differences appear to correspond to the alteration differences between the extensive clay production and appearance of lower greenschist facies minerals. Those areas identified as lower greenschist facies, e.g., Sections 129-800A-58R-1 and -58R-2, have lesser MDF's (curves C and D of Fig. 22B) than the least altered material (curves A and B of Fig. 22B). The lower greenschist grade regions also have normal polarity in contrast to the reversed polarity of the least altered dolerite, suggesting that if the reversed polarity is primary, this alteration also occurred at a later time than intrusion.

In summary, the sills appear to have been emplaced in a time of reversed polarity and were later altered in a time or times of normal polarity. The sills were intruded just below Berriasian sediments (see "Biostratigraphy" section, this chapter) and there is no indication that their reversed polarity magnetization is not a primary magnetization. Because the very thick volcanogenic turbidite sediments uphole are Aptian in age, and because one might expect that the intrusive emplacement was related to the extrusive activity giving rise to the volcaniclastic sediments of the turbidites, the age of the sill emplacement is likely to have been in a reversed interval closely preceding or succeeding Aptian time. This would suggest intrusion during M0 to M3 time (earliest Aptian-Barremian-late Hauterivian), or during anomaly 33R time (early Campanian). The proximity in age of the reversed interval in earliest Aptian time (M0) to the Aptian age of volcaniclastic sediment pile favors this Early Cretaceous age as the time of intrusion.

INORGANIC GEOCHEMISTRY

Eight interstitial water samples were squeezed from sediment cores recovered in Hole 800A. The first sample belongs to lithologic Unit I (brown clay); the others were collected in lithologic Unit IV (volcaniclastic turbidites) and Unit V (brown claystone). Unfortunately, it was impossible to sample water from chert and silicified limestone of the lithologic Unit III, because of both the lithology and the scarce recovery. Chemical analyses are summarized in Table 4 and presented in Figures 24 and 25. Except for the first sample, 10 to 20 cm^3 of water were extracted from 10-cm-long, whole-round core samples. No evidence of pollution by drilling fluids (seawater or mud, Table 4) was found from a combination of analytical results.

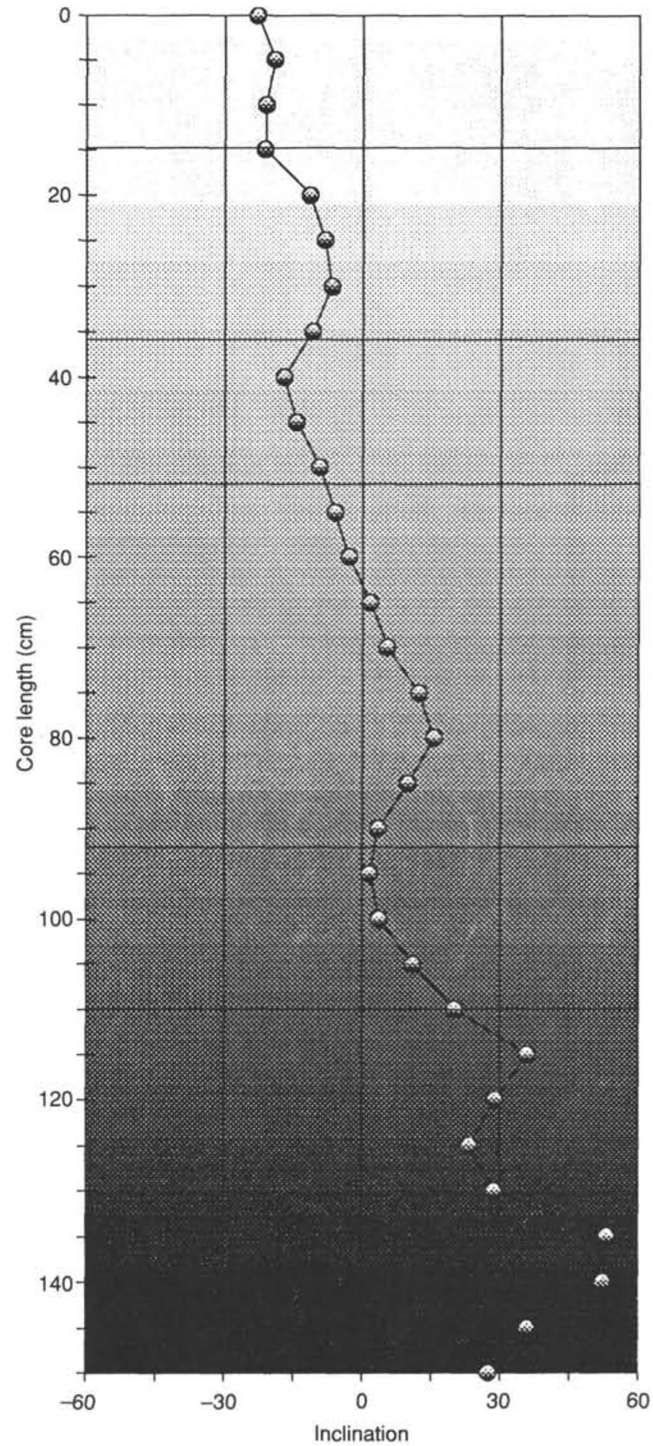

Figure 23. Inclination variations within sill 1, illustrating the correlation between orange color and inclination change. The sill in Section 129-800A-57R-2 is orange down to 110 cm, becoming gradually lighter from top to bottom; below 110 cm only gray dolerite is present. This color gradation is schematically illustrated by the background shading in the diagram. The lines indicate the positions of distinct oxidation fronts within the orange dolerite.

Table 4. Chemical composition of interstitial water extracted from sediments in Hole 800A, surface seawater, and water extracted from drilling mud.

Core, section, interval (cm)	Depth (mbsf)[a]	Alkalinity (meq/L)	Cl (mmol/L)	SO_4 (mmol/L)	pH	Salinity (‰)	Ca (mmol/L)	Mg (mmol/L)	K (mmol/L)	Na* (mmol/L)	Mn (μmol/L)
129-800A-											
4R-2, 25–30	22	2.3	568.9	25.8	7.5	36.2	10.5	53.1	11.8	480	1.8
26R-2, 140–148	232	0.5	537.2	17.6	8.2	33.8	56.0	9.2	2.8	436	86.7
27R-1, 140–150	239	0.5	527.3	14.5	8.1	33.0	58.3	8.2	1.8	417	57.8
33R-6, 60–70	296	0.6	530.3	14.0	7.8	33.5	58.2	6.7	1.4	426	33.1
37R-2, 0–10	327	1.2	554.1	16.4	8.1	35.0	54.7	13.7	1.9	444	49.2
41R-2, 0–10	364	0.6	531.3	11.1	7.1	32.2	57.3	8.0	1.6	420	38.1
49R-2, 140–150	434	0.7	531.3	12.3	7.1	33.0	59.2	10.6	1.3	411	18.3
54R-2, 0–12	473	0.6	554.1	13.2	8.2	33.7	60.8	11.7	2.0	429	6.3
Surface seawater		2.2	562.0	28.1	8.0	35.0	10.4	53.5	11.2	480	l.d.
Water from drilling mud		0.6	256.8	14.4	8.4	15.8	8.7	7.4	4.3	249	<3.0

Note: Na* is calculated by charge balance; n.d. = not determined; l.d. = less than detection level.
[a] Sub-bottom depth rounded to nearest meter.

Results

Concentrations of all major constituents except calcium show roughly the same depth profiles with different amplitudes (Figs. 24 and 25). For sodium, magnesium, potassium, chlorine, sulfate, and alkalinity, concentrations at 22 mbsf are close to seawater concentrations. Between 232 and 473 mbsf (in lithologic Unit IV), the concentrations of these species are reduced. The extent of the depletion depends on the chemical species. Potassium, magnesium, and alkalinity are reduced to 10%–30% of their values in seawater, sulfate to 40%–50%, sodium to about 85%, and chlorine to 94%. One sample at 327 mbsf appears systematically less depleted than the others; qualitatively, it contains fewer clay minerals than the other samples from this lithology. Finally, at 472 mbsf (in lithologic Unit V), the concentrations of these species increase to varying extents. These general trends are reflected by the depth profile of salinity, which decreases from a seawater value (36·) at 22 mbsf to 32.2·–33.8· between 232 and 473 mbsf, with the exception of the sample at 327 mbsf. The behavior of calcium is the opposite of the other major constituents. Below 232 mbsf, calcium concentration increases to about 560% to its value in seawater.

Strontium and silicon are enriched with respect to seawater at 22 mbsf and reach 321 and 546 μmol/L, respectively, at 240 mbsf. Strontium moderately increases to 356 μmol/L at 473 mbsf. In contrast, silicon concentrations decrease sharply between 240 and 296 mbsf to 200 μmol/L. Manganese concentrations are similar to seawater at 22 mbsf, then increase to 86 μmol/L at 232 mbsf, and decrease gradually to 6 μmol/L at 473 mbsf.

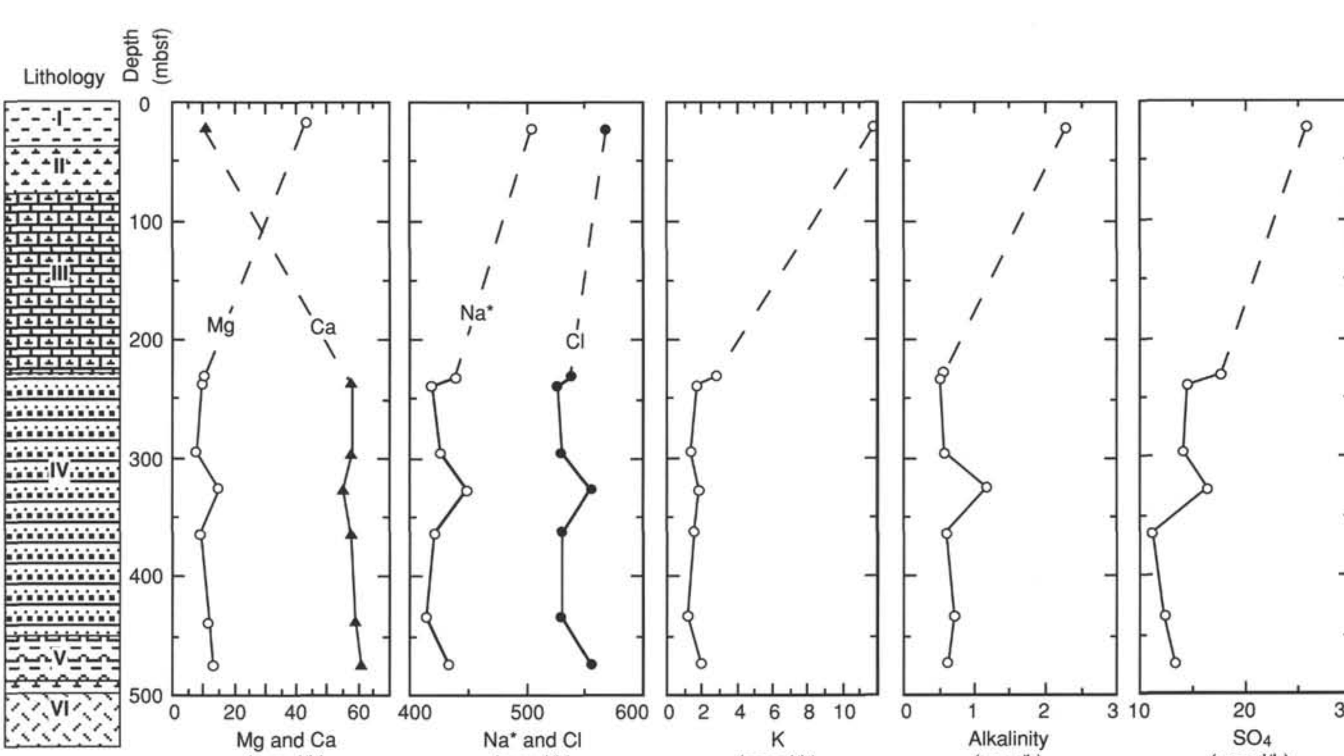

Figure 24. Concentration vs. depth profiles for Mg, Ca, Na*, Cl, K, alkalinity, and SO_4 in interstitial water extracted from sediments in Hole 800A. The lithostratigraphic column refers to the lithologic units defined in the "Lithostratigraphy and Sedimentology" section (this chapter). Unit I = brown clay, Unit II = red chert and porcelanite, Unit III = silicified limestone and chert, Unit IV = volcaniclastic turbidites, Unit V = brown claystone, and Unit VI = aphyric basalt.

Table 4 (continued).

Si (μmol/L)	Sr (μmol/L)	Lithology
377	89	Pelagic brown clay
n.d.	321	Volcanic turbidite
546	321	Volcanic turbidite
206	274	Volcanic claystone
193	n.d.	Volcanic turbidite
185	362	Volcanic sandstone
158	345	Volcanic siltstone
231	356	Radiolarian claystone
11	49	
17	—	

Concentration Gradients

The shapes of the concentration gradients of the major ions (Fig. 24) are characterized by a break below the cherts of lithologic Unit III and then by nearly constant concentrations in the underlying volcaniclastic turbidites. The break is certainly due to the presence of the chert, which acts as a very efficient barrier to diffusional communication. This is a consequence of the low porosity (10% to 30%) and low water content (5% to 15%) of the cherts (see "Physical Properties" section, this chapter). A similar effect of a lithological barrier was described previously and attributed to the occurrence of cherts over volcaniclastic units (e.g., DSDP Sites 315 and 317: Gieskes, 1976; DSDP Site 462: Gieskes and Johnson, 1981). The question is whether the chlorine, magnesium, sodium, potassium, and calcium concentration changes occur in lithologic Unit III or in the underlying sediments. In the absence of fluid samples from lithologic Unit III or above, it is difficult to give direct arguments. However, the reactions most probably occur in the volcaniclastic turbidites because the observed chemical variations are typical of the alteration of volcanic material. Similar conclusions were reached at DSDP Sites 317 and 462 based on diffusion gradients above the cherts (Gieskes, 1976; Gieskes and Johnson, 1981).

Chlorinity

The chloride ion is considered conservative in marine sediments because there are generally no significant sinks or sources present (e.g., Sayles and Manheim, 1975). Four of the five samples from Unit IV were depleted by about 6% with respect to seawater. Such a depletion is due either to dilution by low-chlorinity water or to uptake of chloride in solid phases during alteration. Chloride uptake by serpentine has been documented elsewhere (Miura et al., 1981), however, serpentine is uncommon in this unit. Dilution by low-salinity water could be related to several processes:

1. Pollution by drilling fluids or during squeezing. Mud injected episodically while drilling contains low-chlorinity water (Table 4, analysis of water extracted from mud) and hence could dilute interstitial water. This cause can be ruled out because (1) no mud was injected during drilling of Core 129-800A-49R and during the three previous cores, and (2) the calcium content of the mud water is 10 mmol/L; hence, pollution would induce a calcium decrease whereas a slight increase is observed. During handling of the sample, pollution is very unlikely because only seawater is in contact with the sample.
2. Dehydration related to diagenetic reactions such as degradation of organic matter or the smectite to illite reaction. These reactions are not important in this context. Only the opal-A/opal-CT/quartz transformation is likely to release water, but this reaction produces only a small amount.

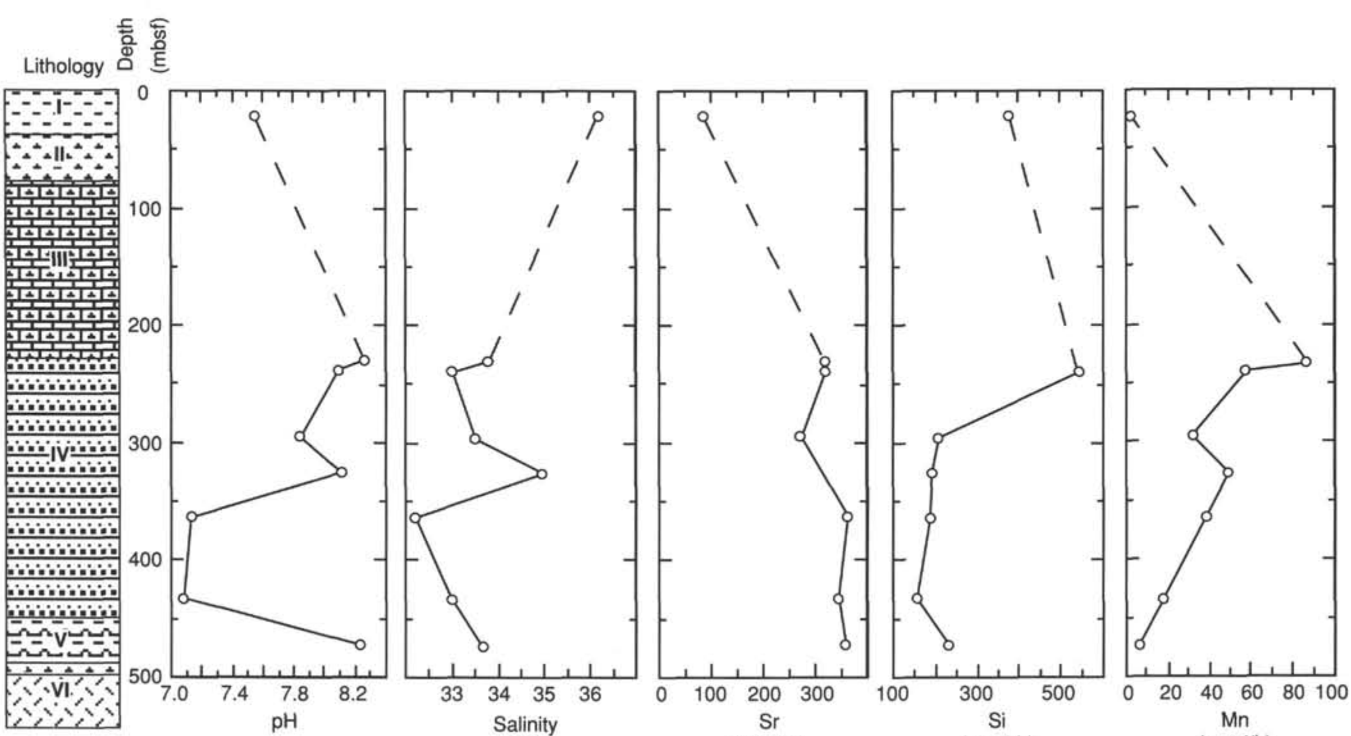

Figure 25. Profiles of depth vs. pH, salinity, and Sr, Si, and Mn concentrations in interstitial water extracted from sediments in Hole 800A. The lithostratigraphic column refers to the lithologic units defined in the "Lithostratigraphy and Sedimentology" section (this chapter). Unit I = brown clay, Unit II = red chert and porcelanite, Unit III = silicified limestone and chert, Unit IV = volcaniclastic turbidites, Unit V = brown claystone, and Unit VI = aphyric basalt.

3. Ultrafiltration process in which chloride ions are retained in a clay-rich formation, producing low-chlorinity water that could percolate in the sampled area. The abundance of clay minerals in Unit IV and below is too low to generate fresh water by membrane filtration.

4. Dewatering of smectite-type minerals. This remains the more probable explanation, but needs to be supported by mineralogical data. The only direct argument in favor of this process is the observation that the only sample from Unit IV that is not rich in clay minerals is also the least depleted in chloride (Sample 129-800A-37R-2, 0–10 cm; 554 mmol/L). The dewatering would certainly occur during the compaction of the sediments. The alternative is that interlayer water is released during squeezing, but this would happen for all squeezed smectite-rich sediments, which is not the case. Dewatering of hydrous minerals was proposed to explain low chlorinity values in Legs 116 (Shipboard Scientific Party, 1989), 123 (Shipboard Scientific Party, 1990a), and 125 (Shipboard Scientific Party, 1990b).

Calcium, Magnesium, Potassium, and Sodium

A calcium increase associated with magnesium and potassium depletion is well known and documented in numerous DSDP-ODP reports. It is attributed to either the effect of alteration of basaltic basement or to diagenetic reactions with the sediment itself. In Hole 800A, the absence of a concentration gradient from 232 to 473 mbsf (top of Unit IV to basement) indicates that it is the alteration of these volcaniclastic turbidites that releases calcium and uptakes magnesium and potassium, probably during the formation of authigenic smectite and zeolite. The exact reactions responsible for these variations must be further documented on the basis of detailed mineralogical and geochemical studies of the sediments. However, the consistent presence of green clays, which could be either celadonite, glauconite, or saponite (see "Lithostratigraphy and Sedimentology" section, this chapter) is certainly a sink for magnesium. Clinoptilolite, also common in Unit IV, may have taken up potassium. Less common in interstitial water is a sodium depletion. Mineralogical investigations are necessary to identify which phase could uptake sodium in the sediment, but the most likely sink is the formation of zeolites. In Cores 129-800-27R and -49R, the absolute sink in sodium reaches 80 mmol/L or 60 mmol/L if it is corrected for a possible dilution. This depletion is about 2 times that of magnesium; therefore, the reaction(s) involving sodium should be important.

Silica

Below the Unit III, silica concentrations decrease abruptly from 546 μmol/L at 240 mbsf to 206 μmol/L at 296 mbsf. The high concentration at 239.40 mbsf is probably due to the proximity of the cherts of Unit III and the sink in silicon may be related to the formation of authigenic clays and zeolites.

Manganese

The progressive decrease in manganese observed from 232 to 473 mbsf (top of Unit IV to the Unit V) reflects the observed increase of manganese oxide minerals in veins (see "Lithostratigraphy and Sedimentology" section, this chapter) toward the bottom and the oxidizing conditions in Unit V.

Conclusion

Interstitial water compositions in sediments recovered from Hole 800A are controlled by three main factors: (1) the presence of the cherts in Unit III which act as a diffusional barrier; (2) the diagenetic and alteration reactions in the volcaniclastics of Unit IV which deplete the water in sodium, magnesium, potassium, and silicon, and release calcium; and (3) the compaction that probably enhances release of interlayer water from smectite-type clays in Unit IV. It is possible that this is observed in this site because the low porosity of Unit III prevents diffusion to erase such concentration gradient.

PHYSICAL PROPERTIES

Determination of physical properties of sediments and rocks recovered at Site 800 was based only on measurements using discrete samples. Continuous measurements provided by the gamma-ray attenuation porosity evaluator (GRAPE) and compressional-wave (*P*-wave) logger were not obtained because sediments and rocks typically did not completely fill core liners, or in the recovery of soft sediments, the cores were too highly disturbed. Physical properties measured on discrete samples are listed in Table 5 and include index properties (wet-bulk density, porosity, water content, and grain density), compressional-wave velocity, and thermal conductivity. All techniques and equipment used in making the measurements are described in the "Explanatory Notes" chapter (this volume). Differences in the properties of the various lithologies encountered at Site 800 can be identified in the physical properties data. However, because of the low recovery rate and low sampling frequency, trends in physical properties variation within the lithologic units are not well defined.

Index Properties

Variations in index properties among the six lithologic units identified at Site 800 are described in the following section in terms of porosity, wet-bulk density, and grain density. Water content varies directly with porosity. Values for water content are listed in Table 5 and plotted in Figure 26. Wet-bulk density was determined by gravimetric and 2-min GRAPE techniques. The values cited are those of the gravimetric analyses, unless otherwise specified. Grain density was determined for all samples using solid "chunks" and for a limited number of powdered samples (Table 5). Analyses of powdered samples are believed to be the more accurate determinations at this site.

Pelagic brown clays of lithologic Unit I (0–38.0 mbsf) were sampled for index properties in Cores 129-800-3R and -4R. The pelagic clays were highly disturbed by rotary coring, and measured values of porosity and wet-bulk density, which average 81.0% and 1.34 g/cm^3, respectively, should be viewed with caution. Grain density averages 2.65 g/cm^3 for the pelagic clays.

The porcellanites and cherts of lithologic Unit II (38.0–78.2 mbsf) display downsection trends of decreasing porosity and increasing wet-bulk density and grain density (Fig. 26). The grain density of these opal-rich sediments is low, ranging from 2.32 to 2.34 g/cm^3. The increase in grain density with depth combined with the downsection decrease in porosity from 25.7% to 22.2% produces an increase in wet-bulk density of 2.00 to 2.05 g/cm^3 with depth.

Trends of decreasing porosity and increasing wet-bulk density and grain density that characterize Unit II continue in the uppermost part of lithologic Unit III (78.2–228.6 mbsf). The trends for porosity and wet-bulk density are reversed at 88.84 mbsf, at which depth values for porosity and wet-bulk density are 10.0% and 2.30 g/cm^3, respectively (Table 5). The increase in grain density continues to 97.40 mbsf, where it is 2.47 g/cm^3. Below 108 mbsf in Unit II the variability in grain density increases in response to fluctuations in calcium carbonate concentration (see "Lithostratigraphy and Sedimentology" section, this chapter). Grain density and calcium

Table 5. Physical properties summary for Site 800.

Core, section, interval (cm)	Depth (mbsf)	Wet-bulk density Gravimetric (g/cm³)	Wet-bulk density GRAPE (g/cm³)	Grain density[a] (g/cm³)	Porosity (%)	Water content (%)	Vertical velocity (m/s)	Horizontal velocity (m/s)	Velocity anisotropy (%)	Thermal conductivity (W/m · K)	Remarks
129-800A-											
3R-1, 82–85	11.42	1.30		2.62	82.8	64.8	1481			0.91	Pelagic clay
3R-2, 20	12.30									0.93	Pelagic clay
4R-1, 115–118	21.35	1.34		2.67	81.1	61.8				0.87	Pelagic clay
4R-3, 58–60	23.78	1.37		2.66	79.0	58.8	1460			0.91	Pelagic clay
6R-1, 35–37	39.95	2.00		2.01(2.34)	25.7	13.1	3412	3713	8.4		Porcellanite
8R-1, 2–4	58.92	1.96		2.16(2.32)	27.5	14.2	3032	3196	5.3		Chert
9R-1, 10–12	68.60	2.05		2.21(2.34)	22.2	11.0	3229				Chert
10R-1, 32–34	78.52	2.09	2.07	2.15(2.37)	21.1	10.3	3459	3561	2.9	1.81	Radiolarian chert and porcellanite
11R-1, 104–106	88.84	2.30	2.27	2.22(2.44)	10.0	4.4	4276	4539	6.0	1.85	Chert
12R-1, 10–12	97.40	2.26	2.21	2.30(2.47)	14.3	6.4	3838	4184	8.6	2.09	Siliceous limestone
13R-1, 62–64	107.42	2.22	2.18	2.29(2.47)	17.1	7.8	3628	3669	1.1		Siliceous limestone
14R-1, 1–3	116.21	2.02	2.02	2.39	27.0	13.6	2954	3164	6.9	1.44	Siliceous limestone
15R-1, 36–38	125.76	2.41	2.40	2.36(2.52)	7.0	3.0	4823	5100	5.6		Siliceous limestone
16R-1, 30–32	135.20	2.17	1.97	2.10(2.43)	18.4	8.6	3458	3523	1.9		Siliceous limestone
17R-1, 47–49	144.67	2.26	2.24	2.28(2.51)	16.5	7.4	3651	3690	1.1	1.65	Porcellaneous limestone
18R-1, 127–129	154.87	1.91	1.95	2.37	34.3	18.3	2533	2535	0.1	1.04	Porcellanite
19R-1, 23–25	163.13	1.99	2.00	2.47	33.5	17.1	2467	2569	4.1	1.63	Siliceous radiolarian limestone
21R-1, 65	181.95									0.94	Nannofossil chalk
21R-1, 135–137	182.65	2.08	2.05	2.69	36.9	18.1	2083	2150	3.2	1.53	Nannofossil chalk
22R-1, 25–27	191.25	2.14	2.15	2.51	24.9	11.8	2967	2907	−2.0	1.48	Siliceous limestone
23R-1, 53–56	201.03	2.15	2.16	2.45	21.3	10.1	3281	3375	2.8	1.78	Siliceous limestone
24R-1, 120–122	211.10	2.12	2.29	2.27	12.2	5.9	4119	4335	5.1	0.89	Siliceous limestone
25R-1, 42–44	219.72	1.92	1.89	2.48	38.3	20.3	2379	2662	11.2		Radiolarite
26R-1, 126–128	229.86	1.96	1.96	2.66	42.9	22.3	2039	2236	9.2	0.86	Volcaniclastic silty sandstone
26R-3, 54–56	232.14	2.00	1.98	2.84	46.2	23.5	2380	2420	1.7	1.16	Volcaniclastic sandstone
27R-1, 16–18	238.16	1.91	1.91	2.70	47.4	25.3	1911	2079	8.4	1.30	Silty claystone
28R-1, 33–35	247.53	1.88	1.88	2.84	52.8	28.6	1792	1899	5.8	0.97	Volcaniclastic siltstone
28R-3, 70	250.90									1.02	Clayey siltstone
28R-3, 73–85	250.93	1.88	1.92	2.64	47.2	25.6	1822	1927	5.6	1.04	Clayey siltstone
28R-5, 76–78	253.96	1.77	1.76	2.80	58.2	33.5	1773	1882	6.0		Silty claystone
29R-2, 29–31	258.29	1.80	1.79	2.74	54.7	30.9	1787	1857	3.8		Clayey siltstone
29R-3, 69–71	260.19	1.95	1.88	2.54	39.2	20.5	2235	2431	8.4		Volcaniclastic sandstone
30R-1, 42–44	266.32	1.99	1.93	2.47	33.6	17.2	2735	3438	22.8		Volcaniclastic clayey siltstone
30R-2, 102–104	268.42	1.98	1.96	2.55	37.7	19.4	2401	2609	8.3	1.51	Porcellanite
31R-1, 53–55	272.53	1.89	1.88	2.56	44.0	23.8	2166	2333	7.4	0.99	Clayey siltstone
31R-2, 34–36	273.84	2.06	2.02	2.87	43.9	21.7	2554	2569	0.6	1.32	Volcaniclastic sandstone
31R-2, 120	274.70									1.05	Volcaniclastic sandstone
32R-1, 101–103	279.11	2.14	2.07	2.68	32.5	15.4	2655	2676	0.8	1.42	Volcaniclastic sandstone
33R-1, 29–31	287.79	1.79	1.81	2.66	53.0	30.1	1844	1922	4.1	0.77	Volcaniclastic siltstone
33R-3, 73–75	291.23	2.29	2.30	2.82	29.6	13.2	3049	3110	2.0	0.66	Volcaniclastic sandstone
33R-5, 12–14	293.62	2.19	2.18	2.75	32.5	15.1	3107	3009	−3.2	0.85	Volcaniclastic sandstone
34R-1, 60–62	297.60	2.15	2.15	2.76	35.2	16.7	2783	2794	0.4	1.27	Volcaniclastic sandstone
34R-3, 115–117	301.15	1.80	1.79	2.82	57.1	32.4	1749	1819	3.9	1.35	Silty claystone
35R-1, 47–49	306.87	1.89	1.89	2.72	49.3	26.6	1909	1991	4.2	1.43	Volcaniclastic silty claystone
35R-3, 36–38	309.76	1.75	1.75	2.69	56.3	32.7	2038	2070	1.6	1.28	Volcaniclastic sandstone
36R-1, 63–65	316.53	2.02	2.04	2.78	43.3	21.8	2563	2540	−0.9	1.26	Volcaniclastic sandstone
36R-3, 76–78	319.66	1.71	1.79	2.50	53.9	32.1	1822	1913	4.9	1.26	Volcaniclastic clayey siltstone
37R-1, 46–48	325.56	1.89	1.87	2.80	51.2	27.6	2275	2259	−0.7	1.26	Volcaniclastic sandstone
38R-1, 112–114	335.62	1.61	1.77	2.26	52.8	33.4	1772	1804	1.8	1.20	Claystone
39R-2, 41–43	345.71	1.66	1.80	2.37	52.6	32.2	1759	1842	4.6	1.08	Volcaniclastic silty-claystone
39R-3, 64–66	347.44	1.67	1.72	2.63	59.7	36.4	1856	1841	−0.8	1.22	Volcaniclastic sandstone
40R-1, 39–41	353.49	2.04	2.00	2.86	44.9	22.4	2491	2503	0.5	1.05	Silty claystone
41R-1, 20–22	362.70	1.97	1.95	2.85	48.5	25.2	2253	2239	−0.6	1.22	Sandstone breccia
42R-1, 53–55	369.13	1.78	1.74	2.75	56.5	32.4	1951	2043	4.6		Claystone breccia
43R-1, 105–107	375.75	1.74	1.73	2.70	57.4	33.6	1965	1979	0.7	0.84	Claystone breccia
44R-1, 124–126	384.94	1.99	1.98	2.77	44.9	23.0	2375	2386	0.5	1.21	Volcaniclastic sandstone
45R-1, 85–87	393.95	1.97	1.97	2.74	44.9	23.2	2545	2534	−0.4	1.03	Volcaniclastic sandstone
46R-1, 78–80	403.28	2.05	1.97	2.79	41.8	20.7	2023	1908	−5.9	1.62	Radiolarian claystone
46R-3, 43–45	205.93	1.85	1.80	2.77	52.7	29.0	2058	2109	2.4	1.26	Silty breccia
47R-1, 89–90	412.79	1.93	1.95	2.75	47.8	25.3	2340	2268	−3.1	1.25	Volcaniclastic sandstone
47R-3, 79–81	415.69	1.97	1.99	2.82	47.5	24.6	2321	2348	1.2	1.25	Volcaniclastic sandstone
48R-1, 7–9	421.47	2.03	2.04	2.73	41.5	20.8	2681	2664	−0.6	1.25	Volcaniclastic sandstone
48R-4, 21–23	426.11	2.09	2.07	2.80	40.2	19.6	2698	2640	−2.2	1.34	Volcaniclastic sandstone
48R-5, 147–149	428.87	1.95	1.90	2.78	47.5	24.8	2124	2184	2.8	1.24	Sandy siltstone
49R-1, 35–37	431.25	1.85	1.87	2.77	53.1	29.3	2027	2076	2.4	1.14	Volcaniclastic sandstone
49R-4, 43–45	435.83	1.86	1.86	2.75	51.9	28.5	2212	2194	−0.8	1.23	Volcaniclastic sandstone
50R-1, 81–83	441.01	1.61	1.60	2.70	65.0	41.1	1668	1708	2.4	1.20	Volcaniclastic silt-claystone
50R-3, 18–20	443.38	2.01	1.99	2.79	44.4	22.5	2496	2464	−1.3	1.28	Volcaniclastic sandstone
51R-1, 71–73	450.31	2.07	1.99	2.66	36.1	17.7	2301	2443	6.0		Siliceous claystone
52R-2, 118–120	461.48	1.97	1.93	2.68	43.2	22.4	1962	1945	−0.9	1.56	Clay radiolarite
53R-1, 128–130	466.18	1.98	1.99	2.59	38.8	19.9	2102	2157	2.6	1.58	Clayey radiolarite
54R-2, 57–59	473.07	1.93	1.89	2.69	45.7	24.0	1882	1980	5.1	1.65	Radiolarian claystone
55R-2, 62–64	481.22	1.90	1.85	2.65	46.0	24.6	1890	1898	0.4	1.68	Radiolarian claystone
56R-1, 38–40	488.88	2.56	2.45	2.46(2.63)	4.2	1.7	5296	5419	2.3		Chert
57R-1, 22–24	498.22	2.53	2.35	2.73(2.78)	14.1	5.7	4025	3963	−1.6	1.68	Dolerite
57R-2, 87–89	499.37		2.48		15.6[b]		4542	4496	−1.0	1.81	Dolerite
57R-2, 98–100	499.48	2.54	2.49	2.72(2.72)	10.8	4.3	4656	4514	−3.1	1.92	Dolerite
58R-1, 49–51	507.69		2.54		12.2[b]		4658	4564	−2.0	1.65	Dolerite
59R-1, 7–9	516.67		2.57		10.6[b]		4646	4576	−1.5	1.61	Dolerite
60R-1, 44–46	526.34		2.53		12.7[b]		4279	4417	3.2	1.70	Dolerite
60R-1, 69–71	526.59	2.58	2.53	2.76(2.79)	11.9	4.7	4442	4219	−5.1	1.77	Dolerite

[a] Values in parentheses were determined using powdered samples.
[b] Porosity determined from GRAPE wet-bulk density.

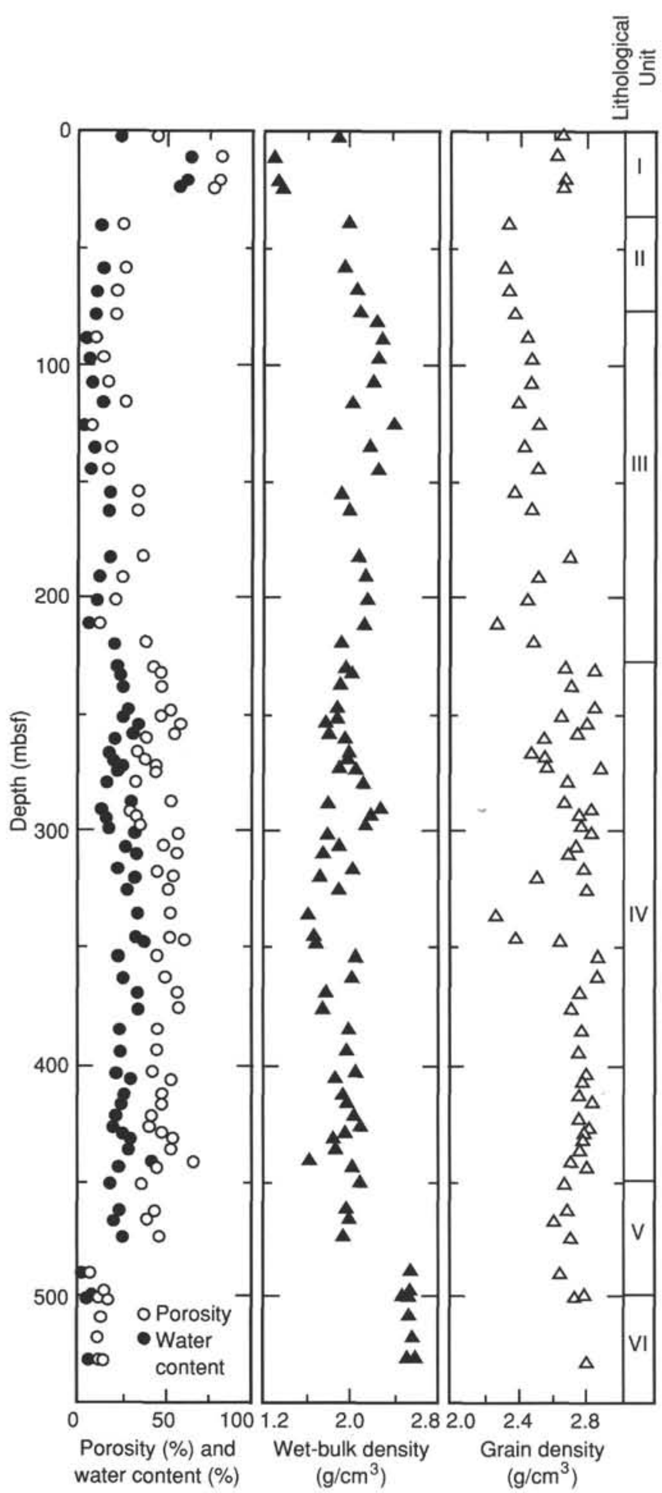

Figure 26. Index properties (porosity, water content, wet-bulk density, and grain density) vs. depth for Hole 800A.

carbonate concentration vary directly in this interval. The downsection increase in calcium carbonate concentration and change in composition from chert to siliceous limestone in Unit II (see "Lithostratigraphy and Sedimentology" section, this chapter) are reflected by increasing porosity and grain density with depth, below 89 mbsf (Fig. 26). Maxima in porosity (36.9%) and grain density (2.69 g/cm^3) occur at 182.65 mbsf and coincide with a carbonate concentration maximum (82%). Below this depth, porosity and grain density decrease rapidly to values of 12.2% and 2.27 g/cm^3, respectively, at 211.10 mbsf. Decreasing porosity and grain density between 183 and 211 mbsf coincide with an increase in silica concentration, indicated on geochemical logs (see "Downhole Measurements" section, this chapter). The covariance of porosity and grain density in Unit III has opposing effects on wet-bulk density, and wet-bulk density varies irregularly between 1.91 and 2.30 g/cm^3 (Fig. 26). Below 211.10 mbsf sharp increases in porosity and grain density and a decrease in wet-bulk density characterize the transition zone between lithologic Units III and IV. At 219.7 mbsf the respective values for porosity, grain density, and wet-bulk density are 38.3%, 2.48 g/cm^3, and 1.92 g/cm^3.

Highly variable porosity, wet-bulk density, and grain density characterize the volcaniclastic sediments of lithologic Unit IV (228.6–449.6 mbsf) (Fig. 26). Variability of the index properties in part is related to sampling both coarse-grained rocks (sandstones and breccias) and fine-grained rocks (siltstones and claystones); however, variation in properties within these two general rock types is also large. Porosity of the fine-grained rocks ranges from 33.6% to 65.0%, whereas porosity of the coarse-grained volcaniclastic rocks varies between 29.6% and 56.3%. Variation in wet-bulk density is of similar scale (Fig. 26), and values range from 1.61 to 2.29 g/cm^3. Grain density displays large variations in the upper part of Unit IV, between 228.6 and 362.7 mbsf, with values ranging from 2.26 to 2.86 g/cm^3 (Fig. 26). Between 362.7 mbsf and the base of Unit IV, grain density is more closely clustered about an average value of 2.76 g/cm^3.

Claystones and radiolarites of Unit V (449.6–498.1 mbsf) are characterized by a more regular increase in porosity and decrease in wet-bulk density with depth. Grain density is nearly constant at 2.65 g/cm^3. In Unit V porosity increases downsection from 36.1% at 450.31 mbsf to 46.0% at 481.22 mbsf (Fig. 26). Over this interval wet-bulk density decreases from 1.99 to 1.85 g/cm^3. The lowermost sample from Unit V, at 488.88 mbsf, is chert, which is characterized by properties distinctly different from those of the other rocks in Unit V. The porosity of the chert is 4.2%, its grain density is 2.63 g/cm^3, and its wet-bulk density is 2.56 g/cm^3.

Dolerites of lithologic Unit VI (498.1–544.5 mbsf) are characterized by little variation in physical properties. Index property measurements were based on gravimetric and 2-min GRAPE analyses for three samples and 2-min GRAPE analyses only on an additional four samples. Porosities of rocks analyzed only with the GRAPE were estimated from the GRAPE wet-bulk density as outlined in the "Explanatory Notes" chapter (this volume). An average grain density of 2.75 g/cm^3 was assumed for these calculations. Porosity of the dolerites is high, ranging from 10.6% to 15.6%. The highest porosity values are from Section 129-800-57R-1, which is contained in the oxidized interval of the upper flow unit within Unit VI. Wet-bulk density of the dolerites varies between 2.35 and 2.58 g/cm^3, and grain density of these rocks ranges from 2.72 to 2.79 g/cm^3. Low values of wet-bulk density 2.35 to 2.48 g/cm^3 characterize the upper flow unit of Unit VI.

Compressional-Wave Velocity

At Site 800, compressional-wave velocities were measured in both vertical and horizontal propagation directions. Velocity anisotropy was calculated as the difference between the horizontal and vertical velocities divided by the average velocity (see "Explanatory Notes" chapter, this volume). Large variations are present in the velocity data set. Despite the wide variation, trends that correspond to changes in physical properties and lithology can be recognized. Unless otherwise noted, the velocity values cited are for measurements made in the vertical direction.

Compressional-wave velocity was measured for two samples of questionably intact pelagic clay of Unit I (Table 5). The average of the measurements is 1470 m/s, less than the velocity of sound in seawater. This anomalous situation is not unusual for deep-sea sediments at shallow burial depths (Hamilton, 1974).

In lithologic Unit II velocity varies roughly directly with wet-bulk density and increases downsection to a local maxima of 4276 m/s in chert at 88.84 mbsf, near the top of Unit III (Fig. 27). Below 88.84 mbsf sonic velocity is highly variable in Unit III, varying roughly inversely with carbonate concentration. A velocity maxima of 4823 m/s occurs in siliceous limestone at 125.76 mbsf. Below this depth, velocity rapidly decreases to 2083 m/s in nannofossil chalk at 182.65 mbsf and subsequently increases downsection to 4119 m/s in siliceous limestone at 211.10 mbsf. The rapid increase in velocity between 183 and 211 mbsf correlates with a rapid decrease in grain density (Fig. 26) and increase in silica, as indicated by silica geochemical logs (see "Downhole Measurements" section, this chapter). The decrease in velocity at the base of Unit III coincides with an increase in grain density (Fig. 26). Velocity anisotropy for sediments and rocks of Units II and III ranges from 2.0% to 11.2% (Table 5). Anisotropy is high at the top of Unit II (8.4%) and at 97.40 mbsf in Unit III (8.6%). The general trend in anisotropy for Units II and III is a broad downsection decrease in anisotropy (Fig. 27), although the highest anisotropy (11.2%) was measured for a radiolarite sample near the base of Unit III, at 219.72 mbsf. High-velocity anisotropy in the radiolarite is associated with well-defined parallel lamination that characterizes these rocks.

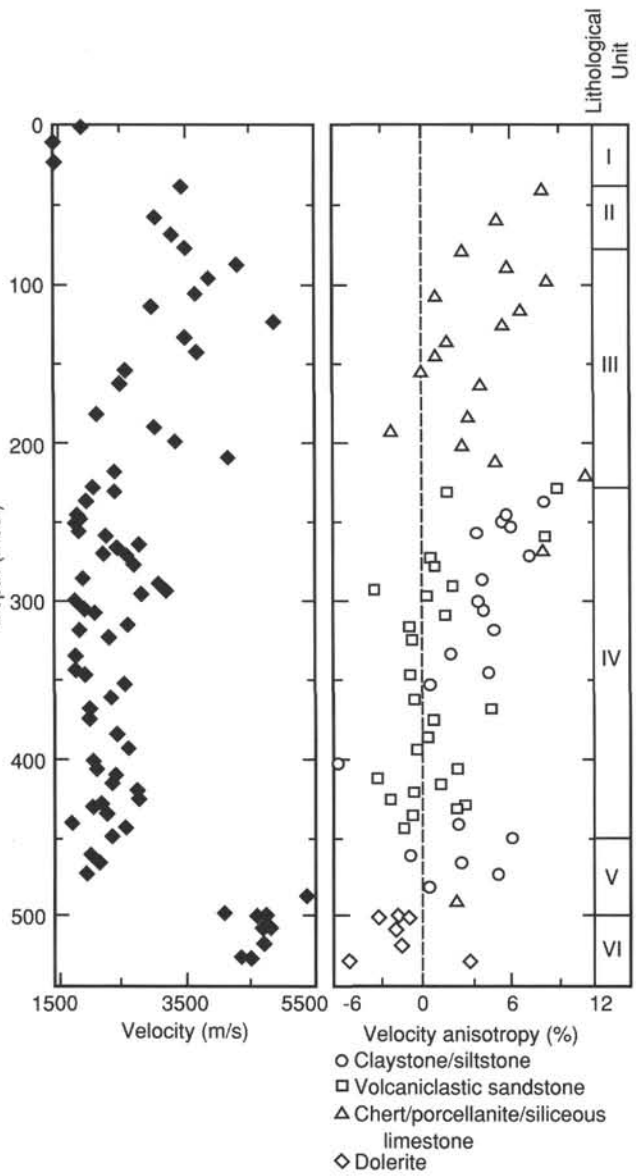

Figure 27. Compressional-wave velocity (measured perpendicular to bedding) and velocity anisotropy vs. depth for Hole 800A. Velocity anisotropy profile is coded according to sediment and rock type.

Lithologic Unit IV is characterized by distinct differences in the velocity of coarse-grained rocks (sandstones and breccias) and fine-grained rocks (siltstones and claystones) that comprise the unit. Velocity of the sandstones and breccias ranges from 1856 to 3107 m/s and averages 2371 m/s. Velocity of the siltstones and claystones of Unit IV ranges from 1668 to 2735 m/s and averages 1946 m/s. Well-defined trends in velocity variation with depth are not apparent in Unit IV (Fig. 27). Velocity anisotropy of rocks of Unit IV varies as a function of lithology. Fine-grained rocks typically display higher anisotropy than coarse-grained rocks in this interval (Fig. 27). Anisotropy of the claystones and siltstones ranges from 5.9% to 22.8% and is characterized by a general decrease downsection. Anisotropy of the sandstones and breccias ranges from 3.2% to 9.2%, with most values clustered near zero.

The claystones and radiolarites of lithologic Unit V display a regular decrease in velocity with depth from 2443 m/s at 450.31 mbsf to 1898 m/s at 481.22 mbsf (Fig. 27). This downsection decrease in velocity correlates with a downsection decrease in wet-bulk density in Unit V (Fig. 26). The chert in the lowermost part of Unit V is characterized by high wet-bulk density (2.56 g/cm^3) and the highest velocity measured at Site 800 (5296 m/s). Rocks of Unit V display a wide range in velocity anisotropy, from 0.9% to 6%, and no regular pattern in anisotropy variation.

The dolerites of Unit VI are characterized by little variation in compressional-wave velocity with depth (Fig. 27). Sonic velocity in these rocks ranges from 4025 to 4646 m/s (Table 5). The lowest velocity occurs in the oxidized interval at the top of Unit VI. All but one of the dolerite samples are characterized by higher vertical velocity than horizontal velocity. Velocity anisotropy in these rocks averages 1.6%.

The different sediment and rock types recovered at Site 800 show consistent relationships between wet-bulk density and compressional-wave velocity. The overall pattern is that of increasing velocity with increasing wet-bulk density (Fig. 28). However, the relationship between bulk density and velocity differs with differing lithologies. The lithologic grouping consisting of clays, claystones, siltstones, and radiolarite claystones displays the lowest velocities and the lowest velocity/density gradient (Fig. 28). The field represented by volcaniclastic sandstones and breccias on the crossplot of wet-bulk density and velocity overlaps that of the fine-grained sediments and rocks, but is characterized overall by higher velocities and a higher velocity/density gradient. Siliceous sediments encompass a wide area on the density-velocity crossplot. The variety of sediments included in this grouping, porcellanite, chert, and siliceous limestone, may account in part for the spread in the data. The siliceous sediments are characterized by velocities higher than those of other rocks at equivalent densities and the highest velocity/density gradient, a pattern consistent with previous studies of velocity-density

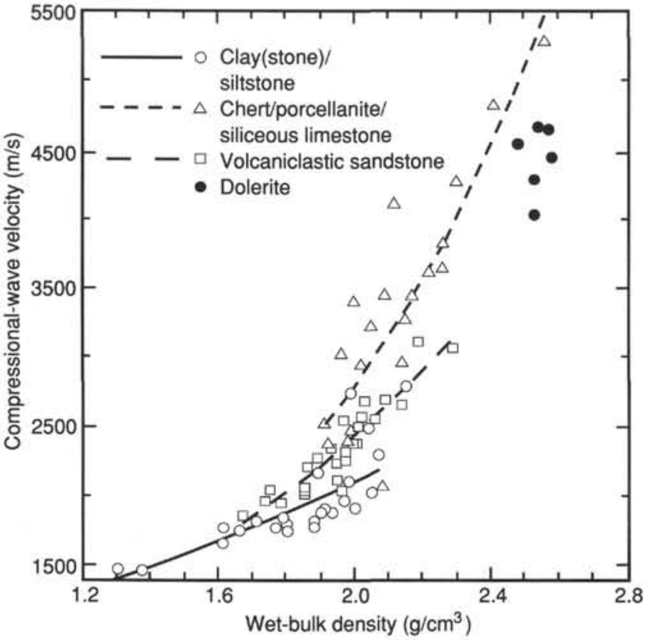

Figure 28. Wet-bulk density vs. compressional-wave velocity (measured perpendicular to bedding) for Hole 800A, coded according to sediment and rock type. Lines are best-fit exponential curves through the data.

relationships in deep-sea sediments (Hamilton, 1978). Density and velocity data for the dolerites do not define a clear relationship between the two parameters. However, velocities displayed by the dolerites are approximately equal to those predicted for oceanic basalts by empirical relations between bulk density and compressional-wave velocity established by Christensen and Salisbury (1975) for measurements made on oceanic basalts at 0.5 kbars effective pressure.

Thermal Conductivity

Thermal conductivity was measured for both sediments and rocks recovered at Site 800. The conductivity of soft sediments was measured by a heated needle probe inserted in the sediment. Conductivity of lithified sediments and basement rocks was measured by a heated needle probe sandwiched between the sample and a slab of low-conducting material. Details for both procedures for measuring thermal conductivity are described in the "Explanatory Notes" chapter (this volume). Fewer measurements of thermal conductivity were made than measurements of other physical properties because the rock fragments recovered were frequently too small to use with the needle probe technique.

General differences in thermal conductivity can be identified among the different lithologies recovered at Site 800 (Fig. 29). Pelagic clays of Unit I are characterized by a low and nearly constant conductivity averaging 0.90 W/m · K. Poor recovery precluded conductivity measurements for Unit II rocks. Silica-rich rocks of Unit III are characterized by high conductivity. The thermal conductivity of siliceous limestone at 97.40 mbsf is 2.09 W/m · K, the highest conductivity measured at Site 800 (Table 5). Thermal conductivity values for Unit III are highly variable, but the general trend is that of decreasing conductivity downsection. Thermal conductivity is also highly variable in the upper part of lithologic Unit IV, ranging from 0.66 to 1.51 W/m · K between the top of the unit and 300 mbsf. In this interval values less than 0.90 W/m · K are suspect either as a consequence of poor sample quality or

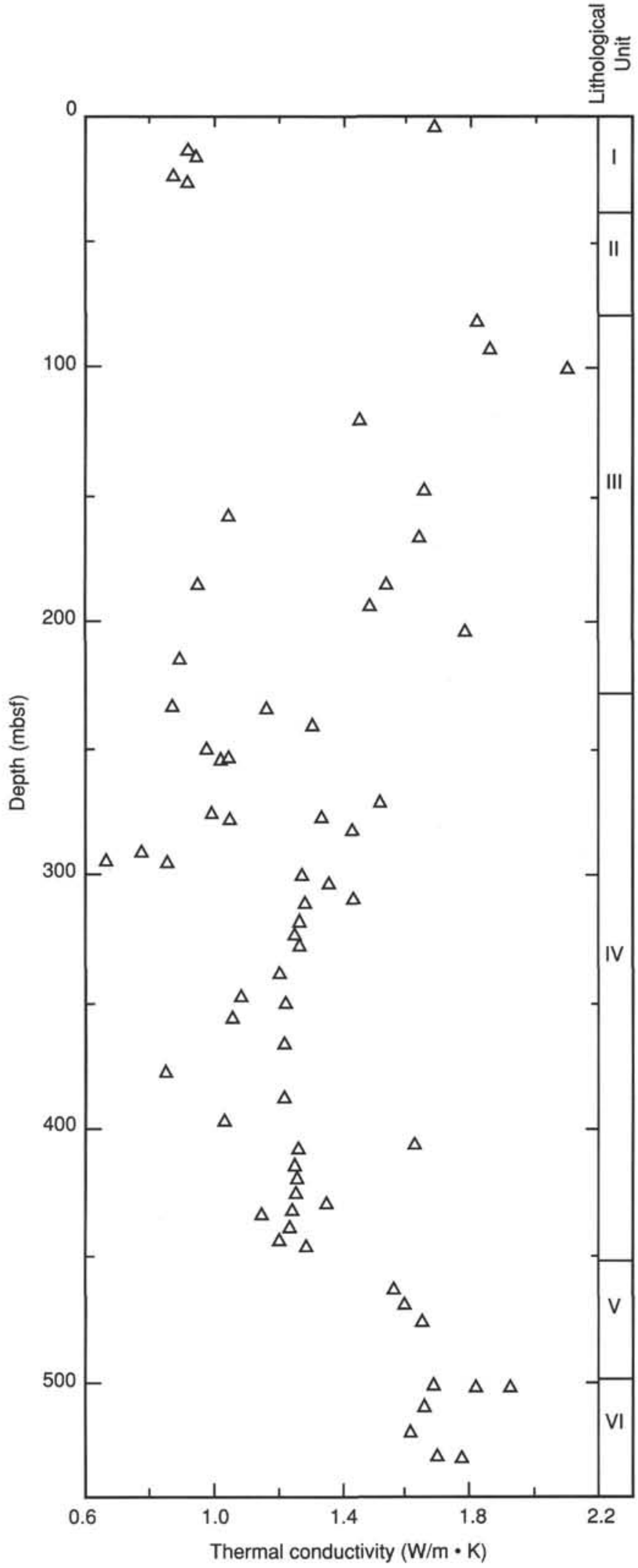

Figure 29. Thermal conductivity vs. depth for Hole 800A.

poor contact between the sample and needle. Below 300 mbsf in Unit IV most of the conductivity measurements fall in a relatively narrow range between 1.20 and 1.40 W/m · K. Thermal conductivity of the claystones and radiolarites of Unit V is markedly higher than that of the volcaniclastic rocks of Unit VI (Fig. 29). Unit V is also characterized by a steady increase in conductivity with depth, from 1.56 to 1.68 W/m · K. Thermal conductivity values measured for the dolerites of Unit VI range from 1.61 to 1.92 W/m · K (Table 5) and average 1.73 W/m · K. The largest variation in conductivity occurs in the altered rocks of the upper flow unit in Unit VI. The average conductivity for Unit VI rocks is slightly less than that reported for basalts from Hole 395A, 1.80 W/m · K (Hyndman et al., 1984) and Hole 648B, 1.77 W/m · K (Detrick et al., 1988). Porosities for basalts from these two holes, however, are less, averaging between 5% and 10%.

The combined sediment and rock conductivity data for Site 800 exhibit a moderately strong inverse relationship between porosity and thermal conductivity (Fig. 30). Figure 30 also illustrates potentially spurious conductivity measurements. Data in the field bounded by conductivities between 0.6 and 1.0 W/m · K and porosities between 10% and 60% fall markedly off the trend defined by the rest of the data and may represent inaccurate conductivity measurements.

IGNEOUS PETROLOGY

One of the hard-rock objectives of Leg 129 at Site 800 was to reach oceanic basement formed at magnetic anomaly M33 (~160 Ma) in the Pacific. Although a series of dolerites was penetrated at the base of Hole 800A, these rocks were not considered to represent "normal" ocean crust, because they (1) occurred just below sediments of lowermost Cretaceous age (~140 Ma), and (2) were interpreted to be intrusive sills rather than submarine lavas, as might be reasonably anticipated for true crust. We were also unable to determine their chemical signature relative to normal-type, mid-ocean ridge basalt (N-MORB) due to the nonoperation of the XRF spectrometer on board. Sills intruded into Cretaceous sediments were also encountered in the Nauru Basin during Leg 129

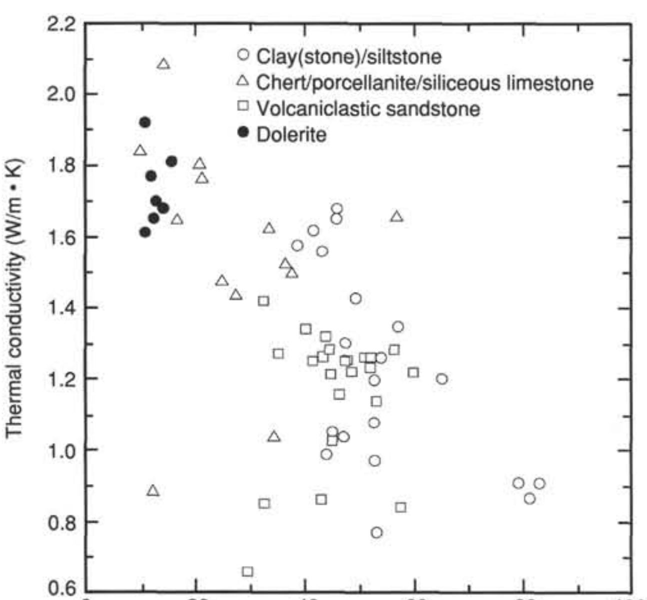

Figure 30. Porosity vs. thermal conductivity for Hole 800A, coded according to sediment and rock type.

(Hole 462), and were considered to be probably Aptian-Albian in age (Schlanger and Moberly, 1986). No chemical analyses are available to compare the two groups of intrusives, but preliminary data for the Hole 800A sills suggest they may be older than the Nauru sills and are petrographically distinct.

Lithology

Five cores (129-800A-57 through -61), representing about 12% recovery overall, sampled just over 7 m of dolerites. Although in gross terms the lithology is similar throughout, and actual contacts were not visible, three separate units within the dolerites were recognized on the basis of (1) a sedimentary interlayer, (2) systematic grain-size variations, and (3) macroscopic textural variations. Bearing in mind that a considerable amount of core is missing, the actual observed extent of each unit is shown in Table 6.

The contact between Unit 1 and the cherty sediments above (Fig. 31) is inferred from the upward-decreasing grain size and increasing degree of oxidation of the dolerite, as well as its more granular texture. The boundary between Units 1 and 2 is probably represented by slightly oxidized, dolerite drilling rubble at the base of Section 129-800A-57R-3 and indicates that a section of core is probably missing at this point. Red chert with silicified cream-colored and pale brown, laminated siltstones (at interval 129-800A-58R-1, 27–43 cm) marks the boundary between Units 2 and 3 (Fig. 32). The indurated and bleached nature of the sediment interlayer suggests that it had been thermally heated by intrusions. This feature, together with the relatively coarse texture of the dolerites, provides evidence for the sill-like nature of the igneous body. Sedimentary features allow the sediments to be directly compared with unaltered, laminated, brown and red siltstones and mudstones higher in the sequence just above the dolerites.

Petrography

In general terms, all the massive dolerites are medium-grained, aphyric, and largely holocrystalline, with very minor, glassy mesostasis (a few percent). Small, open miaroles (commonly 1 mm in diameter), lined with the terminations of plagioclase crystals or sometimes partly infilled with carbonate or clays, are randomly developed throughout.

The dolerites differ macroscopically and display three main textural variants:

1. Finer-grained, granular, equidimensional matrix (grains commonly <1 mm long), characteristic of the chilled facies at the top of Unit 1. In view of the reduced grain size this chilled zone is strictly a basalt, rather than a dolerite.
2. Medium-grained, hypidiomorphic-granular matrix (grains 1–2 mm in length) exhibiting black, stubby, and elongate prisms of pyroxene with white and green (clay-altered) plagioclase laths; featured in Unit 2.
3. Medium-grained, hypidiomorphic-granular matrix (grains commonly 1–5 mm in length), but characterized by long, straight (more rarely curved), skeletal-looking, black pyroxene crystals (5–15 mm long). The pyroxene may form

Table 6. Extent of sill units recognized in Hole 800A.

Unit no.	Interval Top	Interval Bottom	Sample thickness (cm)
1	129-800A-57R-1, 13 cm	129-800A-57R-3, 41 cm	192
2	129-800A-58R-1, 0 cm	129-800A-58R-1, 27 cm	27
3	129-800A-58R-1, 43 cm	129-800A-61R-1, 31 cm	489

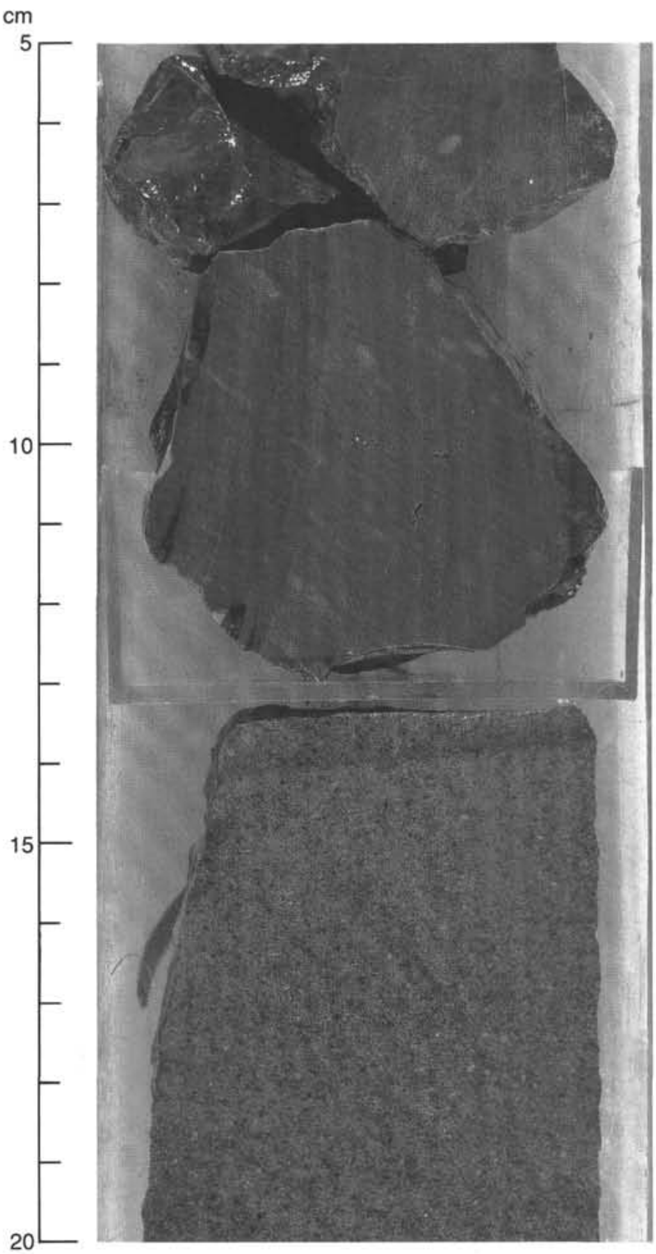

Figure 31. Photograph of the contact between dolerite Unit 1 and chert rubble in Section 129-800A-57R-1, 13 cm. Although much of the contact facies is missing, the dolerite is fine-grained, largely holocrystalline, and gradually increases in grain size down the unit. This section of dolerite also exhibits progressive oxidation toward the assumed contact.

crude radiate groups composed of 2 to 4 individual crystals. These long crystals are most pronounced in altered zones of Unit 3 where they stand out against a pale green clay matrix (Fig. 33). The actual length and thickness of the black pyroxenes may vary in a random fashion through this unit.

Thin-section examination of samples from Units 1 and 3 (Table 7) confirms that the dolerites are aphyric and generally medium-grained with a hypidiomorphic-granular texture containing no or minor mesostasis (1%–2%). The clinopyroxene is invariably a pink pleochroic titanaugite and suggests the dolerites have alkaline affinities. All are moderately to highly

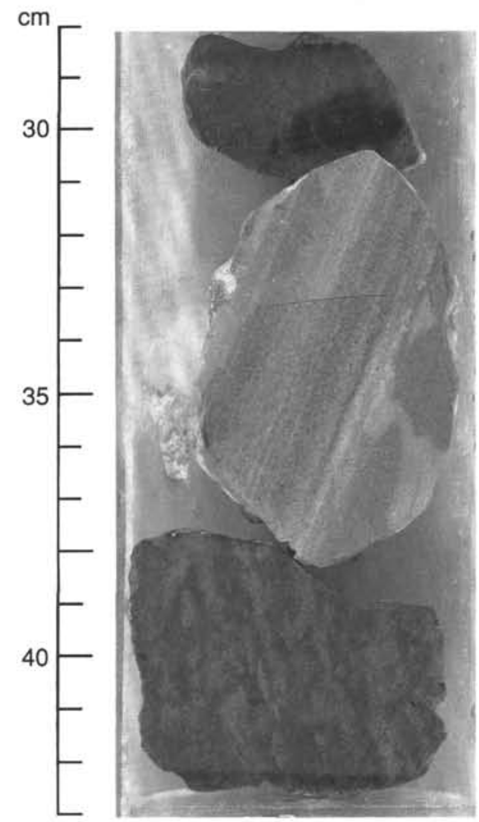

Figure 32. Photograph showing the baked chert and silicified siltstone interlayer between dolerite Units 2 and 3 within interval 129-800A-58R-1, 28–43 cm. The actual contacts between the lithologies were not recovered. The well-preserved lamination in the central siltstone block can be matched with unaltered, sedimentary material above the dolerites.

altered (see below) such that only plagioclase remains as an abundant, primary phase (40%–55%), whereas clinopyroxene and titanomagnetite may be totally replaced or remain as volumetrically reduced relicts (maximum fresh clinopyroxene content was on the order of 10%). Some petrographic features of the dolerites are illustrated in Figure 34. A brief description of the more important primary characteristics obtained from thin-section study follows.

Unit 1

Unit 1 shows a gradual increase in the grain size of primary plagioclase (An_{55-60}) from <1.0 mm (commonly 0.4–0.6 mm) to 1.0–1.5 mm towards the bottom of the unit. Secondary materials (see below) occupy the spaces between the plagioclase laths which may show Carlsbad, and more rarely, polysynthetic twinning. Zoning within the plagioclase is suggested by the cores often being replaced, whereas the rims are clear.

Units 2 and 3

Units 2 and 3 are dominated by primary plagioclase laths (0.5–5.0 mm in length) showing a range of composition from An_{35-70}, with more sodic values, probably representing secondary alteration. Most plagioclases are zoned with altered cores. Clinopyroxene (titanaugite) occurs both as anhedral grains or more commonly as elongate, subhedral prisms normally varying from 0.4 to 4.0 mm (longer prisms are seen in hand specimens). The macroscopic, skeletal-like form is due to variable alteration and replacement of the elongate

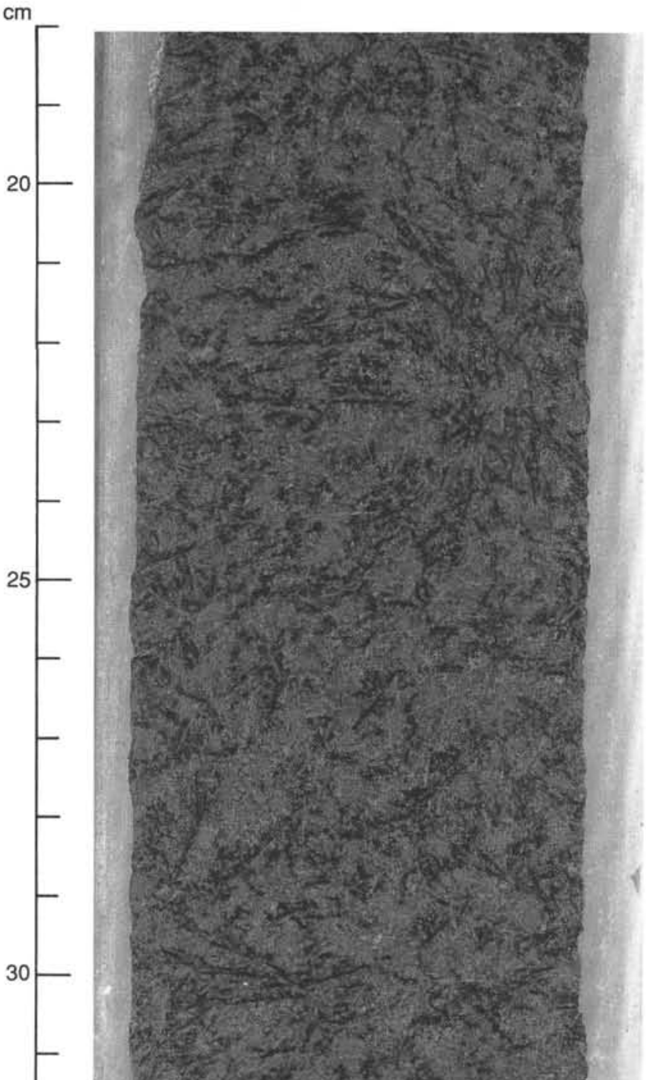

Figure 33. Characteristic texture of Unit 3 dolerite (interval 129-800A-58R-3, 18–32 cm) with individual and radiate groups of long, black, skeletal-looking pyroxenes set in a variably altered, clay-rich matrix.

prisms by secondary minerals that isolate fresh pyroxene relicts, which being in optical continuity, emphasize the extent of single crystals. A rare feature observed only in a few fresh clinopyroxene plates, is very small, round, and ovoid inclusions of brownish glass. Small subhedral and variably skeletal grains of titanomagnetite are common (about 2%) throughout both units, together with ubiquitous secondary pyrite, and show variable alteration depending on their proximity to the Unit 2/Unit 3 contact. The only other primary minerals observed are occasional, small apatite crystals. Some highly altered, angular-shaped zones between plagioclase laths have been interpreted as being originally glassy mesostasis, although the proportion is very low (a few percent) in these essentially holocrystalline rocks.

Alteration

The dolerites are moderately to highly altered (generally 20%–55%) due mainly to variable oxidation, clay development, carbonate, and other secondary minerals in minor proportions. Variation in the degree of alteration is seen at two core positions:

1. The top of Unit 1 (interval 129-800A-57R-1, 13–55 cm) is the most oxidized (as shown by hematite and a hydrated, iron-oxide, limonitic stain) with the degree of alteration decreasing downward from the assumed contact. The presence of an oxidized zone here implies alteration due to the downward percolation of oxygenated seawater, probably soon after consolidation of the sill. However, magnetic studies indicate that this section of core has a superimposed normal polarity (and small inclination) that is different from the rest of the fresher dolerite below which exhibits a reversed polarization throughout and a high inclination (+50°). This suggests that oxidation was a later phenomenon, possibly in response to a subsequent intrusion, or later volcanic activity that raised the ambient temperature of this zone.
2. The top of Unit 3 (Section 129-800A-58R-1) does not show much of an increase in the degree of alteration (30%) to the rest of the unit below, but a number of alteration domains composed of specific secondary phyllosilicates, as well as the presence of higher-grade amphibole and biotite, characterize this core section (see below). Magnetically, this zone (down to about Section 129-800A-58R-2, 80 cm; see "Paleomagnetics" section, this chapter) has a low inclination of 0°–10°, which steadily increases down the core and also reinforces the notion that Unit 3 is distinct from Unit 2 above which has a strong positive inclination (+50°).

Unit 1 is characterized by the presence of deep, red hematite almost totally replacing magnetite and pyrite, and with brown, limonitic stains covering clays and along mineral boundaries. Pale green, smectitic clays replace both pyroxene and plagioclase and together with carbonate and limonite, may sometimes totally replace plagioclase laths. Lower down in this unit, replacement takes the form of alteration domains typified by specific secondary minerals or assemblages. Three domains are recognized, comprising sericite and some carbonate (replacing plagioclase), opaque and brown smectites, and dark green chlorite (both replacing pyroxene). Throughout the altered matrix are colorless, acicular crystals of a zeolite (phillipsite?), although the proportion is low (about 1%). Of particular interest is the presence of biotite and traces of actinolite, both of which are restricted to the smectite- and chlorite-rich domains (see below).

Units 2 and 3 show similar alteration features to the lower portion of Unit 1 with abundant brownish smectites (20%–40%) and minor proportions of chlorite, carbonate, and zeolite. The most significant development at the top of Unit 3 (Sections 129-800A-58R-1 and -58R-2) is the presence of pleochroic, colorless to dull pale green actinolite and strongly pleochroic, pale yellow to red-brown biotite (about 5% and 1%, respectively). Both are secondary and, due to their generally unaltered nature and porphyroblastic growth within and across smectite and chlorite domains, have most probably formed later than the main, clay-rich alteration. In only a single recorded case do actinolite fibers replace a fresh, clinopyroxene crystal as a uralitic fringe. Lower down in the core, the proportion of actinolite rapidly drops, although the content of biotite, often seen as flakes, now independent of the actinolite, is maintained (2%–3%). Biotite may also nucleate on magnetite or grow within the interspaces of skeletal magnetite crystals. Occasionally it may be partly replaced by a bright, blue-green pleochroic "clay" which is tentatively identified as either smectite-chlorite or, more likely, celadonite.

Table 7. Approximate proportions (visual estimate) of primary and secondary phases in dolerites at the base of Hole 800A.

Core, section, interval (cm)	129-800A-57R-1, 20–22	129-800A-57R-2, 89–91	129-800A-58R-1, 46–47	129-800A-59R-1, 3–4	129-800A-60R-1, 43–44	129-800A-60R-1, 71–74
Piece	1	1E	2A	1A	1B	2
Primary minerals (%)						
Plagioclase	40	40	55	50	45	40
Clinopyroxene	0	0	10	10	5	5
Magnetite	0	2	2	2	1	2
Apatite	0	tr	0	0	tr	tr
Spinel	0	0	0	0	tr	0
Mesostasis	0	0	pr	pr	0	0
Secondary minerals (%)						
Smectitic clays	42	10	10	20	38	40
Celadonite(?)	0	0	1	5	3	4
Carbonate	3	5	0	5	tr	tr
Sericite	0	20	0	0	0	0
Zeolite	0	1	2	1	2	1
Chlorite	tr	18	11	tr	2	2
Hematite	9	0	0	0	0	1
Pyrite	2	3	3	4	2	2
Actinolite	0	tr	5	1	tr	tr
Biotite	4	1	1	2	2	3

Note: tr = trace constituent; pr = present.

In conclusion, the dolerites exhibit four alteration stages:

1. Initial development of smectitic clays, chlorite, sericite, and possibly zeolite. This mineral assemblage is typical of low-grade submarine alteration in the zeolite facies.
2. Oxidation probably followed stage 1 as clays are often iron stained. Also, carbonate appeared at a later stage relative to the clays, although it may span the oxidation phase as calcite and unaltered pyrite are seen as veinlets cutting all units.
3. Development of secondary actinolite and biotite. This implies a higher grade of alteration than stage 1, within the lower part of the greenschist facies.
4. Celadonite(?) alteration of biotite indicates relatively low grades of alteration again after stage 3.

A tentative explanation for the lower greenschist facies event, which is mainly recorded at the top of Unit 3, is the thermal effect of a subsequent intrusive sill, such as now represented by Unit 2.

Fractures and Veins

Thin (~1 mm wide), horizontal, and oblique (40° dip) veinlets occur spasmodically throughout the dolerites and are commonly filled with calcite (with or without pyrite) and rarer, dark green, saponitic(?) clay. Pyrite and calcite are also relatively common in the dolerite matrix. Alteration haloes or zones associated with the veinlets are not present.

Geochemistry

No geochemical analysis for major oxides or trace elements was achieved at Hole 800A. As part of the inorganic geochemistry program on the sediments, the dolerites were analyzed for carbon and sulfur (Table 8) and show high $CaCO_3$ values that correspond to concentrations of secondary calcite within the core.

Summary of Main Features

1. The only igneous rock lithology encountered in Hole 800A was a massive, aphyric, largely holocrystalline, slightly miarolitic alkali dolerite that was characterized by the presence of macroscopic, elongate, black pyroxene crystals.
2. Three dolerite units are recognized on the basis of textural variation and the presence of a sedimentary interlayer between Units 2 and 3.
3. The dolerites are moderately to highly altered, with the presence of ubiquitous green and brown smectitic clays, hydrated iron oxides, calcite, and pyrite, and lesser amounts of chlorite, sericite, and possibly celadonite. Apart from the above low-grade alteration assemblages, the presence of later secondary actinolite and biotite indicates a low greenschist facies event possibly caused by the emplacement of a subsequent, adjacent sill.

DOWNHOLE MEASUREMENTS

Operations

On 3 December 1989, after reaching a total depth (TD) of 544.5 mbsf, pipe was drawn up to 312 mbsf during a short wiper trip. The pipe was unable to penetrate below 335 mbsf on the run back to TD and at this point it was decided to prepare what was left of the hole for logging. The bit was dropped (with great difficulty) at 335 mbsf and the hole was filled with mud at an effective concentration of 2.5% KCl above that of seawater. The last circulation into Hole 800A was at 1845 hr UTC on 3 December. Logging operations began at Site 800 at 2025 hr on 3 December 1989 and were completed at 0015 hr on 5 December, corresponding to a total logging time of 28 hr (Table 9). The pipe was pulled to 70 mbsf for the beginning of each logging run and raised to approximately 50 mbsf while logging up hole.

The quad combination tool string (see "Downhole Measurements" section, "Explanatory Notes" chapter) included, from top to bottom, telemetry, long-spaced sonic, lithodensity, natural gamma-ray spectrometry, and dual induction resistivity tools, in addition to the Lamont temperature logging tool (TLT). These tools were rigged at 2145 hr on 3 December, creating a tool string 30.72 m long. At 0100 hr, this string was run down to 28 m above the mud line and held stationary for 3 min to obtain a bottom-water calibration point for the TLT. The depth to the end of pipe as recorded on this logging run was within .6 m of that calculated by the driller. As logging continued downhole it was reported that the wireline heave compensator (WHC) was not operating. The WHC was reportedly repaired in Singapore during dry dock prior to Leg 129 but was untested under full tensional load until the first logging run at Site 800. Down-going logging data were only acquired to 142 mbsf due to a hard disk failure in the recording

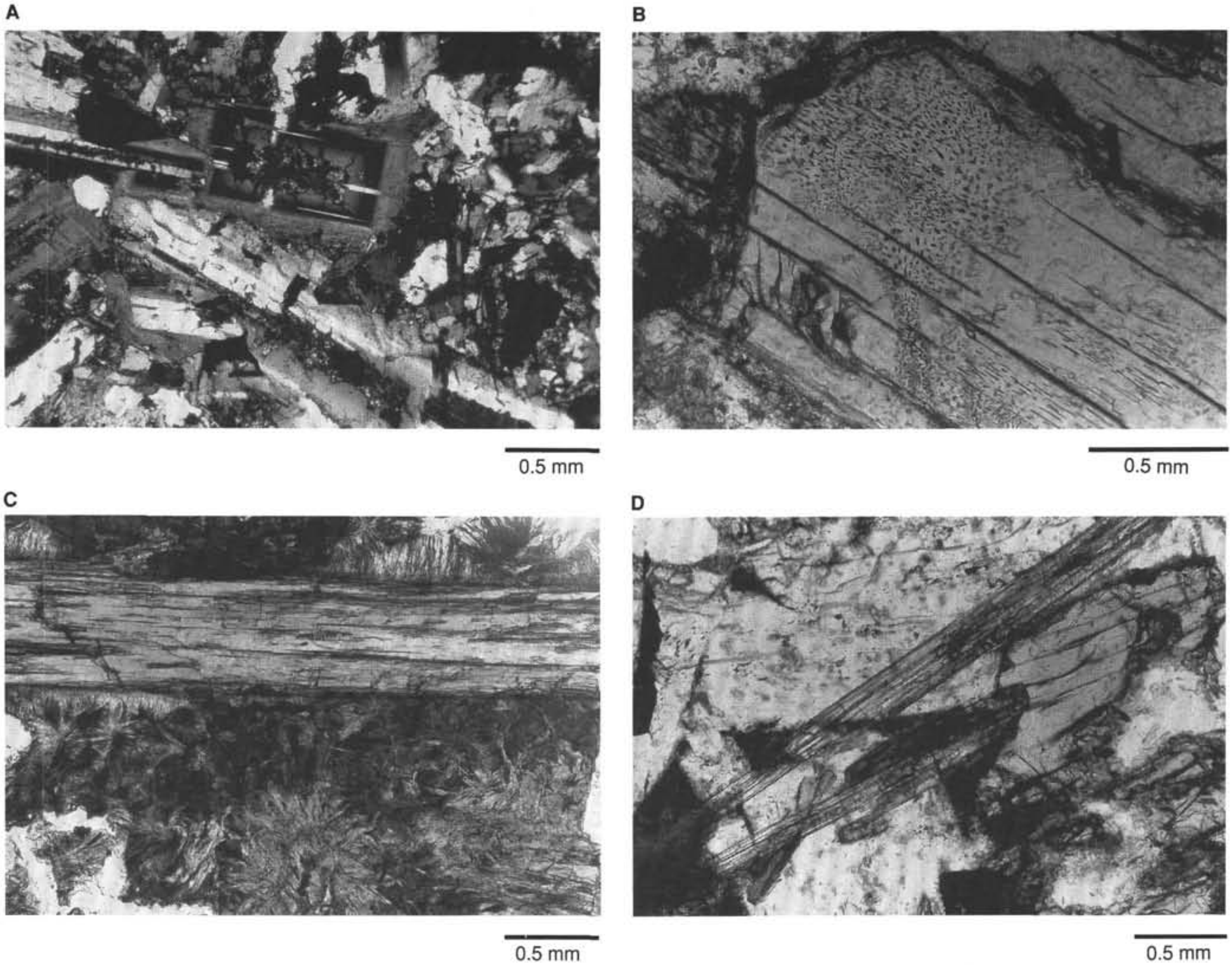

Figure 34. Photomicrographs illustrating some characteristic petrographic dolerites from Hole 800A. Scale bar = 0.5 mm. **A.** Zoned, twinned plagioclase laths with altered cores. Sample 129-800A-59R-1, 3–4 cm (crossed polars). **B.** Cloud of minute glass inclusions within clinopyroxene crystal. Sample 129-800A-60R-1, 43–44 cm (plane polarized light). **C.** Large, unaltered actinolite prism growing across groups of radiate smectite fibers. Sample 129-800A-58R-1, 46–47 cm (plane polarized light). **D.** Acicular zeolite fibers. Sample 129-800A-60R-1, 71–74 cm (plane polarized light).

unit. The tool string continued downhole until a bridge was encountered at 313.1 mbsf. Logging data were recorded successfully on a backup system as the tool string moved uphole at 300 m/hr from 312.3 to 50.6 mbsf (Fig. 35) with a repeat section taken from 312.3 to 222.2 mbsf. The bottom of pipe was encountered at approximately 50 mbsf and another bottom-water temperature calibration point for the TLT was obtained inside the pipe at 28 m above the mud line. The quad combination string was returned to the rig floor at 0600 hr on 4 December. The TLT was then taken from the rig floor to the downhole measurements lab, opened, and hard-wired to the Masscomp computer to download the recorded temperature/time measurements. The second of two TLT's was taken down to the rig floor and attached to the end of the geochemical combination tool string.

The geochemical tool string (see "Downhole Measurements" section, "Explanatory Notes" chapter, this volume), which included telemetry, natural gamma-ray spectrometry, aluminum clay, induced gamma-ray spectrometry, and Lamont temperature tools, was rigged at 0845 hr on 4 December creating a tool string 18.13 m long. This tool combination was lowered down the pipe and held stationary for 3 min at 28 m above the mud line to obtain a bottom-water calibration point for the TLT. The tool string encountered the bridge at 313.1 mbsf and logging data were recorded from 313.1 mbsf up into pipe at 43.12 mbsf as the tool string moved uphole at 200 m/hr (Fig. 36). A repeat logging run beginning at 244.2 mbsf was attempted but the neutron generator portion of the gamma-ray spectrometry tool failed. Another bottom-water temperature calibration point for the TLT was obtained inside the pipe at 28 m above the mud line and the geochemical logging run was completed at 1552 hr on 4 December.

The final tool combination run at Site 800 was the formation microscanner (FMS) (see "Downhole Measurements" section, "Explanatory Notes" chapter), which included telemetry, natural gamma-ray spectrometry, and the FMS tools (but no TLT). This tool string was rigged and in the hole at 1700 hr on 4 December. FMS data were recorded uphole at 260 m/hr from 312.3 to 50.6 mbsf with no problems. The final logging run ended at 0015 hr on 5 December with all tools off

Table 8. Carbon and sulfur analyses for dolerites at the base of Hole 800A.

Core, section, interval (cm)	Depth (mbsf)	$CaCO_3$ (wt%)	C_{org} (wt%)	S (wt%)	Comment
129-800A-					
57R-1, 17–24	498.17	3.0	0.00	0.02	Oxidized zone
57R-2, 86–91	499.36	3.2	0.02	0.20	Calcite-pyrite vein
58R-1, 47–51	507.67	0.4	0.00	0.04	Miarolitic
58R-2, 32–37	508.85	1.6	0.00	0.10	Calcite replacement
58R-2, 106–110	509.59	0.2	0.00	0.04	
59R-1, 4–9	516.64	1.1	0.00	0.06	
60R-1, 44–46	526.34	0.2	0.00	0.10	Miarolitic
60R-1, 69–74	526.59	0.2	0.00	0.00	

of the wireline and secured on deck. Logging depths recorded during the quad combination run were shifted to match drill-string depths (and thus coring depths). Subsequent logging runs were shifted relative to the quad combination using the natural gamma-ray log. The geochemical combination log was shifted upwards by 3 m and the FMS log was not shifted.

Summary log figures appear at the end of this chapter. The FMS images are presented on microfiche in the back of this volume.

Table 9. Actual time schedule (UTC) for logging operations at Hole 800A, including a listing of the tools used during each logging run.

Tool string	Time	Procedure
Quad combination (TCCB—LSS—HLDT—NGT—DIL—TLT)	RIH, 2145 hr UTC 3 December 1989 POOH, 0600 hr UTC, 4 December 1989	Log down to 13 mbsf. Run down to 312.3 mbsf (312.3 mbsf), log up to 50.6 mbsf. Run down to 312.3 mbsf, log up to 222.2 mbsf.
Geochemical combination (TCCB—NGT—ACT—GST—TLT)	RIH, 0845 hr UTC POOH, 15.52 hr UTC	Run down to 313.1, log up to 43.12 mbsf.
Formation microscanner (FMS—TCCB—NGT)	RIH, 1700 hr UTC POOH, 0015 hr UTC, 5 December 1989	Run down to 312.3 mbsf, log up to 50.6 mbsf.

Note: Total logging time = 28 hr (includes rig-up and final rig-down of tool strings). Abbreviations are as follows: TCCB = telemetry tool; LSS = long-spaced sonic tool; FMS = formation microscanner; HLDT = lithodensity tool; TLT = Lamont temperature tool; DIL = dual induction tool; ACT = aluminium clay tool; GST = induced gamma-ray spectrometry tool; NGT = natural gamma-ray spectrometry tool; RIH = Run in to hole; POOH = Pull out of hole.

Log Quality

The logs are generally of good quality (Figs. 35, 36, 37, and "Summary Log" following this chapter). The raw sonic data, however, required significant shipboard processing and editing to create a useful sonic log (Figs. 35 and 38). The data recorded from the induced gamma-ray spectrometry tool require post-cruise processing; references made to silicon, calcium, and iron are therefore only broadly qualitative. In contrast, the natural gamma-ray spectrometry tool produces reliable values for the concentration of potassium, thorium, and uranium and the aluminum clay log is generally little improved through post-cruise processing. The quad combination and geochemical logs are not obviously affected by ship's heave. The small degree of elasticity within the wireline summed over its extreme length (6000 m) may have acted to slightly decouple these logging tools from the heave of the ship. The ship's heave did adversely affect the raw FMS records, but these data would require significant shore-based image-processing to achieve an interpretable record even without these adverse effects.

Logging Units

Five logging units were identified in Hole 800A (Figs. 35 to 37) based on log response and analyses of recovered cores, but are not to be confused with the lithologic units defined earlier (see "Lithostratigraphy and Sedimentology" section, this chapter). The boundaries between adjacent logging units were placed at significant inflection points resulting from simultaneous variations on at least several of the logs illustrated in Figures 35 and 36. These units display consistent log responses or distinct overall trends.

Core recovery was poor throughout most of the logging interval (less than 10%) and only fragments of the most indurated portions of the formation were actually recovered. The lithologies for unrecovered intervals have been inferred from the logs based on the broad assumption that the logging tools respond to varying proportions of the primary constituents in samples actually recovered (e.g., biogenic silica, carbonate, pelagic clay, and volcanogenic clay) and to their relative porosity.

Logging Unit 1 (50.6–78 mbsf)

Logging Unit 1 is distinguished by covarying resistivity and total gamma-ray responses. This unit contains both the highest resistivity values (6–9 ohm-m) obtained in Hole 800A as well as extended high values of total gamma-ray (80 API), which are apparently due to a high uranium concentration (4.4–4.7 ppm). High values of uranium/thorium are often associated with increases in organic material (Fertl, 1979). The highest uranium/thorium ratios occur between 50.6 and 68 mbsf. Indeed, samples from Sections 129-800A-7R-CC and 129-800A-9R-CC (49.2–58.9 mbsf and 68.5–78.2 mbsf) contained abundant organic material (see "Lithostratigraphy and Sedimentology" section, this chapter). Logging Unit 1 is also characterized by high silicon and low calcium contents. The lower boundary of logging Unit 1 at 72–78 mbsf is marked by abrupt, simultaneous, local minima in velocity (1.9 km/s), resistivity (1 ohm-m), density (1.75 g/cm^3), uranium/thorium, and silicon, along with local maxima in total gamma-ray (79 API), aluminum (.35 wet wt%), and iron. These variations are juxtaposed against local minima/maxima in the opposite sense for all logs including a jump to higher calcium values from 78 to 81 mbsf. The inflection point for this sinusoidal variation in logs occurs at 78 mbsf and is chosen as the base of logging Unit 1. The high resistivity values, reflecting low porosity, together with the high relative silicon values, suggest that the chert and porcellanite recovered in this section accurately reflect the most indurated portion of this formation. The high total gamma-ray count and the high uranium/thorium ratio suggest that this formation may include a less indurated clay matrix containing an elevated concentration of organic matter. The logging response at the lower boundary of logging Unit 1 argues strongly for a volcanic clay-rich, chert-poor layer at approximately 75 mbsf, immediately overlying a more indurated, less porous layer containing silica and relatively more carbonate beginning at approximately 78 mbsf. The logging data correlate well with lithofacies unit II ("Lithostratigraphy and Sedimentology" section, this chapter) with the base of logging Unit 1 and lithofacies Unit II coinciding exactly.

Logging Unit 2a (78–142 mbsf)

Logging Unit 2a is characterized by relatively low sonic velocities (1.7–2.2 km/s), low resistivities (1–2 ohm-m), initially high total gamma-ray (55–70 API) decreasing to 25 API from 107 to 127 mbsf, and a relatively high calcium/silicon ratio that increases with depth and reaches a maximum in logging Unit 2b.

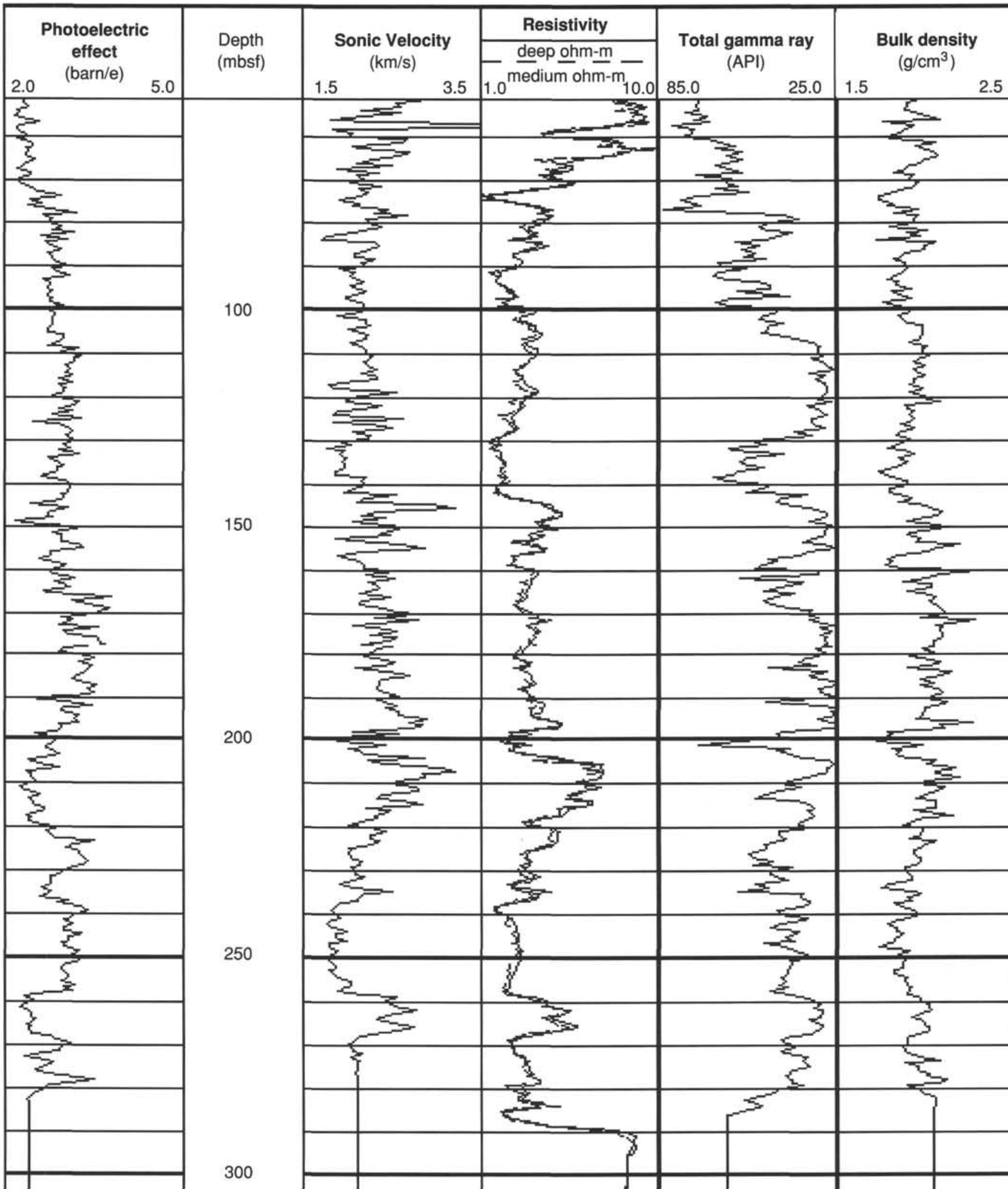

Figure 35. Selected downhole logs from the quad combination tool string for the interval 50.6 to 306.2 mbsf in Hole 800A: photoelectric effect, sonic velocity, resistivity, total gamma ray, and bulk density. Sonic velocity, resistivity, and density reflect the porosity of the formation and, therefore, the degree of lithification or cementation (e.g., chert vs. radiolarite).

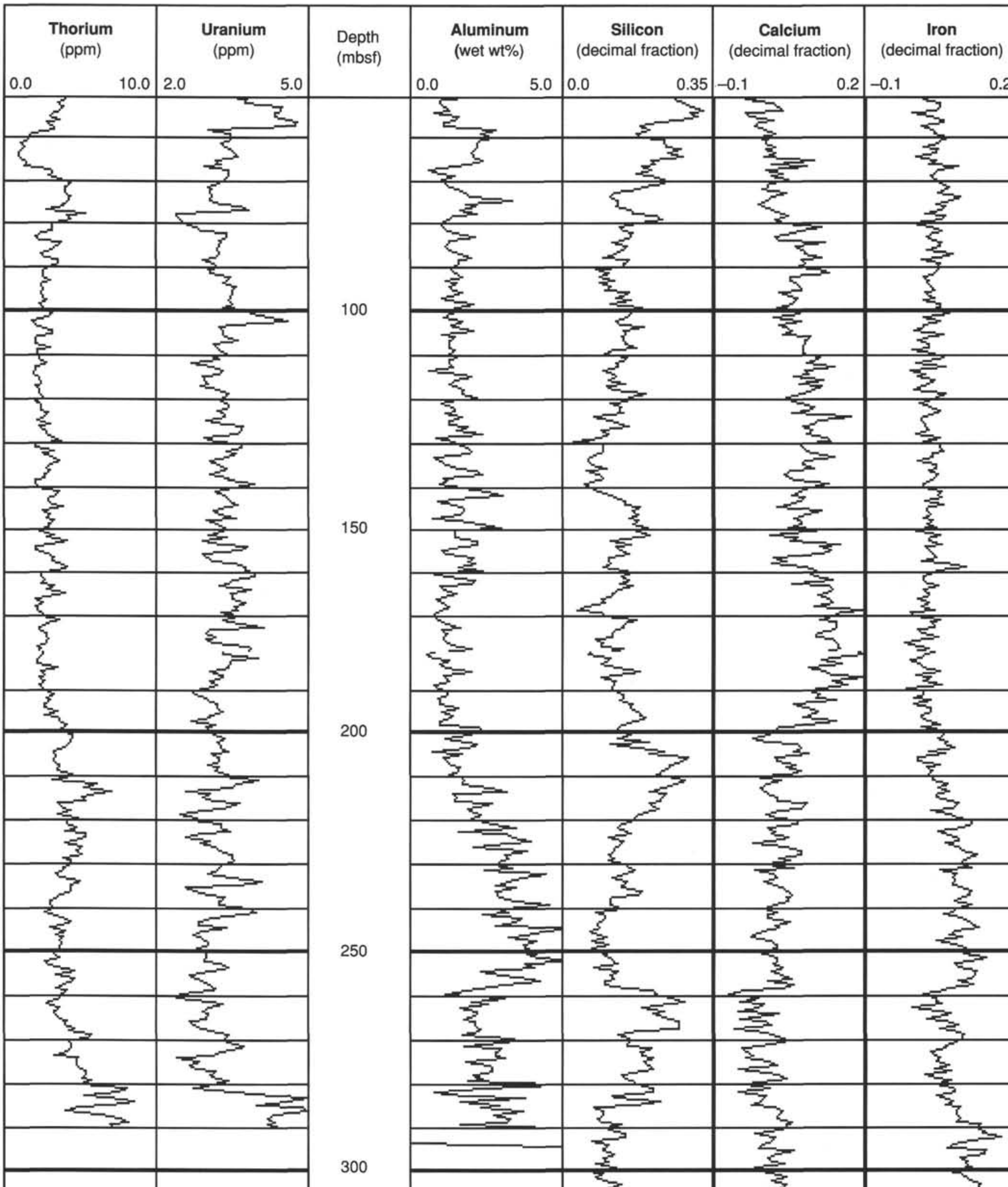

Figure 36. Selected downhole logs from the geochemical combination tool string for the interval from 50.6 to 306.2 mbsf in Hole 800A: thorium, uranium, aluminum, silicon, calcium, and iron. The relative abundances of these elements serve to identify the primary constituents that distinguish the major lithologies recovered at Hole 800A (e.g., biogenic silica and carbonate, pelagic clay, and volcanogenic material, including clay).

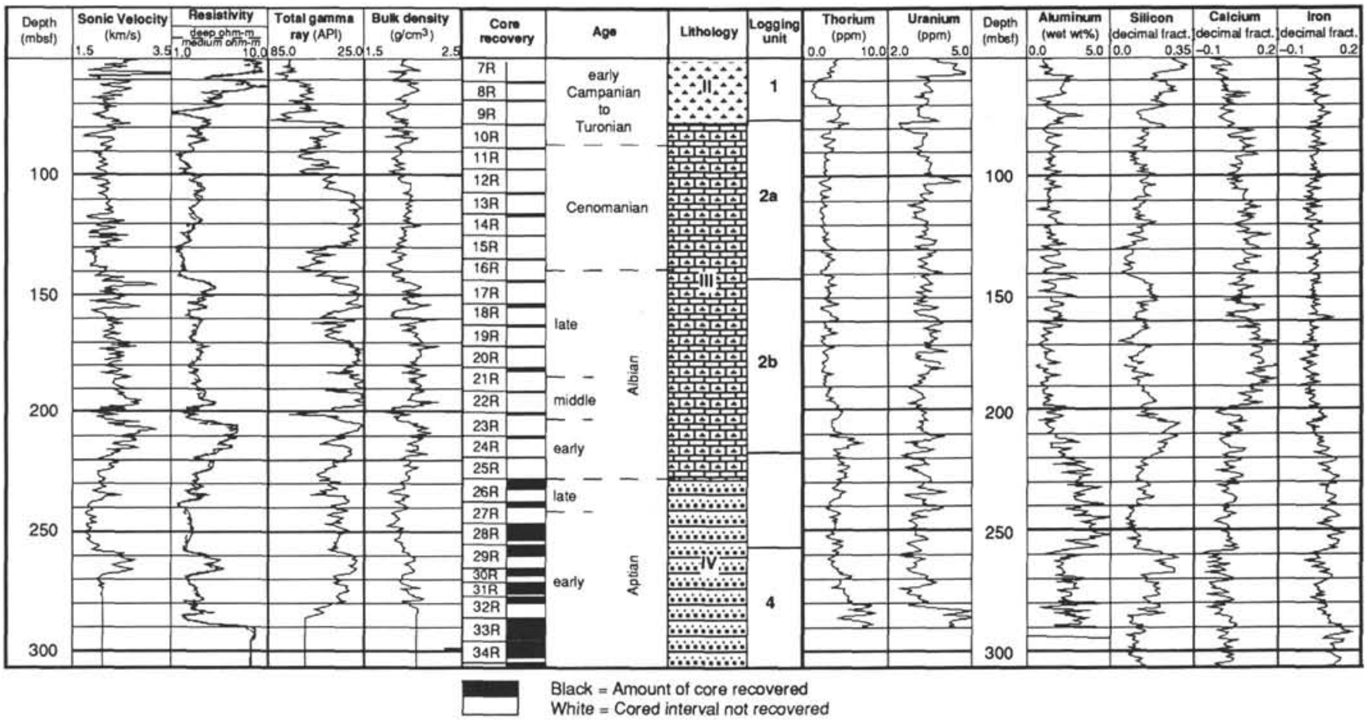

Figure 37. Summary compilation of downhole logs, intervals of core recovery, lithology, and downhole logging units at Hole 800A. Lithologic units are based on coring results (see ''Lithostratigraphy and Sedimentology'' section, this chapter).

This type of logging response corresponds well with the lithologies and trends observed for lithofacies Unit III (''Lithostratigraphy and Sedimentology'' section, this chapter), but the average formation velocity as well as the low resistivity and high total gamma-ray emphasize that less indurated, higher porosity, clay-rich intervals must make up the unrecovered majority of this section. The lower boundary of logging Unit 2a is again an inflection point created by a sinusoidal variation observed on several logs. The boundary is marked by local minima in velocity (1.9 km/s), resistivity (.5 ohm-m), density (1.75 g/cm^3) and silicon with a relative maximum in total gamma-ray (67 API) juxtaposed against maxima/minima for all these logs, including the introduction of a local maximum in calcium. This logging boundary occurs from 131 to 151 mbsf and may be interpreted as a change from a clay-rich chalk to a massive, silicified limestone bed at approximately 142 mbsf.

Logging Unit 2b (142–219 mbsf)

Logging Unit 2b is characterized by high velocities (2.1–3.1 km/s), resistivities (1.5–3.0 ohm-m), and densities (1.9–2.3 g/cm^3), and low gamma-ray (25 API). This logging unit is also distinguished by the highest calcium/silicon ratios obtained within the entire logged interval.

The logging response observed in Unit 2b indicates an overall decrease in clay content and increase in carbonate content compared to the overlying unit, with restricted zones that are clay-rich and carbonate-poor (e.g., at 157 mbsf). These results correspond well with the lithologic trends observed in the cores (lithologic Unit III). The lower boundary of logging Unit 2b is distinguished by another sinusoidal variation observed on all logs from 198 to 219 mbsf. The boundary is marked by local minima in velocity (1.7 km/s), resistivity (.5 ohm-m), density (1.7 g/cm^3), silicon, and calcium, and local maxima in total gamma-ray (73 API), iron, and aluminum immediately juxtaposed against maxima/minima in these logs, including an overall shift to lower calcium and higher silicon values. This logging response is probably due to a clay-rich interval of volcanic origin (high aluminum and iron, low silicon) overlying an interval with low clay content dominated by chert rather than silicified limestone. The bottom portion of this logging unit from 198 to 219 mbsf corresponds to the transitional zone at the base of lithofacies Unit III (''Lithostratigraphy and Sedimentology'' section, this chapter), where volcanogenic clays are interbedded with chert.

Logging Unit 3 (219–258 mbsf)

Logging Unit 3 is characterized by simultaneous trends of increasing aluminum and iron content and decreasing silicon content with depth along with an overall shift towards low calcium. This interval is also marked by decreasing velocity (2.2 to 1.7 km/s) and resistivity (5 to .5 ohm-m) with variable total gamma-ray counts.

Logging Unit 3 corresponds to lithologic Unit IV and illustrates the transition from nonvolcanogenic lithologies to a sequence dominated by volcanogenic material. The lower boundary of logging Unit 3 is marked by a sharp increase in velocity (1.9 to 2.7 km/s), resistivity (.5 to 3.5 ohm-m), and silicon content along with a sharp decrease in aluminum, iron, and total gamma-ray count. The lowest values of calcium observed in Hole 800A also begin at this level (near 258 mbsf). An interval dominated by chert or a silica-rich sand with a virtual absence of volcanogenic clays is inferred from the logging response that defines the base of Unit 3.

Logging Unit 4 (258–312 mbsf)

Logging Unit 4 begins at 258 mbsf and terminates at the TD for logging operations at Site 800. This unit is characterized by the lowest calcium values observed in Hole 800A, variable but elevated aluminum and iron content, and a trend toward a lower silicon content with depth. Logging Unit 4 also corre-

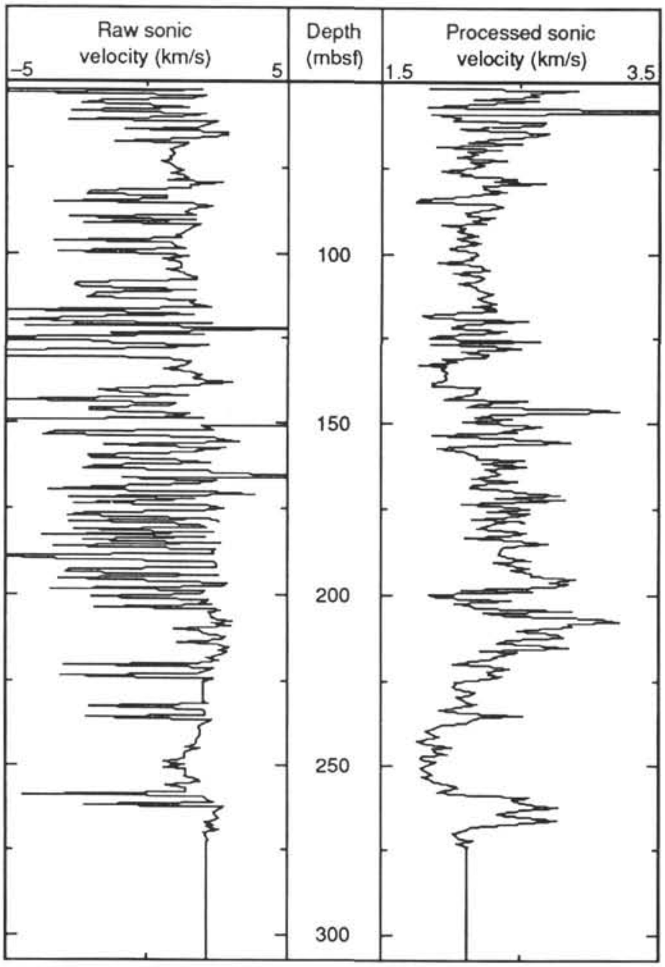

Figure 38. Comparison of observed "raw" and processed velocity logs for Hole 800A. The velocity spike (processed log) at 58 mbsf is an artifact. Covariation of the processed sonic log with resistivity, gamma ray, and bulk density logs (Fig. 35) indicates that a useful velocity log was produced.

sponds to lithofacies Unit IV and is interpreted as a zone dominated by volcanogenic material grading upward into a zone containing greater amounts of biogenic silica. A rapid change from high silicon to low silicon content is matched by the disappearance of radiolarians below approximately 285 mbsf (see "Biostratigraphy" section, this chapter).

Synthetic Seismogram

A synthetic seismogram was computed for Site 800 to accurately tie the drilled sequence in the hole to seismic reflection data over the site (Fig. 39). The seismogram covers the interval from 50.6 to 306.2 mbsf, approximately 7.576 to 7.804 s two-way traveltime (twt).

The unprocessed sonic velocity log at Hole 800A (Fig. 38) is dominated by very high and/or low values corresponding to cycle skipping, especially in the uppermost 175 mbsf. The sonic log-processing software aboard the *JOIDES Resolution* allowed us to set a window of possible velocity values and then recalculate a new log using only the traveltime data that result in velocities within the chosen window. We chose a minimum-maximum window of 1.69 to 5.1 km/s. The processed sonic log (Fig. 38) was used in combination with the raw-bulk density log to calculate reflection coefficients that were convolved with the source wavelet to produce a synthetic seismogram. The synthetic seismogram was shifted to the proper two-way traveltime on the seismic profile by matching the reflection created by the first chert encountered at this site. The synthetic seismogram (Fig. 39) is compared with the single-channel seismic (SCS) line shot on approach to Site 800. The major reflectors apparent on the synthetic seismogram are correlated with the seismic 10-trace mix and seismic reflection profile. Improved synthetic seismograms will be produced following shore-based processing, including incorporation of physical properties data, repicking of traveltimes and the use of improved source wavelets.

A few general interpretations of the rocks comprising a portion of the sedimentary section at Site 800 have been made by extrapolating the downhole logging results onto the seismic profile. A further description of the correlation between seismic stratigraphy and lithostratigraphy is given in the "Site Geophysics and Seismic Stratigraphy" section, this chapter (see Fig. 40).

Seismic Intervals

1. 7.512 to 7.572 s twt: This uppermost zone corresponds to lithofacies Unit I. The seismically transparent nature indicates a relatively homogenous interval with no significant impedance contrasts. The first reflector on the SCS profile is due to the impedance contrast at the sediment/water interface and is followed 24 ms later by another high-amplitude event that is part of the source wavelet and does not represent a separate impedance contrast. The thickness of this unit is most accurately determined with the 3.5-kHz profiler at 60 ms (see Fig. 41, "Site Geophysics and Seismic Stratigraphy" section, this chapter).
2. Logging Unit 1, 7.572 to 7.608 s twt (average velocity = 2.2 km/s): The sharp velocity/porosity contrasts of chert and interbedded, clay-rich zones of lithofacies Unit II create the two moderate-amplitude, flat-lying reflectors that bound lithofacies Unit II.
3. Logging Unit 2a, 7.608 to 7.664 s twt (average velocity = 2.29 km/s): This interval contains discontinuous, moderate-amplitude reflections and more continuous, high-amplitude events, both of which are the result of velocity-density contrasts between clay-rich zones and silicified limestone/chert-dominated intervals of lithofacies Unit III. A single, very high amplitude reflector observed on the synthetic seismogram at approximately 7.66 s twt is produced by a high-velocity/low-porosity interval at 142 mbsf, which is interpreted to be a zone of silicified limestone (see logging Units 2a to 2b). This reflector corresponds to a very low amplitude event on the 10-trace mix; however, the seismic reflection profile shows that this event varies dramatically in amplitude across Site 800, perhaps indicating lateral variation in silicification within this carbonate/clay sequence.
4. Logging Unit 2b, 7.664 to 7.716 s twt (average velocity = 2.96 km/s): This interval contains slightly higher amplitude and more continuous flat-lying reflections. The high carbonate, low clay content inferred for the unrecovered section of this interval from both logs and cores apparently creates a low-porosity matrix that results in the high-interval velocity.
5. Logging Units 3 and 4, 7.716 to 7.804 s twt (average velocity = 2.00 km/s): This interval is characterized by the highest amplitude and most continuous reflections observed within the logged interval. This sequence of flat-lying reflections corresponds to the volcanogenic turbidites of the upper portion of lithofacies Unit IV ("Lithostratigraphy and Sedimentology" section, this chapter). This section is dominated by volcanogenic silt and clay (low silicon/aluminum ratio), resulting in a low-interval velocity of 1.77 km/s interspersed with intervals of elevated silica (e.g., the boundary of logging Units 3 and 4).

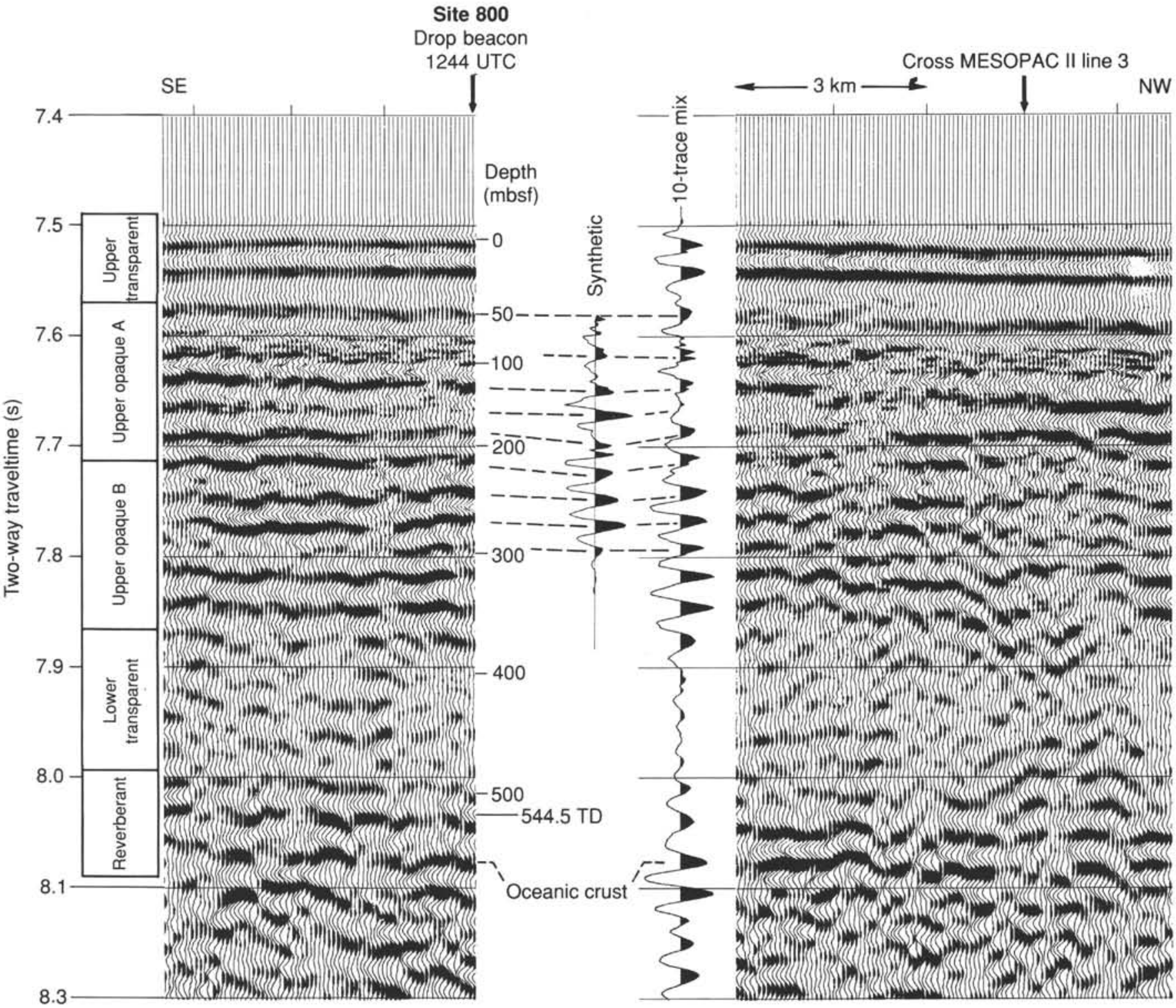

Figure 39. Comparison of vertical-incident SCS water-gun data recorded on approach to Site 800, with a 10-trace mix of this data centered over Hole 800A and a synthetic seismic reflection. This trace was computed from downhole velocity and density measurements and the far-field source wavelet produced by the two 80-in.^{3} water guns used during Leg 129. The following is a list of seismic processing and display parameters: mute, 3-trace mix, band-pass filter 25–250 Hz, and 500 ms AGC.

The synthetic seismogram, coupled with the geochemical logs, indicates that high-amplitude reflections are created by velocity/porosity contrasts associated with sharp changes in silicon content, and to a lesser degree, changes in calcium content, both at a larger scale than individual turbidite sequences. In other words, the seismic character of this interval is apparently produced by changes in porosity due to silicification along primary bedding structures observed within turbidites. This observation may explain the relatively transparent seismic character of the lowermost volcanic turbidite sequence, which is barren of both microfossils (the sources for excess silica and carbonate) and any dominant bedding structures ("Sedimentology and Lithostratigraphy" and "Biostratigraphy" sections, this chapter).

Summary

A suite of eight different downhole logs were successfully recorded at Site 800, resulting in the identification of five distinct logging units. Compositional trends and boundaries were inferred from these logs through intervals of poor recovery by assuming that unrecovered intervals are composed of varying proportions of recovered materials. The logs were most useful in defining boundaries and in characterizing the unrecovered majority of the formation.

The correlation of the synthetic seismogram with the observed seismic profile (along with geochemical logs) indicates that diagenetic horizons along primary bedding structures rather than the primary structures themselves create the large impedance contrasts that control the character of the seismic image.

SITE GEOPHYSICS AND SEISMIC STRATIGRAPHY

Site Geophysics

Site selection for Leg 129 was based on the multichannel seismic (MCS) surveys described in the "Explanatory Notes" chapter (this volume). Underway geophysical data were collected as we approached all sites. These data provided the

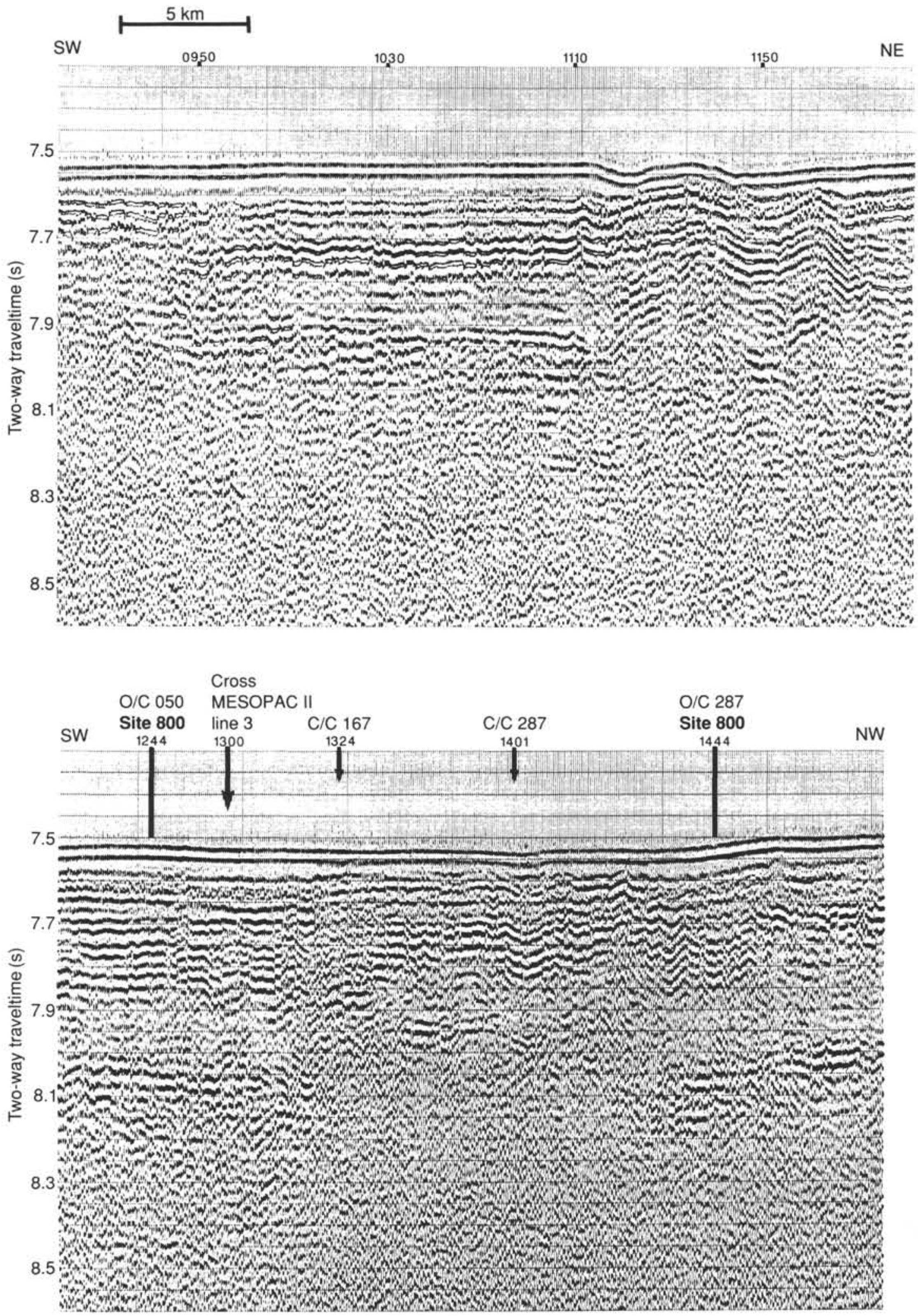

Figure 40. The entire SCS profile (two 80-in.^{3} water guns) obtained on approach to Site 800 (1244 hr UTC, 25 November 1989) during Leg 129. This SCS profile crosses MESOPAC II line 3 (see Fig. 43) at 1300 hr, where proposed site PIG-1 was originally located. This SCS profile recrosses Site 800 at 1444 hr on a nearly orthogonal path. High velocity basement (sills) and total depth at Site 800 lie at 8.004 and 8.024 s twt, respectively. The SCS data were processed and displayed with the following parameters: water velocity F/k migration, mute, 2-trace mix, band-pass filter 30–100 Hz, and 500 ms AGC. Vertical exaggeration is approximately 22× at 1.5 km/s.

correlations with principal MCS sections needed in order to position the ship at preferred locations.

Site 800 (proposed site PIG-1) in the northern Pigafetta Basin is located near the intersection of lines 1 and 3 of an MCS survey obtained during the MESOPAC II expedition aboard *Le Suroit* in August-September 1989. Because Leg 129 began less than 3 months after the *Le Suroit* cruise, only single-channel records of both water-gun and air-gun data, as well as sonobuoy refraction data, obtained during MESOPAC II were used to locate proposed site PIG-1. The site was specifically located at 0740 hr UTC 21 August 1989 along an air-gun (two 1000-in.^{3}) portion of MESOPAC II profile 3, which includes the area sampled by sonobuoy 2m (see Fig. 4 and "Background and Objectives" section, this chapter). The only other seismic data in the area are a few widely spaced, single-channel, air-gun analog profiles (e.g., C1205, V3312, V3214, and V3612).

SCS reflection and 3.5- and 12-kHz profiling were conducted during the approach of the *JOIDES Resolution* to Site 800 (see "Operations" section, this chapter, for detailed approach plan). The actual site is located on this SCS water-gun profile at 1244 hr UTC, 25 November 1989 (Fig. 40), approximately 3 km southwest of the intersection of Leg 129's SCS and MESOPAC II's line 3 (proposed site PIG-1 location).

The water-gun (two 80-in.^{3}) data collected by the *JOIDES Resolution* and the air-gun (two 1000 in.^{3}) data of MESOPAC II are corroborative and, together with 3.5-kHz data, provided the following seismic criteria for locating Site 800:

1. The relatively thick (60–65 ms), transparent layer over acoustic basement, imaged with an excellent 3.5-kHz record (Fig. 41), indicated that enough soft sediment was present over the first cherts to provide lateral support for the drill string during spud-in.
2. A high-amplitude reflection imaged at .50 to .55 s below seafloor (bsf) corresponds to the onset of velocities characteristic of oceanic crust as recorded on sonobuoy 2m (MESOPAC II), indicating that approximately 500 to 600 m of sediment overlie oceanic crust in this area.
3. This basement reflection shallows in areas surrounding the site and, therefore, this location offered a thicker, lower sediment section without putting basement out of reach of a single-bit hole.

Seismic Stratigraphy

The acoustic stratigraphy of large portions of the western Pacific consists of four units originally defined by Ewing et al., (1968): (1) an upper transparent layer, (2) an upper opaque layer, (3) a lower transparent layer, and (4) acoustic basement. These seismic facies descriptions were made from observations of SCS analog air-gun profiles. Acoustic basement has been characterized by the presence of a prominent zone of flat-lying ("smooth"), high-amplitude, closely spaced reflections referred to as "horizon B" by Ewing et al. (1968), the "deep opaque layer" by Heezen, et al. (1973), and as the "reverberant layer" by Houtz et al. (1970) and Houtz and Ludwig (1979). It is now recognized that the reverberant nature of acoustic basement in such profiles is usually the result of a trailing bubble pulse oscillation reflecting from a single, high-impedance boundary (Shipley et al., 1983). This characteristic of the air-gun source is now routinely compensated for through the use of tuned air-gun arrays and deconvolution techniques. The use of water guns in these surveys provides a much more implosive and bubble pulse-free source signature that provides a high-resolution record with little processing effort (Hutchinson and Detrick, 1984).

Although modern acquisition and processing techniques have allowed a more detailed and quantitative assessment of the stratigraphic units originally proposed by Ewing et al. (1968) (especially acoustic basement), these units can still serve to describe the general seismic character of the Pigafetta Basin.

The lowermost sequence, known as the "reverberant layer," is composed of closely spaced, high-amplitude, continuous reflections that directly overlie a less continuous, more diffractive surface. This sequence extends over a 100-ms interval from 492 ms to approximately 600 ms bsf (8–8.1 s twt) (Figs. 40, 42, and 43). Immediately overlying this interval is the "lower transparent" layer, which is characterized by low-amplitude, widely spaced, discontinuous reflections that extend from 372 to 492 ms bsf (7.884–8.004 s twt). This interval appears to thin to under 100 ms in thickness within 6 km to either side of Site 800 along the intersecting SCS profiles recorded during the approach (see 1210 hr and 1315 hr, Fig. 40). The deepening of basement resulting in this locally thickened, lower transparent sequence is also observed on MESOPAC II line 3, locating this site in a somewhat elongate structural basin. The lower transparent layer is bounded on top by another distinct sequence of closely spaced, moderate- to high-amplitude reflections that are traceable for over 50 km. This interval extends from 60 to 372 ms bsf (7.572–7.884 s twt) and is identified as the "upper opaque" sequence. The upper opaque zone can be divided into two units: (A) 60 to 204 ms bsf and (B) 204 to 372 ms bsf. The lower sequence, from 204 to 372 ms bsf (upper opaque B), is composed of parallel, continuous, high-amplitude reflections. The upper opaque zone, from 204 up to 60 ms bsf (upper opaque A), displays somewhat more discontinuous, lower amplitude reflections with the uppermost reflectors in the sequence exhibiting localized pinch-outs, in addition to a possible truncation of reflectors marking an unconformity between the upper opaque and upper transparent sequences.

The "upper transparent zone" as envisioned by Ewing et al. (1968) is very much attenuated in the Pigafetta Basin and extends from 0 to approximately 60 ms bsf (7.512–7.572 s twt) at Site 800. This interval is best displayed on the 3.5-kHz record obtained during Leg 129 (Fig. 41) and during MESOPAC II, but is also apparent on SCS records. These four seismic facies are essentially identical on the SCS of both Leg 129 and MESOPAC II.

Correlation between Seismic Stratigraphy and Lithology at Site 800

Figure 42 summarizes the seismic reflection record and correlates this record with lithologic and logging observations and measurements obtained at Site 800.

The lithofacies significance of the "reverberant layer" or "acoustic basement" had never been determined for the Pigafetta Basin before Leg 129. Houtz and Ludwig (1979) completed an extensive review of the areal extent, thickness, and velocity of this seismic facies and demonstrated that the reverberant layer in the Pacific can be produced by the impedance contrasts between sediments and volcanic sills or flows (e.g., DSDP Site 462 in the Nauru Basin), by volcanogenic turbidites (e.g., DSDP Site 585 in the East Mariana Basin) and, in some cases, the sediment oceanic crust in areas of particularly smooth crust. A firm understanding of seismic source and display characteristics is necessary to interpret a zone of closely spaced reflections as the result of multiple impedance contrasts (true layering) or simply a single, high-impedance boundary. The physical significance of the reverberant layer, and therefore its utility as a seismic-stratigraphic

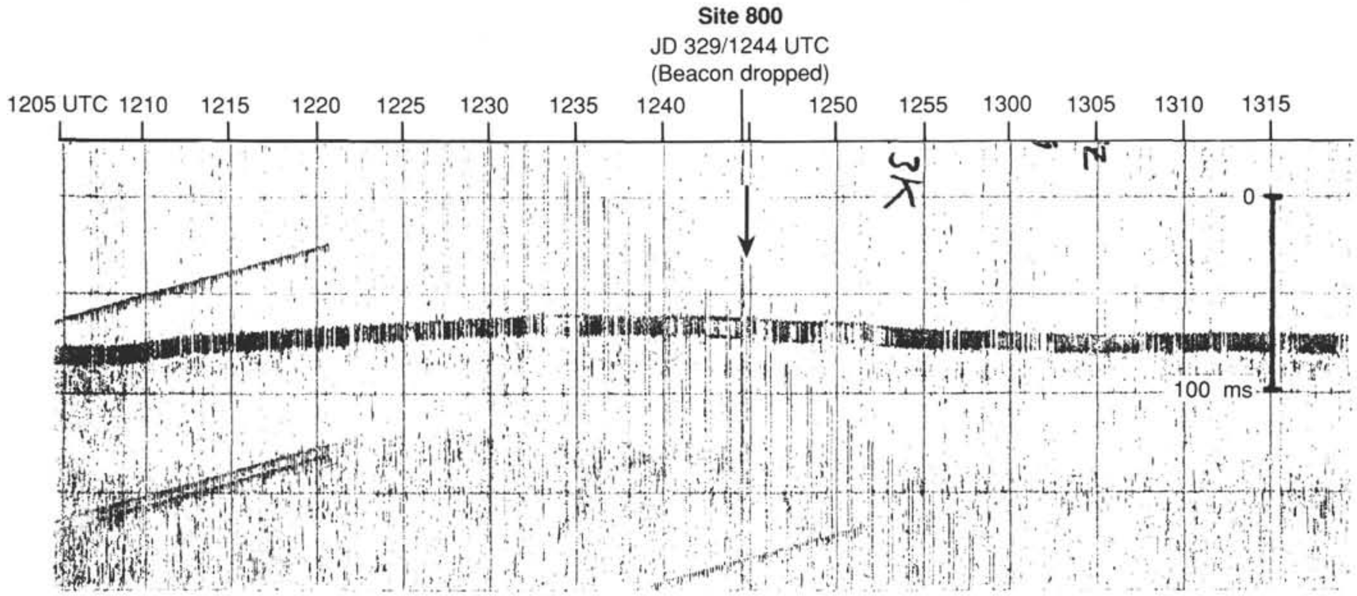

Figure 41. The 3.5-kHz record collected on approach to Site 800 (beacon drop) during Leg 129. Acoustic basement on this record marks the top of the first chert and indicates 0 to 65 ms of pelagic clay. This record displays a slightly thicker transparent layer than that observed on SCS profiles. The 60 ms reported for the thickness of the upper transparent seismic facies was measured from an enlarged 10-trace mix of the SCS record.

correlation unit, can now be better determined (Shipley et al., 1983).

The reverberant layer at Site 800 is created by a massive chert overlying a series of dolerite sills (see "Igneous Petrology" section, this chapter). The physical nature of these closely spaced reflections is primarily due to source characteristics and not on any real layering. This seismic facies is interpreted to result primarily from a single-impedance contrast between the radiolarite clays and the top of chert overlying dolerite sills at 498 mbsf. However, a second impedance contrast at 552 ms bsf (8.07–8.1 s twt) apparently creates a more diffractive reflection, which is interpreted as the top of oceanic crust. The top of the massive chert creates a very uniform, smooth reflecting surface and the high-velocity material directly overlying basement acts to reduce basement relief on time-section displays. This type of smooth, flat-lying, high-velocity horizon is characteristic of much of the Pigafetta Basin and the majority of the East Mariana Basin (Abrams et al., 1988). The deeper diffractive reflection marks the top of a rougher, less uniform surface interpreted as the top of oceanic crust. If this diffractive reflection does represent the top of oceanic crust, some lower velocity material must exist between it and the dolerite sills. An estimate of 133 m for the maximum thickness of sills over basement has been made by assuming the dolerite sills extend all the way to this reflection with a constant velocity of 4.46 km/s (see "Physical Properties" section, this chapter). Sonobuoy data correctly indicated that high velocities (4.8 km/s) begin at the clay/dolerite sill interface but were unable to resolve the differences in velocity and velocity gradients that could distinguish normal oceanic crust from oceanic crust with such a thin overburden of igneous material.

The lower transparent layer correlates with the thin (48.5 m) pelagic sequence of clay and radiolarite sand and the poorly bedded brecciated debris flows between 498 and 343 mbsf (see "Lithostratigraphy and Sedimentology" section, this chapter). This interval is also characterized by an absence of radiolarians and nannofossils. The discontinuous, widely spaced, low-amplitude reflections in this interval indicate that no large, laterally continuous impedance contrasts are present, and it is inferred that the lack of diagenetic or well-cemented horizons focused along well-developed bedding structures is responsible for the seismically transparent nature of this layer.

The transition from brecciated, poorly bedded debris flows to coarse-grained, bedded turbidites, along with the appearance of nannofossils at approximately 343 mbsf, correlates to a change from lower transparent to upper opaque seismic facies. The lowermost section of the opaque zone (upper opaque B), which is characterized by the highest amplitude, most continuous reflections, changes to lower amplitude, continuous to more discontinuous events upsection within the upper opaque A zone. The subtle change in seismic character that divides the upper opaque seismic facies is clearly correlated to the transition from redeposited volcanogenic material with intervals of high silicon content (about 219 to 300 mbsf) to a sequence of pelagic carbonate and silica-rich sediments (between 78 and 219 mbsf). The most discontinuous, diffuse reflections are associated with the clay/porcellanite/chert sequence between 38 and 78 mbsf.

The transparent nature of the uppermost 60 ms (upper transparent layer) indicates a relatively homogenous interval containing no significant impedance contrasts and is correlated to pelagic brown clay (0–38 mbsf).

The correlation of seismic facies with lithofacies is most strongly constrained within the interval logged at Site 800, which lies entirely within the upper opaque layer. It is apparent from correlations with the synthetic seismogram (Fig. 43) that high-amplitude reflections are associated with intervals of elevated silica content, high velocity, resistivity, and density, and low total gamma-ray count (see "Downhole Measurements" section, this chapter). The reflection events in this interval (50–307 mbsf) are interpreted to be caused by impedance contrasts created by diagenetic or well-cemented horizons interbedded with clay- and chalk-dominated intervals. Reflections are highest in amplitude and most contin-

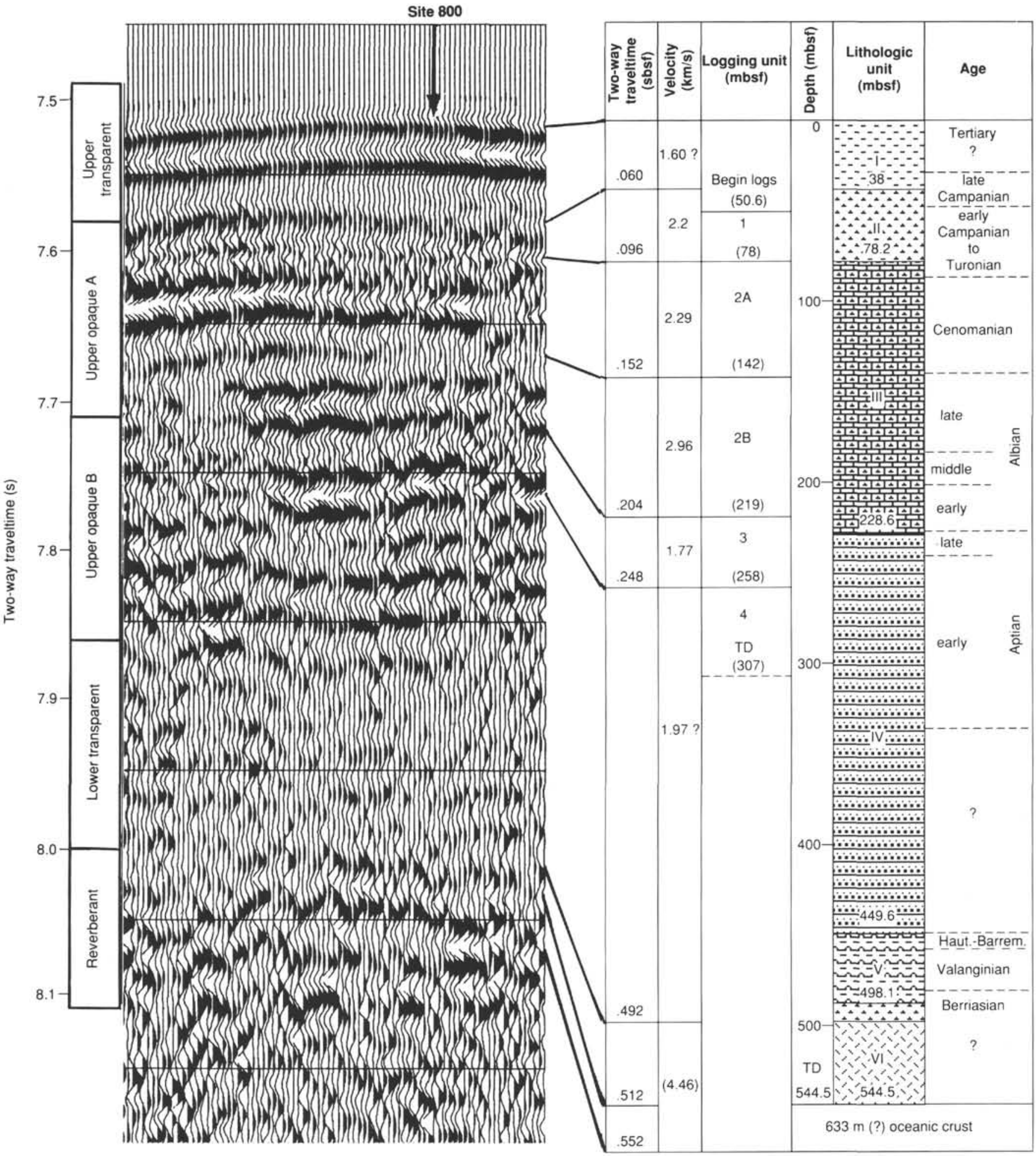

Figure 42. Summary of seismic stratigraphy at Site 800 showing correlations with logging units, ages, and depths. These correlations should only be considered as best estimates until further constraints are provided by improved synthetic seismograms (see Fig. 39). The velocity calculated for lithologic Unit I, assuming that the first sub-seafloor reflection at 60 ms bsf is the first chert at 38 mbsf, is 1.27 km/s. A more reasonable velocity of 1.6 km/s is assumed, resulting in a thickness of 48 m of pelagic clay (Unit I). The 10-m discrepancy in thickness derived from drill-string length vs. that predicted by the 3.5-kHz record is discussed in the "Operations" section, "Site 801" chapter. The 2.2-km/s velocity corresponds to the interval 38 to 78 mbsf. The 4.46-km/s velocity given for the dolerite sills is an average from physical properties measurements. This SCS water-gun record is displayed with a vertical exaggeration of 33× at 1.5 km/s with the same parameters described in Figure 40.

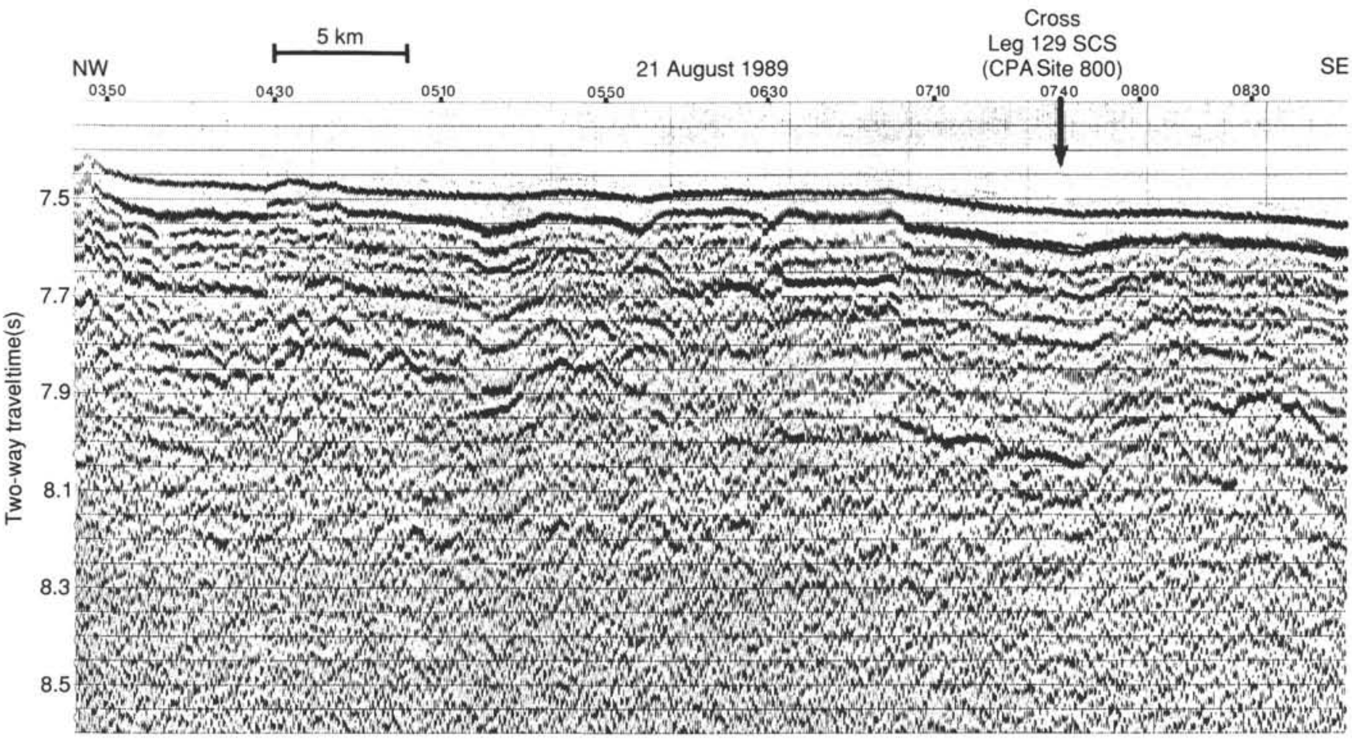

Figure 43. MESOPAC II line 3 SCS record (two 1000-in.^{3} air guns) showing intersection with the SCS approach profile collected during Leg 129, 3 km northeast of Site 800. Sonobuoy 2m was recorded along this profile from 0349 to 0800 hr UTC and indicates that high-velocity basement begins at 8.025–8.050 s twt at the closest point of approach (CPA) to Site 800. The relief of the basement reflection along this flow-line profile indicates that original abyssal hill morphology is not completely muted by thick sequences of sills or flows. This near-channel record was processed and displayed with the following parameters: shot edit, mute, predictive deconvolution, band-pass filter 8–40 Hz, and 500 ms AGC. Vertical exaggeration is approximately 25× at 1.5 km/s.

uous within the well-developed, graded turbidite beds between 228 and 343 mbsf and become lower in amplitude and more variable in continuity within the pelagic carbonate-silica interval between 38 and 228 mbsf. These observations indicate that within the fine-grained, thinly bedded turbidites, redeposited silica can be focused along well-developed bedding structures creating continuous, high-amplitude reflections, and alternatively, that silica redeposition is less focused, creating more diffuse reflecting horizons in the intervals of less robust bedding structure above. Within the logged interval the common factor for creating reflections is low porosity associated with excess silica. Unfortunately, the logged interval at Site 800 did not reach significantly below the fine-grained, thinly bedded turbidites that extend to 278 mbsf, and so we cannot determine if the continuous reflections below this interval are due solely to primary structure of the coarser grained, thicker turbidite beds interbedded with less indurated clay/claystone, or if excess silica also plays a role in the creation of these reflectors.

SUMMARY AND CONCLUSIONS

Introduction (Jurassic Hopes and Cretaceous Fears)

The first site drilled on Leg 129 was considered an important test of our hypothesis that Jurassic crust and sediment were within reach in the Pigafetta Basin. The results of this single-bit pilot hole were to set the pace for the rest of the leg. If Jurassic rocks were indeed present at this site, located in an area where magnetic anomaly identification was indisputable, we were confident that we would be able to find even older rocks at the next site, within the Jurassic quiet zone. The section was thin enough to be cored quickly and we expected to reach the top of the Mesozoic within a few tens of meters of penetration. Below that level, if Upper Cretaceous cherts would not hamper operations too much, drilling through the entire sediment section was only a matter of a few days. The image of the basement on the seismic profiles was certainly not as clear as we would have liked for a first attempt, but other conditions were so encouraging that we were optimistic about the outcome.

The upper part of the section corresponds exactly to what we expected to find: equatorial cherts of Late Cretaceous age overlying Albian pelagic sediments. The composition of these sediments, partly silicified but still calcareous, yielded relatively good biostratigraphic control and their moderate rates of accumulation were an indication that most of the Mesozoic section that we had hoped for was indeed present at this site. The first cores recovered that contained some redeposited volcaniclastics of Aptian age were not really a surprise because a large seamount of that age (Himu) was only some tens of miles away. The shallow-water nature of these sediments indicates that they are more probably derived from Golden Dragon Guyot about 100 miles to the southeast, or from a larger, unnamed guyot slightly farther away to the northeast. Recovering more of the same facies core after core was not really alarming since we were steadily getting back in time, and reaching the lower Aptian told us that we could be out of the volcanogenic deposits soon. Basement was getting closer with each core, however, and volcaniclastics were also becoming coarser grained toward the base of the section, indicating higher rates of sedimentation that began to cloud our optimistic predictions. Relief came with siliceous claystones and radiolarites of Hauterivian-Barremian age. It looked as if we had seen most of the ever-feared middle Cretaceous sediments and were again in pelagic deposits well down into the Lower Cretaceous. Within a few tens of meters, however, medium-grained dolerites were encountered. Before we even had a confirmation of the age of the overlying sediments we knew that we had not reached the Jurassic crust. The igneous rocks were clearly intrusive and soon we learned that the oldest sediments were of Berriasian age and that we had just missed the Jurassic.

Although the main objective for this site was not achieved, drilling at Site 800 nevertheless yielded interesting results pertaining to the Mesozoic evolution of the western Pacific. These results mostly concern the history of the middle Cretaceous volcanic events and the motion of the Pacific plate since the earliest Cretaceous. In addition this site provided enough background information to better understand the geophysical characteristics of the Pigafetta Basin and plan our strategy for the remainder of the cruise.

Basement Problems

We are convinced that the lowermost layers cored at this site do not represent the oceanic crust. They consist of dolerites of a clearly intrusive nature, injected in sediments that post-date the magnetic anomalies. We believe that the true basement corresponding to the top of the oceanic crust cannot be very far below the top of the dolerite sills because the flat acoustic basement observed in the area lies at a depth of 8.05 s twt. This depth is compatible with the theoretical depth of Upper Jurassic crust, so that a thick accumulation of volcanic rocks or sediments sandwiched between the sills and the top of the oceanic crust is unlikely. Because the oldest sediment reached at this site is of earliest Cretaceous age (Berriasian), an age that predates all of the volcanic events recorded in the Nauru Basin, as well as on the numerous seamounts dredged in the western Pacific, it is likely that the intrusives here could be related to, and contemporaneous with, these events. The actual age and exact depth of the oceanic basement at Site 800 remain a mystery, but it appears probable, in hindsight, after having reached the Jurassic crust at Site 801, 290 nm to the southeast, that Site 800 is indeed underlain by crust of Oxfordian age, as predicted from the magnetic anomalies and basement depth.

Cretaceous Volcanic Events

Hard rock and sediments recovered at this site document a major pulse of volcanic activity during the Cretaceous. The igneous intrusives are probably related to that activity, although their age remains unknown until it is determined by radiometric methods. The sediments have also recorded that pulse in a series of thick, redeposited, volcaniclastic turbidites that account for about half of the section cored at this site. These sediments attest to the construction of volcanic edifices that must have reached close to the sea surface some time during the Aptian. The lower part of the turbidite interval is poorly dated, but the first sequences were deposited on top of Hauterivian-Barremian pelagic sediments. The sedimentary structures observed in this interval seem to indicate that the rate of sedimentation, or at least the distance from the sources of the redeposited material has decreased steadily with time. Most, if not all, of the volcanic "pulse" coincides with the entire Aptian stage. This site has again documented in detail what appears to be one of the dominant geological features of the western Pacific: widespread, vigorous volcanic activity during the Aptian. It is expressed here in the construction of volcanic edifices large enough to have reached close to the surface, or even to have been emergent at times, and it is possible that the intrusives found at the base of Hole 800A correspond to the same event. In any case, these two distinct expressions of intraplate volcanism are now documented over an area covering several millions of square kilometers.

History of Plate Motion

Site 800 provides a new set of data which, when combined with results from the other sites drilled during Leg 129, should be very useful for the study of the motion of the Pacific plate during the Mesozoic. An estimate of the successive paleolatitudes of the site was obtained from paleomagnetic data, and the distribution of various sediment facies in time provides additional independent clues for the determination of the time at which the site crossed the equator.

The reconstruction of the history of Pacific plate motion has been attempted through various models relying on different sets of references such as hotspot traces, paleolatitude estimates from seamounts or magnetic anomalies, sediment record of equatorial crossings, and combinations of these approaches. Despite discrepancies between the different models, the general trend of the history of plate motion is relatively well established for the period ranging from the Late Cretaceous to the Holocene. The older record, however, is still subject to major uncertainties. The few sites that have reached Lower Cretaceous sediments have provided enough information to indicate that the Pacific plate motion had a major northward component since at least as early as the Valanginian (Lancelot and Larson, 1975; Lancelot, 1978). Larson and Lowrie (1975) suggested that during at least the earliest Cretaceous and possibly the Late Jurassic, the plate moved from north to south so that it may actually have crossed the equator twice.

Paleomagnetic data from Site 800 confirm that the motion of the Pacific plate had a monotonic northward component at least from the early Aptian through the Cenomanian, and that indeed the plate moved from north to south prior to that time. The shift from southward to northward motion appears to have occurred between the Hauterivian-Barremian and the early Aptian. These findings show a good agreement with the biogenic component of the sediment record. The time when the site was in the vicinity of the high-productivity, equatorial zone is well documented by a relative increase in the abundance of silica of biogenic origin in the sediments. This increase is recorded by a peak in the abundance of radiolarians, the presence of chert, and the amount of silicon detected by the geochemical logging tool. Carbonate sedimentation exhibits trends that supplement the information provided by silica. Calcareous nannofossils show a marked increase in quantity from the late Aptian through the Cenomanian. The combined influences of the production of carbonate in the surface waters and the dissolution at depth will have to be studied in more detail before a model of equatorial CCD evolution for this period can be established. The older equatorial crossing has not been documented at this site by paleolatitude estimates from paleomagnetic measurements because the core samples from the older sediments recovered near the base of the hole were not judged entirely suitable for shipboard analysis. The silica content of the sediment, however, indicates that Site 800 was close to the equator during Berriasian-Valanginian times.

REFERENCES

Abrams, L. J., Larson, R. L., Shipley, T., and Lancelot, Y., 1988. Cretaceous volcanic sequences and Jurassic(?) crust in the western Pacific. *Trans. Am. Geophys. Union*, 69:1442.

Baumgartner, P. O., 1984. A middle Jurassic-Early Cretaceous low-latitude radiolarian zonation based on Unitary Associations and age of Tethyan radiolarites. *Eclogae Geol. Helv.*, 77:729–837.

Baumgartner, P. O., 1987. Age and genesis of Tethyan Jurassic Radiolarites. *Eclogae Geol. Helv.*, 80:831–879.

Berger, A., Imbrie, J., Hays, J., Kukla, G., and Saltzman, B., 1984. *Milankovitch and Climate* (Pt. 1): NATO ASI Ser., Ser. C, 126.

Cande, S. C., Larson, R. L., and LaBrecque, J. L., 1978. Magnetic lineations in the western Pacific Jurassic Quiet Zone. *Earth Planet. Sci. Lett.*, 41:433–440.

Christensen, N. L., and Salisbury, M. H., 1975. Structure and constitution of the lower oceanic crust. *Rev. Geophys. Space Phys.*, 13:57–86.

Detrick, R., Honnorez, J., Bryan, W. B., Juteau, T., et al., 1988. *Proc. ODP, Init. Repts.*, 106/109: College Station, TX (Ocean Drilling Program).

Ewing, J., Ewing, M., Aitken, T., and Ludwig, W. J., 1968. North Pacific sediment layers measured by seismic profiling. *In* Drake, C. L., and Hart, P. J. (Eds.), *The Crust and Upper Mantle of the Pacific Area.* Am. Geophys. Union. Monogr., 12:147–173.

Ferry, S., and Schaaf, A., 1982. Early Cretaceous environment at Deep Sea Drilling Project Site 463 (Mid Pacific Mountains) with reference to the Vocontian Trough (French Subalpine Ranges). *In* Thiede, J., Vallier, T. L., et al., *Init. Repts. DSDP*, 62: Washington (U. S. Govt. Printing Office), 669–682.

Fertl, H. H., 1979. *Gamma Ray Spectral Data Assists in Complex Formation Evaluation:* Houston (Dresser-Atlas).

Garrison, E. D., 1974. Radiolarian cherts, pelagic limestones and igneous rocks in eugeosynclinal assemblages. *In* Hsü, K. J., and Jenkyns, H. C. (Eds.), *Pelagic Sediments on Land and Under the Sea.* Spec. Publ. Int. Assoc. Sedimentol., 1:367–399.

Geroch, S., and Nowak, W., 1983. Proposal of zonation for the late Tithonian-Late Eocene, based upon arenaceous foraminifera from the Outer Carpathians, Poland. *In* Oertli, H. J. (Ed.), *Benthos '83:* 2nd Int. Symp. on Benthic Foraminifera (Pau), 225–239.

Gieskes, J. M., 1976. Interstitial water studies, Leg 33. *In* Schlanger, S. O., Jackson, E. D., et al., *Init. Repts. DSDP*, 33: Washington (U.S. Govt. Printing Office), 563–570.

Gieskes, J. M., and Johnson, J., 1981. Interstitial water studies, Leg 61. *In* Larson, R. L., Schlanger, S. O., et al., *Init. Repts. DSDP*, 61: Washington (U.S. Govt. Printing Office), 603–605.

Gradstein, F. M., and Sheridan, R. E., 1983. On the Jurassic Atlantic Ocean and a synthesis of results of DSDP Leg 76. *In* Sheridan, R. E., Gradstein, F. M., et al., *Init. Repts. DSDP*, 76: Washington (U.S. Govt. Printing Office), 913–943.

Haggerty, J. A., and Premoli-Silva, I., 1986. Ooids and shallow-water debris in Aptian-Albian sediments from the East Mariana Basin, Deep Sea Drilling Project Site 585: implications for the environment of formation of ooids. *In* Moberly, R., Schlanger, S. O., et al., *Init. Repts. DSDP*, 89: Washington (U.S. Govt. Printing Office), 399–412.

Hamilton, E. L., 1974. Prediction of deep-sea sediment properties: state of the art. *In* Inderbitzen, A. L. (Ed.), *Deep-Sea Sediments: Physical and Mechanical Properties:* New York (Plenum), 1–44.

———, 1978. Sound velocity-density relations in sea-floor sediments and rocks. *J. Acoust. Soc. Am.*, 63:366–377.

Handschumacher, D. W., and Gettrust, J. F., 1985. Mixed polarity model for the Jurassic "Quiet Zones": new oceanic evidence of frequent pre-M25 reversals. *Eos*, 66:867.

Handschumacher, D. W., and Kroenke, L., 1978. An extended time scale of Mesozoic geomagnetic reversals. *Eos*, 59:266.

Handschumacher, D. W., Sager, W. W., Hilde, T.W.C., and Bracey, D. R., 1988. Pre Cretaceous tectonic evolution of the Pacific Plate and extension of the geomagnetic polarity reversal time scale with implications for the origin of the Jurassic "Quiet Zone." *Tectonophysics*, 155:365–380.

Harland, W. B., Cox, A. V., Llewellyn, P. G., Pickton, C.A.G., Smith, D. G., and Walters, R., 1982. *A Geologic Time Scale:* Cambridge (Cambridge Univ. Press).

Hay, W. W., 1988. Paleoceanography: a review for the GSA Centennial. *Geol. Soc. Am. Bull.*, 100:1934–1956.

Heezen, B. C., MacGregor, I. D., and DSDP Leg 20 Scientific Party, 1973. Mesozoic chalks beneath the Caroline abyssal plain: DSDP Site 199. *In* Heezen, B. C., MacGregor, I. D., et al., *Init. Repts. DSDP*, 20: Washington (U.S. Govt Printing Office), 65–85.

Hilde, T.W.C., 1973. Mesozoic seafloor spreading in the North Pacific [D.Sc. thesis]. Univ. of Tokyo, Tokyo, Japan.

Hilde, T.W.C., Isezaki, N., and Wageman, J. M., 1976. Mesozoic seafloor spreading in the North Pacific. *In* Sutton, G. H., Manghnani, M. H., and Moberly, R. (Eds.), *The Geophysics of the Pacific Ocean Basin and its Margins.* AGU Geophys. Monogr. Ser., 19:205–226.

Hilde, T.W.C., Uyeda, S., and Kroenke, L., 1977. Evolution of the western Pacific and its margins. *Tectonophysics*, 38:145–166.

Houtz, R. E., Ewing, J., and Buhl, P., 1970. Seismic data from sonobuoy stations in the northern and equatorial Pacific, *J. Geophys. Res.*, 75:5093–5111.

Houtz, R. E., and Ludwig, W. J., 1979. Distribution of reverberant subbottom layers in the southwest Pacific Basin. *J. Geophys. Res.*, 84:3497–3504.

Hutchinson, D. R., and Detrick, R. S., 1984. Water gun vs. air gun: a comparison. *Mar. Geophys. Res.*, 6:295–310.

Hyndman, R. D., Christensen, N. I., and Drury, M. J., 1984. The physical properties of basalt core samples from Deep Sea Drilling Project Leg 78B, Hole 395A. *In* Hyndman, R. D., Salisbury, M. H., et al., *Init. Repts. DSDP*, 78B: Washington (U.S. Govt. Printing Office), 801–810.

Jackson E. D., Koizumi, I., et al., 1980. *Init. Repts. DSDP*, 55: Washington (U.S. Govt. Printing Office).

Jenkyns, H. C., 1978. Pelagic environments. *In* Reading, H. G. (Ed.), *Sedimentary Environments and Facies:* Oxford (Blackwell), 314–370.

Jenkyns, H. C., and Winterer, E. L., 1982. Palaeoceanography of Mesozoic ribbon radiolarites. *Earth Planet. Sci. Lett.*, 60:351–375.

Kaminski, M. A., Gradstein, F. M., Berggren, W. A., Geroch, S., and Beckmann, J. P., 1988a. Agglutinated foraminiferal assemblages from Trinidad. Taxonomy, stratigraphy and paleobathymetry. *Abh. Geol. Bundensanst. Austria*, 41:155–227.

Kaminski, M. A., Grassle, J. F., and Whitlatch, R. B., 1988b. Life history and recolonization among agglutinated foraminifera in the Panama Basin. *Abh. Geol. Bundensanst. Austria*, 41:229–243.

Karpoff, A. M., 1989. Les faciès pélagiques condensés cénozoiques des océans Pacifique et Atlantique: témoins des grandes crises géodynamiques [Thèse Doc. ès Sci.], Univ. Louis Pasteur, Strasbourg.

Kastner, M., Keene, J. B., and Gieskes, J. M., 1977. Diagenesis of siliceous oozes. I. Chemical controls on rate of opal-A to opal-CT transformation - an experimental study. *Geochim. Cosmochim. Acta*, 41:1041–1059.

Kent, D. V., and Gradstein, F. M., 1985. A Cretaceous and Jurassic geochronology. *Geol. Soc. Am. Bull.*, 96:1419–1427.

Kono, M., 1980. Statistics of paleomagnetic inclination data. *J. Geophys. Res.*, 85:3878–3882.

Krasheninnikov, V. A., 1971. Cretaceous benthonic foraminifera: DSDP Leg 20. *In* Heezen, B. C., MacGregor, I. D., et al, *Init. Repts. DSDP*, 20: Washington (U.S. Govt. Printing Office), 205–213.

Lancelot, Y., 1973. Chert and silica diagenesis in sediments from the central Pacific. *In* Winterer, E. L., Ewing, J. I., et al. *Init. Repts. DSDP*, 17: Washington (U.S. Govt. Printing Office), 377–405.

———, 1978. Evolution sedimentaire et tectonique de la plaque Pacifique. *Mem. Soc. Geol. France*, Nelle Ser., 134.

Lancelot, Y., and Larson, R. L., 1975. Sedimentary and tectonic evolution of the northwestern Pacific. *In* Larson, R. L., Moberly, R., et al., *Init. Repts. DSDP*, 32: Washington (U.S. Govt. Printing Office), 945–957.

Larson, R. L., and Chase, C. G., 1972. Late Mesozoic evolution of the western Pacific Ocean. *Geol. Soc. Am. Bull.*, 83:3627–3644.

Larson, R. L., and Hilde, T.W.C., 1975. A revised time scale of magnetic reversals for the Early Cretaceous and Late Jurassic. *J. Geophys. Res.*, 80:2586–2594.

Larson, R. L., and Lowrie, W., 1975. Paleomagnetic evidence for motion of the Pacific plate from Leg 32 basalts and magneticanomalies. *In* Larson, R. L., and Moberly, R., et al., *Init. Repts. DSDP*, 32: Washington (U.S. Govt. Printing Office), 571–577.

Larson, R. L., and Schlanger, S. E., 1981. Geological evolution of the Nauru Basin, and regional implications. *In* Larson, R. L., Schlanger, S. E., et al., *Init. Repts. DSDP,* 61: Washington (U.S. Govt. Printing Office), 841–862.

Larson, R. L., Pitman, W. C., Golovchenko, X., Cande, S. C., Dewey, J. F., Haxby, W. F., and LaBrecque, J. L., 1985. *The Bedrock Geology of the World:* New York (W. H. Freeman).

Manivit, H., Perch-Nielsen, K., Prins, B., and Verbeek, J. W., 1977. Mid Cretaceous calcareous nannofossil biostratigraphy. *Proc. K. Ned. Akad. Wet., Ser. B: Palaeontol., Geol., Phys., Chem.,* 8:169–191.

McKenzie, J. A., Bernoulli, D., and Schlanger, S. O., 1980. Shallow-water carbonate sediments from the Emperor Seamounts: their diagenesis and paleogeographic significance. *In* Jackson, E. D., Koizumi, I., et al., *Init. Repts. DSDP,* 55: Washington (U.S. Govt. Printing Office), 415–455.

Miura, Y., Rucklidge, J. C., and Nord, G. L., Jr., 1981. The occurrence of chlorine in serpentine minerals. *Contrib. Miner. Petrol.,* 76:17–23.

Moberly, R., Schlanger, S. O., et al., 1986. *Init. Repts. DSDP,* 89: Washington (U.S. Govt. Printing Office).

Nakanashi, M., Tamaki, K., and Kobayashi, K., 1989. Mesozoic magnetic anomaly lineations and seafloor spreading history of the northwestern Pacific. *J. Geophys. Res.,* 94:15437–15462.

Perch-Nielsen, K., 1979. Calcareous nannofossils from the Cretaceous between the North Sea and the Mediterranean. *In* Wiedmann, J. (Ed.), *Aspekte der Kreide Europas.* Int. Union Geol. Sci., Ser. A, 6:223–272.

———, 1985. Mesozoic calcareous nannofossils. *In* Bolli, H. M., Saunders, J. B., and Perch-Nielsen, K. (Eds.), *Plankton Stratigraphy:* Cambridge (Cambridge Univ. Press), 329–426.

Pisciotto, K. A., 1981. Distribution, thermal histories, isotopic compositions, and reflection characteristics of siliceous rocks recovered by the Deep Sea Drilling Project. *In* Warme, J. E., Douglas, R. G., and Winterer, E. L. (Eds.), *The Deep Sea Drilling Project: A Decade of Progress.* SEPM Spec. Publ., 32:129–148.

Roth, P. H., 1978. Cretaceous nannoplankton biostratigraphy and oceanography of the northwestern Atlantic Ocean. *In* Benson, W. E., Sheridan, R. E., et al., *Init. Repts. DSDP,* 44: Washington (U.S. Govt. Printing Office), 731–759.

Sanfilippo, A., and Riedel, W. R., 1985. Cretaceous radiolaria. *In* Bolli, H. M., Saunders, J. B., and Perch-Nielsen, K. (Eds.), *Plankton Stratigraphy:* Cambridge (Cambridge Univ. Press), 573–630.

Sayles, F. L., and Manheim, F. T., 1975. Interstitial solutions and diagenesis in deeply buried marine sediments: results from the Deep Sea Drilling Project. *Geochim. Cosmochim. Acta,* 39:103–127.

Schaaf, A., 1984. Les radiolaires du Cretace inferieur et moyen: biologie, systematique biochronologie et paleoenvironement. [These Doc. es Sci.], Univ. Louis Pasteur, Strasbourg.

Schlanger, S. O., and Moberly, R., 1986. Sedimentary and volcanic history: East Mariana Basin and Nauru Basin. *In* Moberly, R., Schlanger, S. O., et al., *Init. Repts. DSDP,* 89: Washington (U.S. Govt. Printing Office), 653–678.

Schroeder, C. J., 1986. Deep-water arenaceous foraminifera in the Northwest Atlantic Ocean. *Can. Tech. Rept. Hydrogr. Ocean Sci.,* 71:1–191.

Shipboard Scientific Party, 1989. Site 717: Bengal Fan. *In* Cochran, J. R., Stow, D.A.V., et al., *Proc. ODP, Init. Repts.,* 116: College Station, TX (Ocean Drilling Program), 45–90.

Shipboard Scientific Party, 1990a. Site 765. *In* Gradstein, F. M., Ludden, J. N., et al., *Proc. ODP, Init. Repts.,* 123: College Station, TX (Ocean Drilling Program), 63–267.

Shipboard Scientific Party, 1990b. Site 780. *In* Fryer, P., Pierce, J., et al., *Proc. ODP, Init. Repts.,* 125: College Station, TX (Ocean Drilling Program).

Shipley, T. H., Whitman, J. M., Dunnebier, F. K., and Peterson, L. D., 1983. Seismic stratigraphy and sedimentation history of the East Mariana Basin, Western Pacific. *Earth Planet. Sci. Lett.,* 64:257–275.

Sissingh, W., 1977. Biostratigraphy of Cretaceous calcareous nannoplankton. *Geol. Mijnbouw,* 56:37–65.

Steinberg, M., 1981. Biosiliceous sedimentation, radiolarite periods and silica budget fluctuations. *In* Int. Geol. Congr., 26th, Ocean Symp., (Paris 1980). *Oceanol. Acta,* 149–154.

Tamaki, K., Nakanishi, M., Sayanagi, K., and Kobayashi, K., 1987. Jurassic magnetic lineations of the western Pacific Ocean and the origin of the Pacific plate. *Eos,* 68:1493.

Thiede, J., Vallier, T. L., et al., 1981. *Init. Repts. DSDP,* 62: Washington (U.S. Govt. Printing Office).

Thierstein, H. R., 1971. Tentative Lower Cretaceous nannoplankton zonation. *Eclogae Geol. Helv.,* 64:459–488.

———, 1973. Lower Cretaceous calcareous nannoplankton biostratigraphy. *Abh. Geol. Bundesanst. Austria,* 29:1–52.

———, 1976. Mesozoic calcareous nannoplankton biostratigraphy of marine sediments. *Mar. Micropaleontol.,* 1:325–362.

Wise, S. W., Jr., and Weaver, F. M., 1974. Chertification of oceanic sediments. *In* Hsü, K. J., and Jenkyns, H. C. (Eds.), *Pelagic Sediments: on Land and under the Sea.* Spec. Publ. Int. Assoc. Sedimentol., 1:301–326.

Witmann, J. M., Baltuck, M., Haggerty, J. A., and Dean, W., 1986. Turbidite sedimentology and history of the East Mariana Basin. *In* Moberly, R., Schlanger, S. O., et al., *Init. Repts. DSDP,* 89: Washington (U.S. Govt. Printing Office), 365–387.

Yeats, R. S., Hart, S. R., et al., 1976. *Init. Repts. DSDP,* 34: Washington (U.S. Govt. Printing Office).

Zotto, M., Drugg, W. S., and Habib, D., 1987. Kimmeridgian dinoflagellate stratigraphy in the Southwestern North Atlantic. *Micropaleontology,* 33:193–213.

Ms 129A-102

NOTE: All core description forms ("barrel sheets") and core photographs have been printed on coated paper and bound as Section 3, near the back of the book, beginning on page 247.

Hole 800A: Resistivity-Sonic-Gamma Ray Log Summary

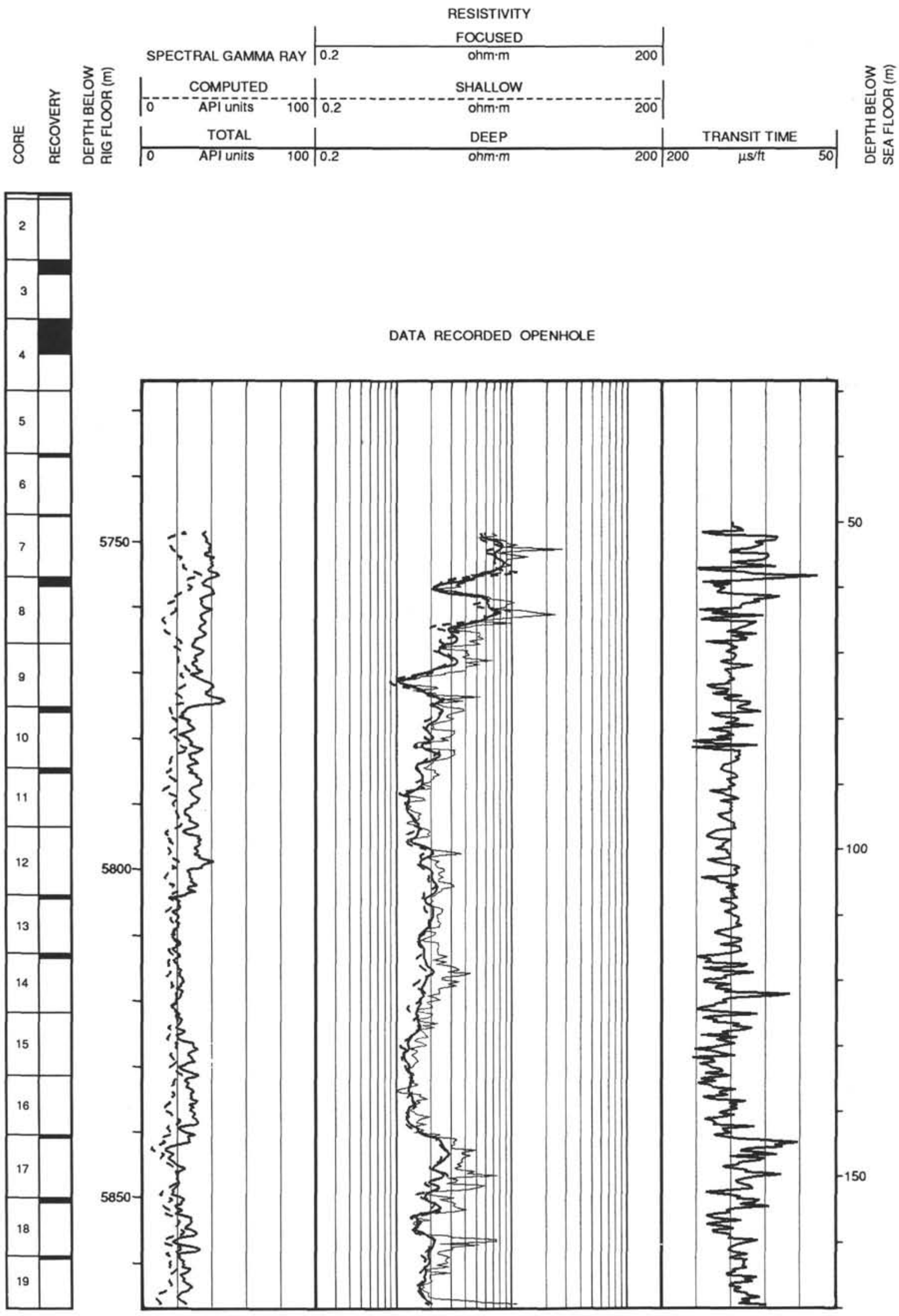

Hole 800A: Resistivity-Sonic-Gamma Ray Log Summary (continued)

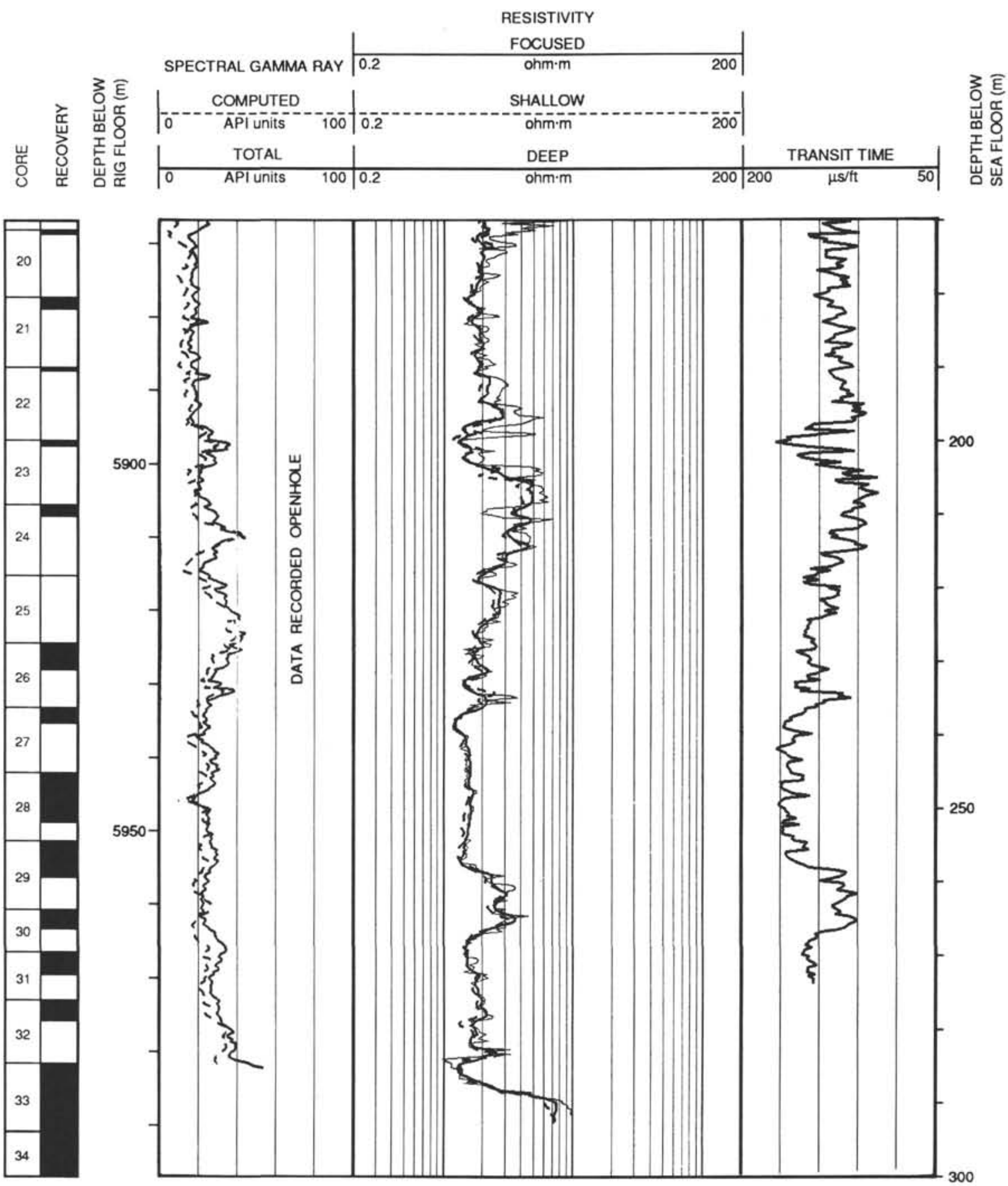

Hole 800A: Density-Caliper-Gamma Ray Log Summary

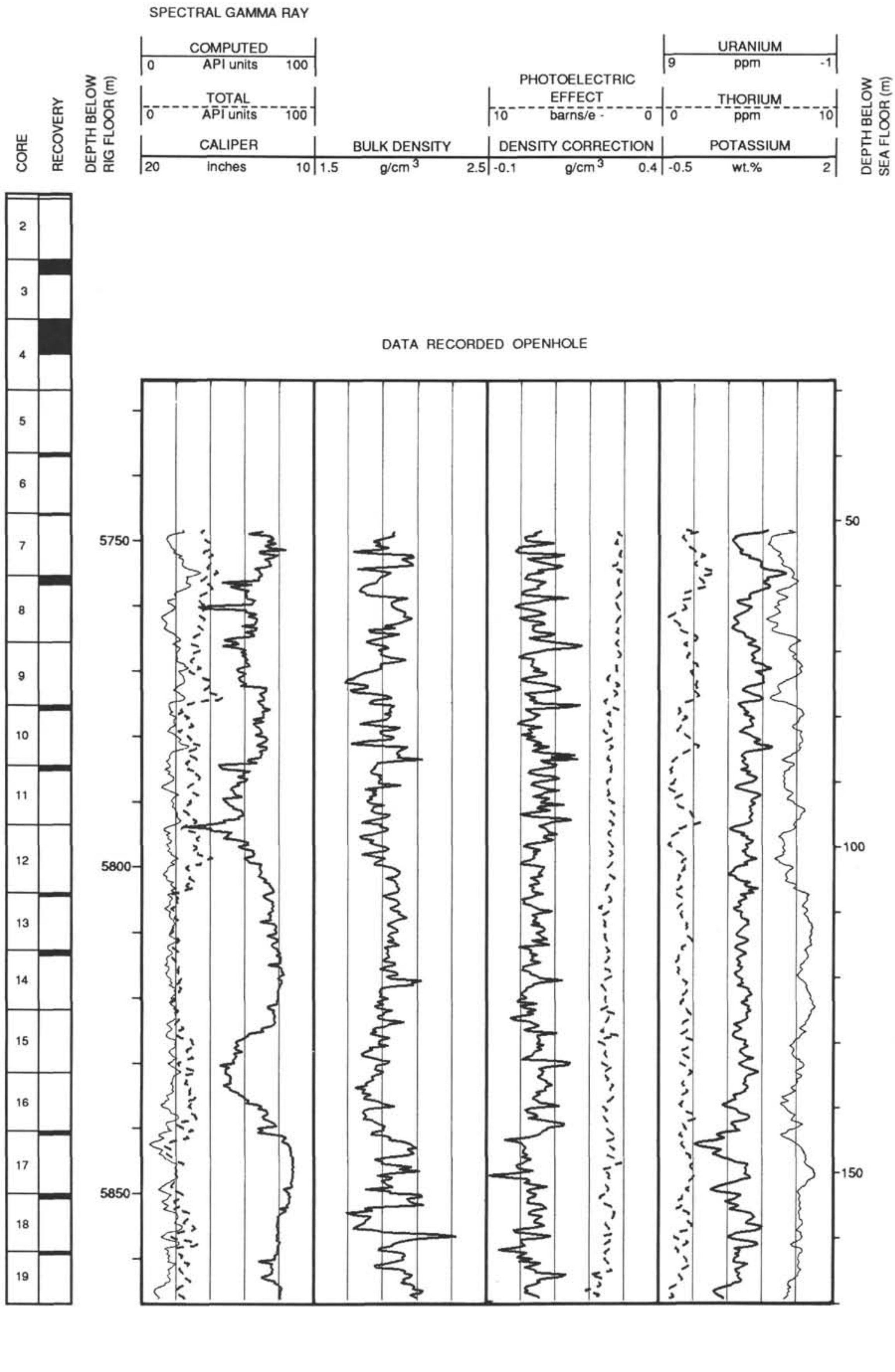

Hole 800A: Density-Caliper-Gamma Ray Log Summary (continued)

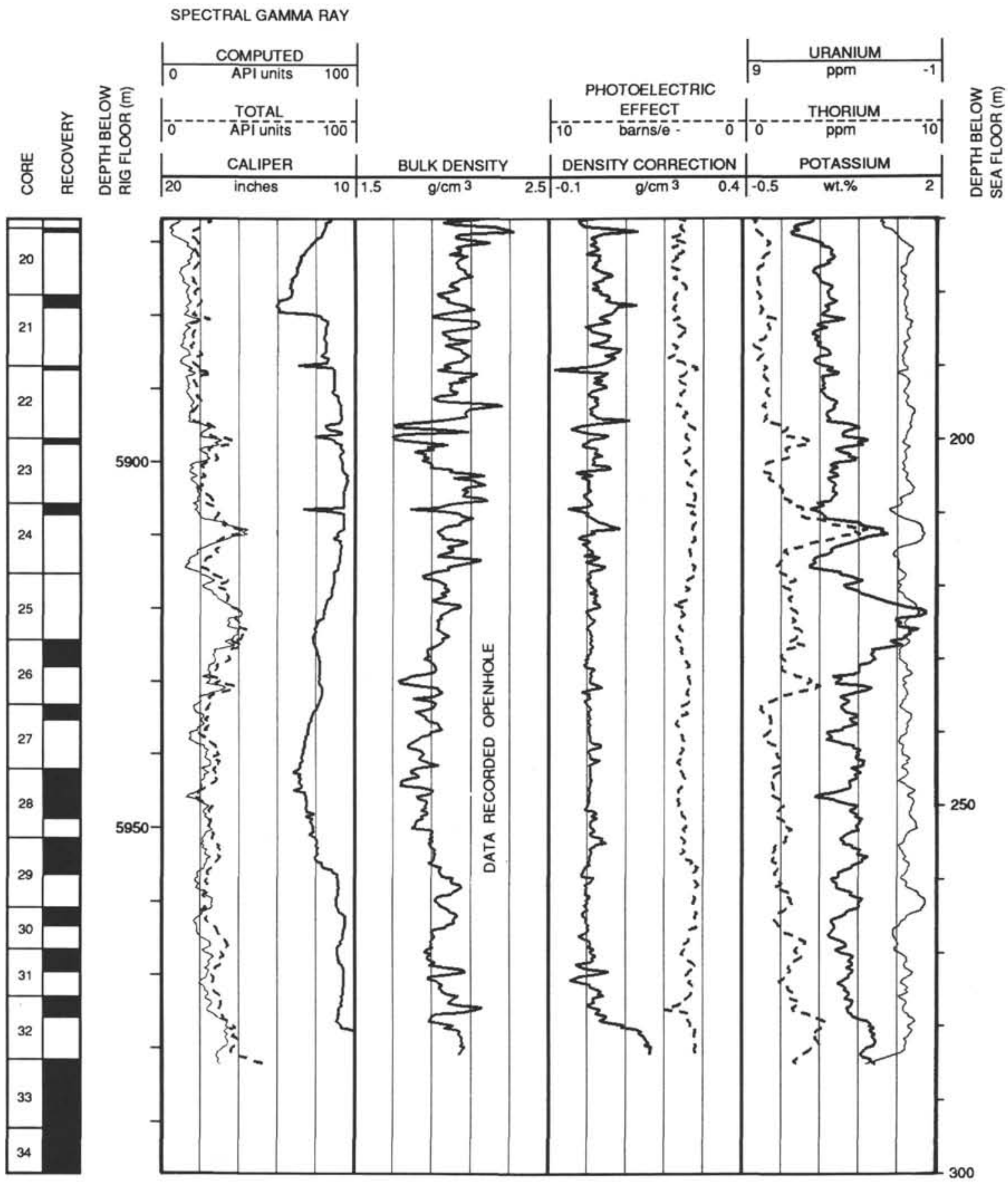

Hole 800A: Geochemical Log Summary

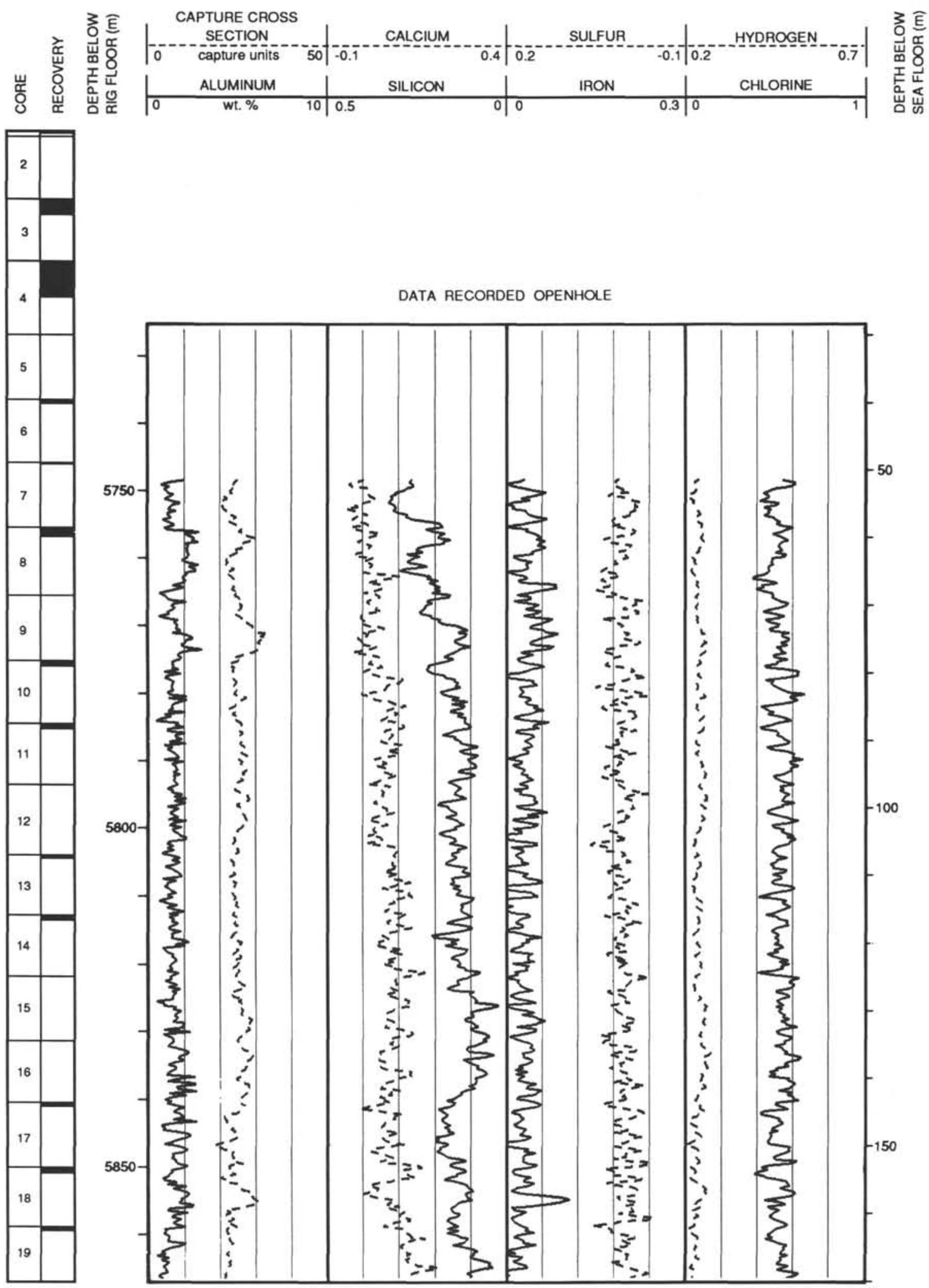

Hole 800A: Geochemical Log Summary (continued)